University of Alberta

Ferromagnetic Resonance in a Permalloy Microstructure Using Time Resolved Scanning Kerr Effect Microscopy

by

Wayne Kevin Hiebert

A thesis submitted to the Faculty of Graduate Studies and Research in partial fulfillment of the requirements for the degree of Master of Science.

Department of Physics

Edmonton, Alberta

Spring 1998

National Library of Canada
Acquisitions and Bibliographic Services
395 Wellington Street
Ottawa ON K1A 0N4
Canada

Bibliothèque nationale du Canada
Acquisitions et services bibliographiques
395, rue Wellington
Ottawa ON K1A 0N4
Canada

Your file Votre référence

Our file Notre référence

The author has granted a non-exclusive licence allowing the National Library of Canada to reproduce, loan, distribute or sell copies of this thesis in microform, paper or electronic formats.

The author retains ownership of the copyright in this thesis. Neither the thesis nor substantial extracts from it may be printed or otherwise reproduced without the author's permission.

L'auteur a accordé une licence non exclusive permettant à la Bibliothèque nationale du Canada de reproduire, prêter, distribuer ou vendre des copies de cette thèse sous la forme de microfiche/film, de reproduction sur papier ou sur format électronique.

L'auteur conserve la propriété du droit d'auteur qui protège cette thèse. Ni la thèse ni des extraits substantiels de celle-ci ne doivent être imprimés ou autrement reproduits sans son autorisation.

0-612-28942-7

Canada

November 5, 1997

Copyright Permission

The co-authors, W. K. Hiebert, A. Stankiewicz, and M. R. Freeman, of the article entitled, *Direct Observation of Magnetic Relaxation in a Small Permalloy Disk by Time-Resolved Scanning Kerr Microscopy*, published in Physical Review Letters, Volume 79, Number 6, 11 August 1997, pages 1134-1137, hereby give permission to W. K. Hiebert for use of the material in his Master of Science thesis entitled, *Ferromagnetic Resonance of a Permalloy Microstructure Using Time Resolved Scanning Kerr Effect Microscopy*, University of Alberta, 1997.

W. K. Hiebert — Date: Nov 5/97

A. Stankiewicz — Date: Nov 5/97

M. R. Freeman — Date: Nov 5/97

University of Alberta

Faculty of Graduate Studies and Research

The undersigned certify that they have read, and recommend to the Faculty of Graduate Studies and Research for acceptance, a thesis entitled *Ferromagnetic Resonance in a Permalloy Microstructure Using Time Resolved Scanning Kerr Effect Microscopy* submitted by *Wayne Kevin Hiebert* in partial fulfillment of the requirements for the degree of *Master of Science*.

Dr. M.R. Freeman (Supervisor)

Dr. J.A. Tuszynski

Dr. J. Jung

Dr. M.J. Brett

Date: 11/07/97

FERROMAGNETIC RESONANCE OF A PERMALLOY MICROSTRUCTURE USING TIME RESOLVED SCANNING KERR EFFECT MICROSCOPY

Magnetic oscillations were studied in a single lithographically patterned permalloy microstructure, placed in an in-plane biasing magnetic field, excited by sub-nanosecond pulses of perpendicular field. Local changes of the perpendicular magnetization component were detected by time-resolved scanning Kerr effect microscopy, allowing direct observation of the non-uniform spatial evolution of the magnetization. The modal frequency of the oscillations was found to agree well with the ferromagnetic resonance frequency. Modeling with the Landau-Lifshitz-Gilbert equation, with damping constant equal to 0.008, well described more uniform features of the data and clear departures were evident due to non-uniform response.

PREFACE

This work may be generally grouped into two categories: (1) technical concerns encompassing fabrication, characterization, and materials science issues, and (2) fundamental investigation including physical understanding, experimental technique, and scientific results. Chapters 3 through 6 fall roughly into the first group while chapters 7 and 8 mainly cover the second.

Chapter 1 gives the scope of the work with an introduction and motivation. Chapter 9 is the conclusion.

Chapter 2 is an attempt to prime the reader on concepts in magnetism important for this work. It is not near comprehensive of the entire field and is even incomplete in discussion of ferromagnetism and magnetization reversal but still gives a flavour for the fundamental motivations and concepts. Sections which are particularly key to the understanding of results and should be read are: 2.3 Landau-Lifshitz equation, 2.6.3 ferromagnetic resonance, and 2.7 magneto-optic Kerr effect.

Chapters 3 through 6 involve technical concerns beginning with the wide body of knowledge on materials and magnetic properties of NiFe in chapter 3. Chapters 4 and 5 deal specifically with fabrication of materials and devices needed for the experiment and include issues of design, deposition, and lithography. Some of the discussion does not lead to culmination in technique but is still important for ongoing development. Chapter 6 cites several techniques used in characterization of the devices; some of the material included comes from the learning process of an MSc. student and has, perhaps, as much value in the writing as the record.

Chapters 7 and 8 are the heart of the work and relate the crux of the scientific investigation. Chapter 7 deals with the experimental set-up and novel technique of TR-SKEM including insightful discussion regarding the technique and improvements. Chapter 8 gives the results of measurements and modeling and discussion of the fundamental investigation.

ACKNOWLEDGMENTS

There are several people and groups whom, without, I could not have completed this work.

For much technical advice and assistance, I gratefully acknowledge Ken Marsh, Don Mullin, Gilbert Lachat, Richard Tomski, Paul Zimmermann, and Steve Rogers. I must very much thank the Alberta Microelectronics Centre, particularly Glen Fitzpatrick, Kevin Kornelson, Lianne Lester, Graham McKinnon, Yan Qi, Niall Tait, and Ken Westra, with a special thanks to Ken Westra for extensive assistance and mentoring in all aspects of fabrication. I need to thank Ken Marsh and Eric Finley for their work in electron beam lithography and I must especially thank Ken Marsh for his long, dedicated hours in this venture. All my fabrication processes, abilities, and results were dependent upon participation of the aforementioned.

For stoichiometric determinations of thin film compositions, I acknowledge Arthur Mar, and Christine Barker. For high quality scanning electron microscope images, I thank George Braybrook. For several uses of, and assistance with, the magnetic force microscope, I thank Mark McDermott and Truong Ta.

For various assistance, discussion, and advice, I thank Mark Freeman, Abdul Elezzabi, Andrjez Stankiewicz, David Lawrie, Geoff Steeves, Greg Ballentine, Ray Egerton, and Marek Malac. In particular, for much assistance in the experiment, its results, and valuable discussion, I greatly thank Andrzej Stankiewicz, Mark Freeman, and Abdul Elezzabi.

Finally, I give my sincerest thanks and appreciation to my advisor, Mark Freeman, for his time, effort, support, and mentoring, to my parents, Marian and Fred, for their love and nurturing, and to my partner, Barbara Lopetinsky, for her loving encouragement, support, and understanding.

TABLE OF CONTENTS

1 **INTRODUCTION** 1

2 **RECENT HISTORICAL DEVELOPMENT OF MAGNETISM** 3

2.1 Introduction 3

2.2 Energy Considerations: From Weiss to Bloch 3

2.3 Landau-Lifshitz Equation 4

2.4 The Intricacy of H (Introduction of Anisotropy K, Exchange A, and Magneto-Striction λ) 5

2.4.1 External Magnetic Field 7

2.4.2 Magnetostatic Field 7

2.4.3 Anisotropy Field 7

2.4.4 Exchange Field 8

2.4.5 Eddy-current Field 9

2.5 Reversibility and Irreversibility: The Hysteresis Loop 9

2.6 Main Dynamical Problems 12

2.6.1 Domain wall dynamics: early work with dynamical Kerr microscopy 12

2.6.2 Dynamic reversal 13

2.6.3 Ferromagnetic resonance (FMR) 16

2.7 Introduction to the Magneto-Optic Kerr Effect (MOKE) 19

2.7.1 Definitions and reflectance coefficients 19

2.7.2 Generalized scanning Kerr effect microscope (SKEM) set-up 23

3 **PROPERTIES OF NiFe (PERMALLOY)** 29

3.1 "81/19" Permalloy 29

3.2 Annealing and Magnetic Annealing (Historical Work) 30

3.3 The Technically Interesting Range of 70-90% Ni Content 34

3.4 Recent Work in Property Engineering 36

4 **FABRICATION DESIGN** 40

4.1 Introduction 40

4.2 Mask 1: Lithographic Coils and Dots 40

4.3 Mask 2: Photoconductive Switches 43

5 **FABRICATION** 45

5.1 Introduction 45

5.2 Deposition 45

5.2.1 Conducting layer 45

5.2.2 NiFe layer 46

5.2.2A Electron-beam evapouration 46

5.2.2B Perkin Elmer sputtered permalloy 47

5.2.2C Ultra-high vacuum (UHV) sputtered permalloy 47

5.2.2D IBM electroplated permalloy 54

5.3 Patterning 54

5.3.1 Photolithography and wet chemical etching 54

5.3.1A Gold 56

5.3.1B Permalloy 57

5.3.2 Ion milling 58

5.3.3 Electron beam lithography (ebl) and liftoff technique 69

5.3.4 Double lithography technique 66

5.4 Summary 69

6 CHARACTERIZATION 70

6.1 Introduction 70

6.2 SEM Thin Film Stoichiometry 70

6.3 Magnetic Force Microscopy (MFM) 72

6.4 Hysteresis Measurements 82

6.4.1 SQUID magnetometery 82

6.4.2 Optical measurements: static longitudinal MOKE 86

7 EXPERIMENTAL SET-UP: TIME RESOLVED SCANNING KERR EFFECT MICROSCOPY (TR-SKEM) 94

7.1 Introduction 94

7.2 Polar TR-SKEM 94

7.3 Sample Mounting and Electrical Considerations 97

7.4 Static Longitudinal MOKE Detection Revisited 100

7.5 The Generalized TR-SKEM 106

7.6 Summary 111

8 RESULTS 114

8.1 Introduction 114

8.2 Probe Beam "Lithography" 114

8.3 Time Scans: FMR Frequencies 120

8.4 Non-Uniformity: Spatial Variation of Magnetization 123

8.5 The Tipping Field: $H_t(t)$ 129

8.6 Magnetic Modeling: Numerical Solutions to the Landau-Lifshitz-Gilbert Equation 134

8.7 More Investigations of the Spatially Varying Magnetization Response 138

8.8 Rotation by 90°: Spatial Variance Confirmation, New Tipping Pulse, and Precise Modeling Results 140

8.9 Discussion: Uniform Modeling vs. Non-Uniform Response 146

8.10 Summary 147

9 CONCLUSION 149

Bibliography 150

Appendix 157

LIST OF TABLES

3.1	Magnetic constants for NiFe alloys	35
6.1	Thin film stoichiometry (weight percent Ni or Fe)	71

LIST OF FIGURES

2.1	Damped precession of the magnetization vector (cartoon)	6
2.2	Example of a hysteresis loop	10
2.3	Domain wall "potential energy surface"	10
2.4	Example of easy and hard hysteresis loops	10
2.5	Modes of magnetization for an infinite cylinder	15
2.6	Inverse switching time in a permalloy film	15
2.7	Classic microwave FMR experiment	17
2.8	FMR curve for swept field	17
2.9	Resonance peak broadening	17
2.10	Polar, longitudinal, and transverse Kerr effects	20
2.11	p- and s- polarized light	20
2.12	Magneto-optic parameter for NiFe	24
2.13	Longitudinal Kerr rotation angles in NiFe	24
2.14	MOKE set-up	25
2.15	MOKE set-up with blocking of half the beam	25
2.16	Half beam blocking by using a cut mirror	25
2.17	Crossed polarizers detection	27
2.18	Split-beam subtraction	27
3.1	Effect of heat treatments on initial permeability of NiFe	31

3.2	Variation of maximum permeability with composition and rate of cooling	31
3.3	Magnetic anisotropy constants of quenched and slowly cooled NiFe	32
3.4	Variation of anisotropy constants of NiFe with cooling rate	32
3.5	Magnetostriction of quenched and slowly cooled NiFe	33
3.6	Dependence of induced uniaxial anisotropy on annealing temperature	33
3.7	Magnetostriction of NiFe in 60% to 90% Ni range	35
3.8	$K_1=0$ and $\lambda=0$ lines in Ni-Fe-Cu-Mo system	37
3.9	$K_1=0$ and $\lambda=0$ lines in Ni-Fe-Cu-Mo system	37
3.10	Wall coercivity of NiFe as function of composition	38
4.1	Layout of microlithographic coils photomask die	42
4.2	Placement by double lithography	42
4.3	Close-up of microlithographic photoconductive switches	44
5.1	In-plane magnetic field assembly (cross-sectional cartoon)	50
5.2	In-plane magnetic field assembly	50
5.3	In-plane and normal magnetic field components of magnetization	52
5.4	Structural zone models for coating growth	52
5.5	Electron-beam lithography in PMMA (wagon wheels)	61
5.6	Electron-beam lithography in PMMA (six 2x1 μm particles)	61
5.7	Electron-beam lithography in PMMA (wagon wheels) - sample 1-6	63
5.8	Electron-beam lithography after liftoff (wagon wheels) - sample 1-5	63

5.9 Electron-beam lithography after liftoff (wagon wheels) - sample 1-5 63

5.10 Electron-beam lithography after liftoff (wagon wheels) - proper liftoff 63

5.11 Electron-beam lithography after liftoff (wagon wheels) - PMMA pie pieces 65

5.12 Electron-beam lithography after liftoff (wagon wheels) - sample 1-6 65

5.13 Electron-beam lithography after liftoff (wagon wheels) - "almost" liftoff 65

5.14 Electron-beam lithography after liftoff (wagon wheels) - PMMA pie pieces 65

5.15 Electron-beam lithography after liftoff (wagon wheels) - metallization upside 65

5.16 Electron-beam lithography after liftoff (2x1 μm particle) 67

5.17 Electron-beam lithography after liftoff (2x1 μm particle) - with defect 67

6.1 Lift mode of a magnetic force microscope (MFM) 73

6.2 MFM of sample "previous" 75

6.3 MFM of sample "previous" - magnified 75

6.4 MFM of sample "previous" - domain structure 76

6.5 MFM of sample "previous" - flux leak 76

6.6 MFM of wagon wheels 77

6.7 MFM of wagon wheels - domains in the lettering 77

6.8 MFM of wagon wheels - wheel hub size and magnetic response 79

6.9 MFM of wagon wheels - wheel hub absent of magnetic information 79

6.10 MFM of wagon wheels - possible wheel hub flux highlights 80

6.11 MFM of wagon wheels - single domain spokes 80

6.12 MFM of alignment marks on sample "previous" - classic closure domain 81

6.13	MFM of alignment marks on sample "previous" - corner splitting of domain	81
6.14	SQUID hysteresis loops of Perkin Elmer sputtered permalloy	83
6.15	SQUID hysteresis loops of UHV sputtered permalloy	85
6.16	MOKE hysteresis loops of 1st e-beam evapourated film	87
6.17	MOKE easy loops of 2nd e-beam evapourated film	89
6.18	MOKE easy loop of 3rd e-beam evapourated film	89
6.19	MOKE easy loop of IBM electrodeposited permalloy	91
6.20	MOKE easy loops of early UHV sputtered films	91
6.21	MOKE easy loop of magnet assembly UHV sputtered film	92
6.22	MOKE easy loop of sample "previous"	92
7.1	Full schematic of the polar TR-SKEM set-up	95
7.2	Cartoon of pump and probe beams striking the sample	96
7.3	Current vs. time in the PC switch	98
7.4	Dithered MOKE on "previous"	102
7.5	Dithered MOKE on 10x10 μm square	102
7.6	Dithered SKEM on 10x10 μm square	104
7.7	"Polarizing cross" in a microscope objective	105
7.8	MOKE hysteresis loop on a microstructured triangle	107
7.9	MOKE hysteresis loop on 10x10 μm square	107
7.10	Schematic of generalized SKEM measurement system	112

8.1	Characteristic time domain images of magnetization response	115
8.2	Spot burning on permalloy microstructures	115
8.3	SEM micrographs of sample 3.6.8	117
8.4	Spatial snapshots of polar magnetization in sample 3.6.8 after the defect	119
8.5	Probe beam "lithography"	119
8.6	Time domain magnetization response (FMR) for various external fields	121
8.7	FMR frequency vs. field in a permalloy microstructure	122
8.8	Time domain response at 500 Oe (numbered peaks)	124
8.9	Evolution of spatial magnetization response - "shock waves"	125
8.10	Possible reasons for spatial symmetries in fig 8.9	127
8.11	Time domain response in high field with interpolating fit	131
8.12	Spatial response in high field (2.17 kOe)	133
8.13	Spatial response in median field (1.1 kOe)	135
8.14	Numerical modeling of time domain response - double pulse	137
8.15	Time domain with corresponding spatial snapshots - animation possibility	139
8.16	Spatial magnetization evolution after the second pulse - rich structure	141
8.17	Time domain response and spatial magnetization at 90° sample rotation	142
8.18	Time domain response for several fields with simultaneous modeling fit	144

LIST OF SYMBOLS, NOMENCLATURE, AND ABBREVIATIONS

α	Gilbert damping parameter ($=\lambda/M_s$)
β	$\sin\theta$ (where θ is angle of incidence)
γ	gyromagnetic ratio
γ	$\cos\theta$ (where θ is angle of incidence)
γ'	$\cos\theta' = (1-(\sin^2\theta)/n^2)^{1/2}$ (where θ' is angle of transmission, θ is angle of incidence, and n is index of refraction)
$\Delta\omega$	frequency full width at half maximum
$\Delta\omega'$	broadened $\Delta\omega$
δ	small signal
ε	dielectric constant
θ	angle
θ	angle of incidence
θ	Curie temperature
θ	polar angle coordinate
κ_1,κ_3	diagonal dielectric tensor elements (complex)
κ_2	off-diagonal dielectric tensor element (complex)
λ	wavelength
λ	magneto-striction
λ	Landau-Lifshitz damping parameter
λ_{100}	magneto-striction in the <100> crystal direction
λ_{111}	magneto-striction in the <111> crystal direction
λ_s	saturation magneto-striction
$\bar{\mu}$	effective permeability
μ_0	initial permeability
μ_0	permeability of free space ($=4\pi\times10^{-7}$ Farads/meter in MKS)
$\mu\Omega$	micro-Ohms
μm	micrometers
μ_{max}	maximum permeability
μO	microscope objective
π	pi
σ	conductivity
τ	characteristic time; switching time; decay time
φ	polar angle coordinate
ϕ	polar Kerr effect rotation
ϕ_0	specific polar Kerr effect rotation attributed to light reflection from a perpendicularly magnetized surface
ω	frequency (angular)
A	angstroms
A	exchange constant
a	lattice spacing
AFM	atomic force microscopy
AMC	Alberta Microelectronics Centre
Ar	argon gas
As	arsenic
Au	gold
B	magnetic induction or flux density
$B_\parallel$	magnetic induction or flux density
B_e	eddy current field
B_{ex}	exchange field
B_r	remanence
C	degrees Celsius
CCD	charged coupled device
Cl	chlorine
cm	centimeters
Co	cobalt
Cr	chromium
Cu	copper
d	thickness

DA	differential amplifier
dc	direct current
DI	Digital Instruments
E	energy
$\vec{\mathbf{E}}$	electric field axis
$E_{\parallel}$	polarization vector
E_{an}	anisotropy energy
e-beam	electron beam
ebl	electron beam lithography
emu	electro-magnetic units
f	frequency
F.C.	a medium cooling rate
Fe	iron
f_{FMR}	ferromagnetic resonance frequency
FIR	finite impulse response low pass filter (assigns a weighted average of a neighborhood to the pixel)
FMR	ferromagnetic resonance
G	Gauss
Ga	gallium
H	magnetic field
H	magnetic field
h	hour
h	height
$H_{\parallel}$	magnetic field
$H_{\parallel}$	parallel magnetic field
$H_{\parallel}$	dc biasing magnetic field
H_c	coercivity
HF	hydrofluoric acid
Hf	hafnium
H_i	transient magnetic field
$H_i(t)$	transient magnetic field and/or interpolated function for the transient magnetic field
H_k	anisotropy field
HNO_3	nitric acid
H_2O	water
H_2O_2	hydrogen peroxide
H_s	pulsed magnetic field in easy direction
H_2SO_4	sulfuric acid
H_t	dc magnetic field in hard direction
Hz	Hertz
IBM	International Business Machines
I_p	Intensity of incident p-polarized light
IPA	isopropyl alcohol
I_s	Intensity of incident s-polarized light
J	total angular spin momentum
J	Joules
K	anisotropy constant
K_1	crystalline anisotropy
kG	kiloGauss
K_u	uniaxial anisotropy
M	magnetization
M	molar concentration
M	magnetization
M	saturation magnetization
median	statistical median low pass filter (assigns the median of a neighborhood to the pixel)
MFM	magnetic force microscopy
MIBK	methyl isobutyl ketone
min	minute
ml	milliliters
Mn	manganese
Mo	molybdenum
MOKE	magneto-optic Kerr effect
$\mathbf{M_p}$	magnetic moment on the p-th site
$\mathbf{M_q}$	magnetic moment on the q-th site
M_s	saturation magnetization
M_z	z- component of magnetization

n	index of refraction
N2	nitrogen gas
N.A.	numerical aperture
Nb	niobium
ND	neutral density filter
Ni	nickel
NiFe	nickel iron or "permalloy"
nm	nanometer
NMR	nuclear magnetic resonance
NPGS	nano pattern generation system
ns	nanoseconds
Oe	Oersted
P	polarizer
p-	definition for a type of light polarization involving reflection from an interface
PA	pre-amplifier
PC	photoconductive switch
PD	photodiode
PEM	photoelastic modulator
PMMA	poly methyl methacrylate
PR	photo resist
PR	polarization rotator
"previous"	name of a specific permalloy sample
ps	picoseconds
Py	permalloy
Q	complex magneto-optic parameter
QU	quenched
r	radius
RC	[resistance]x[capacitance] (gives a characteristic time)
rf	radio frequency
RMS	root mean square
R_p	Intensity of reflected p-polarized light
rpm	revolutions per minute
R_s	Intensity of reflected s-polarized light
r_{ss}, r_{pp}, r_{sp}, r_{ps}	elements of the s-, p-, reflectivity matrix
S	electron spin
s	seconds
s-	definition for a type of light polarization involving reflection from an interface
s_0, s_1, s_2, s_3	position points
SAW	surface acoustic wave
S.C.	slowly cooled
SCCM	standard cubic centimeters per minute
SEM	scanning electron microscope
SIL	solid immersion lens
SKEM	scanning Kerr effect microscopy
SPM	scanning probe microscopy
SQUID	superconducting quantum interference device
STM	scanning tunneling microscope
T	tesla
Ta	tantalum
Ti	titanium
TR-SKEM	time-resolved scanning Kerr effect microscopy
t_s	switching time
UHV	ultra-high vacuum
UV	ultraviolet
V	volume
V	Volts
V_{pp}	Volts peak-to-peak
v_y	wall velocity
W	Watts
w	free energy density
Zr	zirconium

1 INTRODUCTION

The physics of magnetization processes in nanostructured magnetic materials has become a subject of intense investigation[1.1-1.3]. Dynamical issues such as wall motion, magnetization reversal and reversal mechanisms, and ferromagnetic resonance have long been intriguing subjects for experimental and theoretical work and have been well tied with industrial application. Recently, strong advances in magnetic devices have pushed materials to the limit (high speed, ultra-high density magnetic recording) and have demanded a new, more fundamental understanding of these dynamics.

The advent of magnetic force microscopy (MFM) has rejuvenated experimental work, giving highly detailed spatial information of the static configurations. Combined with improved computational abilities a solid forum is provided for the comparison of numerical modeling and micromagnetics to experimental results[1.1,1.4-1.6]. In spite of this, measurement of dynamical phenomena has remained indirect and spatially unresolved, unable to provide the necessary information against which to test numerical predictions.

This work reports on studies of magnetic excitations in a permalloy microstructure using time-resolved scanning Kerr effect microscopy (TR-SKEM)[1.7]. This technique is uniquely well-suited to elucidate such dynamics. The combined picosecond temporal and sub-micrometer spatial resolutions allow direct study of dynamical phenomena; direct time dependence of magnetic excitation development is accomplished and "snapshot" magnetic maps of a sample surface are acquired. As a result, first-hand observation of the magnetic excitation development is obtained, giving non-uniform spatial profiles invisible to other techniques. In addition, numerical modeling is compared directly to data in the time-domain allowing determination of the phenomenological damping rate.

The experiment is effectively an optical implementation of a ferromagnetic resonance (FMR) measurement. The microstructure is magnetically saturated in-plane and excited by sub-nanosecond perpendicular field pulses. Optical detection synchronous with the excitations allows the temporal resolution (time-width of laser pulse) with a scanned, focused laser spot giving the spatial resolution (to the diffraction limit of optics).

Work in this thesis consists of :

1) fabrication design, fabrication, and characterization where the tasks of fabricating good quality permalloy microstructures and turning optical pulses into pulsed magnetic fields are taken up, and
2) experimental design and discussion and time-resolved measurement and analysis where TR-SKEM is used for elucidation of the dynamical magnetic properties of the permalloy microstructure including time-resolved observation of spatially non-uniform magnetization response.

2 RECENT HISTORICAL DEVELOPMENTS OF MAGNETISM

2.1 Introduction

Here I would like to briefly outline some of the major concepts in modern magnetism. I strive to introduce only those concepts that are needed for the context of this present work. There are several books on the subject referenced in the bibliography[2.1-2.6].

2.2 Energy Considerations - From Weiss to Bloch

One of the most important conceptual approaches in modern magnetism is use of minimization of energy in the ferromagnet. It was noticed that ferromagnets like iron would have no net magnetic moment at room temperature, though in theory, the exchange interaction in the material should have all spins lining up. Weiss was the first to propose[2.7] that this observation could be explained if the material were split up into several regions that were saturated in themselves but were randomly oriented macroscopically. This was the birth of the concept of domains.

Bloch was the first to consider[2.8] why this domain formation should happen from an energy point of view. If a material has a preferred axis of orientation (due to crystallinity, for example), there is an energy penalty associated with not lining up with that axis. Further energy (demagnetizing energy) is associated with free poles at the edges of a large, uniformly magnetized body and competes with energy that accompanies the formation of domain walls (the spins over a domain wall are not aligned and hence introduce exchange energy). Several other energy considerations add to the complexity of

a ferromagnet and can include energy due to magnetic "stretching" of the material called magnetostriction and energy due to inclusions or defects in the material. The minimization of these energies in the magnet is what leads to domain structure.

There are some important notes about domain formation. Generally, as a ferromagnet reduces in size, the number of domains decreases because the energy in a domain wall remains the same while the competing demagnetizing energy scales down. Eventually, if a ferromagnet is small enough in size, one single domain wall would contain more energy than the total of demagnetizing energy and the ferromagnet should act as a single domain. In thin films, there is a further consideration on the type of domain wall that is formed: a thick film will act like bulk material as the spins in the wall contain no component perpendicular to that wall (Bloch wall), a very thin film (as thin as the wall) will lead to very short domain walls (more like a domain line) meaning demagnetizing effects start to favour spin rotation in the thin film plane (Neel wall), and an intermediate thickness will result in a combination (cross-tie wall)[2.2].

2.3 Landau-Lifshitz equation

In a classic paper in 1935, Landau and Lifshitz considered a 180° domain wall in a material with an easy axis of magnetization[2.9]. A phenomenological theory was developed for the dynamic configuration in the form of the famous Landau-Lifshitz equation:

$$\left(\frac{-1}{\gamma}\right)\frac{d\mathbf{M}}{dt} = (\mathbf{M}\times\mathbf{H}) - \lambda\left[\mathbf{H} - (\mathbf{H}\bullet\mathbf{M})\mathbf{M}/M_s{}^2\right] \qquad (1)$$

where **M** is the magnetization at a given point and **H** is the magnetic field felt at that point.

The first part on the right hand side is simply stating that, when **M** and **H** are not

parallel, the configuration will not be static. Indeed because we are dealing with the coupling of an angular momentum (spin) with the magnetic field we find a precession of the spin vectors (fig 2.1) around that field given by the time rate of change of **M** (γ is the gyromagnetic ratio or the magneto-mechanical coupling given by e/m = $1.76 \times 10^{11}\ s^{-1}T^{-1}$).

The second part on the right hand side arises from the fact that **M** and **H** will never align with just the first term. With a direction of **H-M** and a magnitude that approaches zero as **H** and **M** become parallel, this second term acts as a source of damping to the dynamical equation (here λ is a damping parameter having the same dimensions as *M*).

The Landau-Lifshitz equation has been written in other forms. Galt wrote the form most often quoted as the Landau-Lifshtiz equation[2.10] and Bloch-Bloembergen have used another. One form in much use today is the Gilbert formulation[2.11]:

$$\frac{d\mathbf{M}}{dt} = -\gamma(\mathbf{M}\times\mathbf{H}) - \alpha\left(\frac{1}{M_s}\right)\mathbf{M}\times\frac{d\mathbf{M}}{dt} \qquad (2)$$

where we now have a dimensionless damping parameter α. This form will be made use of in the work described herein.

2.4 The Intricacy of H (Introduction of Anisotropy K, Exchange A, and Magneto-Striction λ)

The Landau-Lifshitz equation may look easy to deal with but what makes up the variable **H** can be very complicated. The field that each spin feels acting upon it can vary over a physical sample and even from spin to spin if the conditions change. In general **H** can be thought of as containing an external magnetic field, a magnetostatic field, an anisotropy field, an exchange field, and a reaction field due to eddy currents (in a

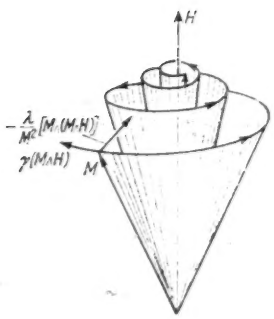

Fig 2.1 Damped precession of the magnetization vector. The terms containing γ and λ are the oscillatory and damping terms, respectively, in a different formulation of the Landau-Lifshitz equation[2.3].

conducting ferromagnet).

2.4.1 External magnetic field

This is simply the field applied to the sample that would be there regardless of the sample's presence. We will call it $\mathbf{B}_a = \mu_0 \mathbf{H}_a$.

2.4.2 Magnetostatic Field

This is field that each spin feels due to the total magnetization of the sample: $\mathbf{B} = \mu_0 \mathbf{H} + \mathbf{M}$. This nonlinearity is what makes the solution to the total field untenable, except for contrived sample conditions (infinite sample or div$\mathbf{H}$ = 0 for instance), because this magneto-static field depends on the magnetization (and derivatives) at every point in the sample (similarly, the demagnetizing field of a sample is unsolvable except for special cases like the ellipsoid). Landau and Lifshitz use a contrived sample in their original paper out of which comes the speed of the domain wall.

2.4.3 Anisotropy Field

This is the field produced by the various anisotropies of the sample of which there can be many different types. The spins in a sample may have a preferred direction of orientation (along the "easy-axis"), in which case there is extra energy associated with orientations not in this preferred direction. This preference can be caused by:

i) a crystallographic orientation of the sample (magneto-crystalline anisotropy),

ii) demagnetizing effects due to free poles at the sample surface, ultimately depending on the shape (shape anisotropy)

iii) stress in the sample which can be induced (magnetostrictive anisotropy)

iv) annealing a sample in a magnetic field (induced magnetic anisotropy)

This interaction can be expressed in terms of a $\sin^2$ power series: $E_{an} = K_1 \sin^2\phi + K_2 \sin^4\phi + \ldots$, where the first term is often adequate and leads to the (simplest) anisotropy field of: $(B_{an})_x = -2K_u M_x / M_s^2$, $(B_{an})_y = -2K_u M_y / M_s^2$, and $(B_{an})_z = 0$, where the easy axis has been taken to be parallel to the z-axis.

Note that magnetostriction is important in its own right, though of less concern for the present work. Magnetostriction λ is a constant per material (for instance λ_{111} is the "magnetostriction" in the <111> crystal orientation). The calculation of λ depends on the crystal structure and lattice spacing and will not be given here. A positive constant means elongation along that axis with increasing magnetization, negative means constriction with increasing magnetization.

2.4.4 Exchange Field

An exchange interaction between neighboring spins is minimized in a ferromagnet by alignment (as opposed to energy minimization for anti-alignment in anti-ferromagnets). This is often considered from atomic coupling in the lattice where a potential energy takes the form of $V = \left(-2JS^2 / M_s^2\right)\mathbf{M}_p \bullet \mathbf{M}_q$ where J is the exchange energy integral, S is the spin, $\mathbf{M}_p/M_s$ and $\mathbf{M}_q/M_s$ are unit vectors in the directions of the spins on the pth and qth sites (notice the minimum happens for parallel spins). A usual nomenclature convention is to introduce $A=2JS^2/a$ as the exchange constant (where a is the lattice spacing). A simple

form of the exchange field might look like: $B_{ex} = \left(2A / M_s^2\right)\nabla^2 \mathbf{M}$

2.4.5 Eddy-current field

This field is the reciprocating result of the currents that are induced by "magnetic motion" in the sample (known as eddy currents). A first approximation would depend on the velocity of the wall (v_y), conductivity (σ), height (h), and saturation magnetization of the sample: $B_e = \mu_0 \sigma h M_s v_y / \pi$.

Another way to look at eddy currents is their characteristic decay time in a finite-sized conductive sample. This would be proportional to conductivity and area of current flow. An expression for this would be: $\tau = \mu_0 \sigma r d/2$ where τ is an eddy current decay time and r and d are radius and thickness of the ferromagnet, respectively.

2.5 Reversibility and Irreversibility: The Hysteresis Loop

Reversal of magnetization in a ferromagnet is an interesting process. Ramping a magnetic field from saturation in one direction to saturation in the opposite direction usually involves irreversible processes and a loss of energy which is visible in a graph of flux density B or magnetization M vs. magnetic field H (fig 2.2). This is known as the hysteresis curve and is characterized by its "squareness", remanence (B_r), and coercivity (H_c).

The least energetic reversal process involves movement of domain walls. The energy associated with a wall, however, will vary spatially over the magnet due to grain boundaries and inclusions (fig 2.3) as it takes less energy for a wall to sit on an impurity.

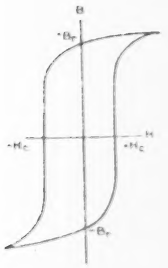

Fig 2.2 Example of hysteresis loop with definitions of remanence B_r and coercivity H_c[2.6].

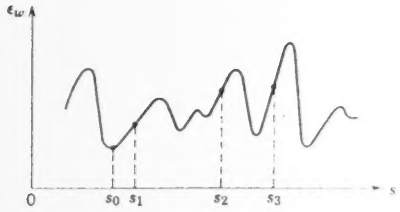

Fig 2.3 "Potential energy surface": variation of the wall energy as a function of position of the domain wall. The movement from s_0 to s_1 is reversible; the movement from s_2 to s_3 is irreversible[2.4].

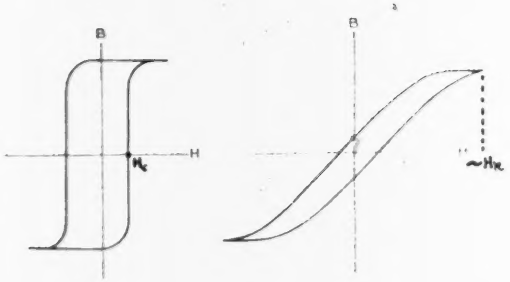

Fig 2.4 **(a)** Easy axis hysteresis loop and coercive field H_c. **(b)** Hard axis hysteresis loop and approximate value of anisotropy field H_k[2.6].

Small wall movements (for instance, from s_1 to s_2) will revert to their original position with removal of the field that caused the movement. A larger wall movement that crosses an energy barrier, however (s_3 to s_4) will not return upon removal of the field and needs extra energy (extra field in the opposite direction) to return to their original position. This accounts for the remanence at zero field and the coercivity. Of note, another type of reversal - by rotation - can be reversible and irreversible as well. In general, both types of reversal, and both reversibilities and irreversibilities happen as the field is swept giving the particular shape of the hysteresis curve. The sweep range also effects the shape of the curve; a smaller sweep range may not overtake all irreversibilities leading to what is called a minor hysteresis loop as opposed to the full (major) hysteresis loop.

As a special note, in the case of anisotropy energy being present (magnetization having a preferred direction) the ferromagnet may have an easy and a hard axis defined as aligned with preferred direction and 90° to alignment, respectively. Applying the field sweep along the easy axis should result in a squarer loop as spins are harder to turn away from the axis and want to anti-align as soon as they do (fig 2.4(a)). Sweeping the field in the hard direction should result in a small hysteresis with low remanence since spins will want to "lead" the field to zero in the hard direction (by aligning with the easy axis) and will be slow and steady to rotate to saturation in the opposite field (fig 2.4(b)). The anisotropy field H_k may be defined as the field necessary to saturate the magnetization in the hard direction: that is, the field that is able to completely overcome anisotropy energy.

2.6 Main dynamical problems

Some of the major dynamical problems worked on will be outlined below. These include domain wall motion, dynamic reversal and reversal mechanisms, and ferromagnetic resonance.

2.6.1 Domain wall dynamics: Early work with dynamical Kerr microscopy

This problem is linked with dynamic reversal in many ways. It is interesting from both the point of view of understanding and that of application, to study the way a magnetic material will respond to a change in magnetic field.

The Landau-Lifshitz equation was applied to domain wall motion to determine characteristic wall velocities and wall mobilities. A good report on this technique, its correction for eddy current damping, and its application to permalloy, is given in O'Dell[2.1]. Some of the experiments used to test these velocities used optical techniques to directly study the magnetization: specifically the magneto-optic Kerr effect, MOKE, (more on this effect will be said in this chapter), was first used in the dynamical sense by Lee and Calaby[2.12] for this detection. The basic experiment had two separated laser spots to detect the passage of a wall in time (giving velocity). Altered forms of this technique were done by Ford[2.13] and Thompson and Chang[2.14]. These first attempts were strewn with problems in measuring velocity because of a delay in starting and stopping of the wall with the driving pulse. The first implementation of a stroboscopic technique to do this detection was by Green and Prutton in 1962[2.15], (followed by Copeland and Humphrey[2.16] and Conger and Moore[2.17]). This work culminated in single shot high speed photography by Kryder and Humphrey[2.18,2.19,2.20]. More recently, wall motions continue to be studied in

this way[2.21,2.22] and are even used in reverse to modulate light spots, knowing wall velocity.[2.23] More discussion on the Kerr effect experiment and its history will be given later in this chapter.

Domain wall dynamics are still of much interest and are now better tied into ferromagnetic resonance. Exact solutions for domain walls in a uniaxial ferromagnet are known for the static case but much recent theoretical, computational, and experimental work has been done for the dynamic situation. Schryer and Walker have considered the motion of 180° domain wall in step-function dc magnetic fields[2.24] where the wall tends smoothly to equilibrium unless the driving field is greater than the coercivity, in which case a precessing periodic motion of the wall occurs. Smith[2.25] proposes a dynamic domain model for magnetic thin films (in theory and computation) and Helman[2.26] gives a general solution to the Landau-Lifshitz-Gilbert equation linearized around a Bloch wall.

2.6.2 Dynamic reversal

Wall motion may almost be thought of as a subfield of dynamic reversal: understanding reversal being the more important goal (both for physics and application), with the study of wall motion being the method to understanding. Understanding dynamic reversal is almost at the very heart of ferromagnetism. Additionally some of the most useful applications of the ferromagnet have proven to be in digital data storage and this technology depends on reversal.

There are several different mechanisms that the magnet can use to reverse from one direction to another. Domain wall motion consist of domains aligned with the external field growing and those aligned against the field shrinking (via movement of the

domain wall). It is the least energetic of processes, but also the slowest. Coherent rotation will be quicker, and therefore more desirable in the case of magnetic recording, for instance. In general, the explicit dynamics of the reversal process are not yet well understood, especially experimentally. Theoretical work in dynamic reversal has had a large head start through micromagnetics.[2.27] Frei[2.28] shows how reversal could take place in an infinite cylinder by rotation in unison, curling, or buckling as shown in figure 2.5. It was first shown by Conger[2.29] that, for coherent rotation in a thin film memory element, the switching time τ should become faster with the field B_z ($\tau = 1.76\ \alpha / |\gamma|\ B_z$ where α, γ are Gilbert damping parameter and gyromagnetic ratio, respectively) though this time was found to be inaccurate experimentally, possibly due to a magnetization ripple effect[2.1]. Thomson derived a form for coherent rotation switching time that depends on energy as a function of angle[2.2] ($t_s = \frac{\lambda}{\gamma^2}\int_{\theta 1}^{\theta_2} \frac{d\theta}{\partial E/\partial\theta}$ with λ being the L-L damping parameter and γ being the gyromagnetic ratio). No matter what the form of t_s for coherent rotation or domain wall motion, the two are found to have different signatures. Figure 9[2.6,2.2] shows some switching investigation on films of uniaxial permalloy studied by Dietrich et.al.[2.30]. H_s was a pulsed field in the easy direction (a dc field H_t was applied in the hard direction). Reversible changes were found for H_s ($H_s >> H_c$) where the film appears to switch entirely by coherent rotation. More recently, Lederman et. al. measure the spontaneous thermal switching of a single domain particle[2.31] and find evidence of a much more complex reversal then the single energy barrier model of Neel[2.32]. High powered computer calculations with micromagnetics have given simulations of reversal processes[2.33,2.34,2.35]. Experimental work that probes the dynamics directly has been lagging and this is where

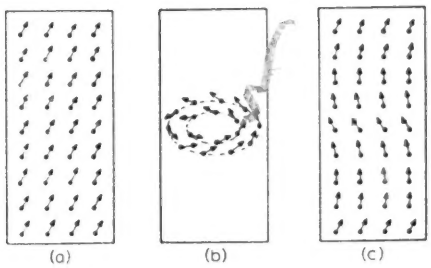

Fig 2.5 Modes of magnetization for an infinite cylinder: **(a)** rotation in unison, **(b)** magnetization curling, and **(c)** magnetization buckling[2.28].

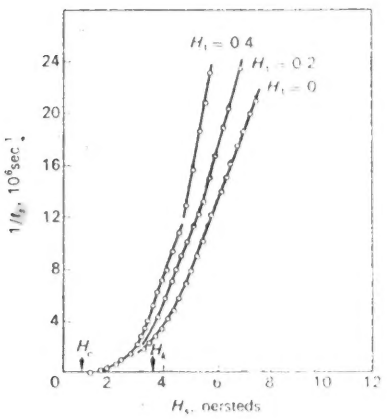

Fig 2.6 Inverse switching time as a function of the longitudinal field strength for a permalloy film of unspecified thickness. H_s is the pulsing field along the easy axis; H_t is a dc field along the hard axis[2.2].

time resolved scanning probe techniques can become extremely useful.

2.6.3 Ferromagnetic resonance (FMR)

Effectively, we've already introduced Ferromagnetic Resonance (FMR) by introducing the Landau-Lifshitz equation and the oscillatory behaviour associated with it when the magnetization is not aligned with the external field (equations 1 and 2 and figure 1). The motion of excited magnetic spins may be called FMR (just as the motion of nuclear spins is termed NMR), though classically, the excitation should be sinusoidal to be called resonance (in our experiment, the excitation is pulsed). More recently, pulsed magnetic resonance has been more common than continuous wave magnetic resonance.

For the simple, uniformly magnetized ferromagnet, H takes on the form $H = H_{\parallel} + 4\pi M_s$ and solving the undamped Landau-Lifshitz equation, one may obtain a characteristic resonance frequency $\omega = \gamma\sqrt{H_{\parallel}(H_{\parallel} + 4\pi M_s)}$. To maintain resonance, however, energy must be fed into the system, because of the various forms of damping (crystal lattice, etc.). Figure 2.7 shows the classic set-up for the microwave cavity FMR experiment. The magnetic material is aligned in a strong external field. A microwave, with its magnetic vector perpendicular to the external field, induces precession in the spins and is thus absorbed. By ramping the external field, the absorption (or, experimentally, the effective permeability) may be measured and the peak absorption should correspond to a match between the resonance frequency and microwave frequency (fig 2.8). Not only are resonance frequencies obtained, but the width of the resonance peak may also be used to calculate the damping coefficient.[2.1] This calculation, however, must assume excitation of only uniform modes in the resonance (that is, identical resonance conditions everywhere in

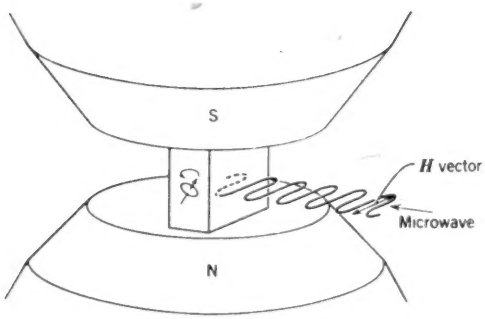

Fig 2.7 Classic microwave FMR experiment[2.4].

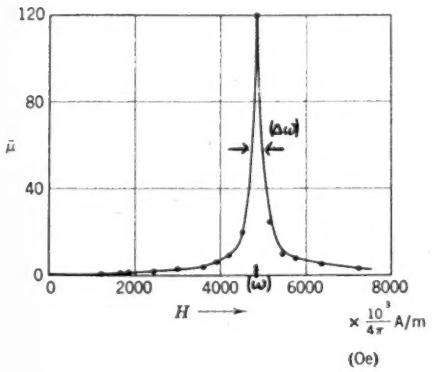

Fig 2.8 Example of FMR curve for swept field H[2.4].

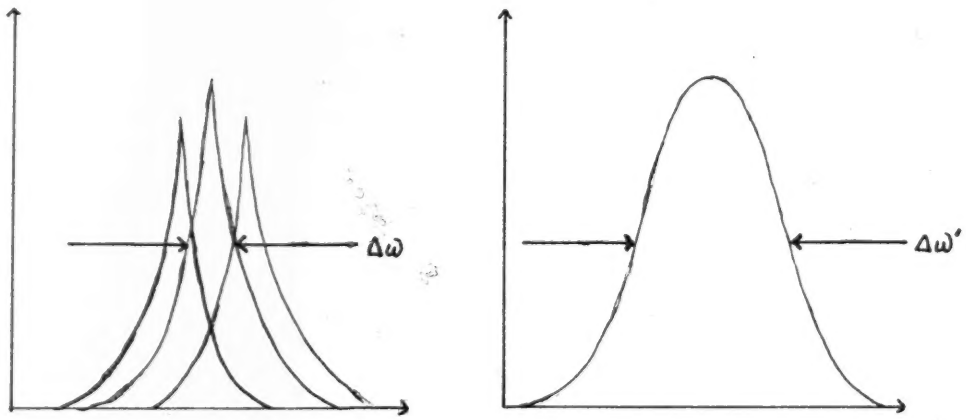

Fig 2.9 Illustration of resonance peak broadening. Different resonance conditions lead to multiple peaks which increase the width Δω.

the ferromagnet). Non-uniform modes of excitation serve to broaden the absorption peak due to the differing resonance frequencies as shown in figure 2.9, and can thus give erroneously high values for the damping. Patton has overcome this problem[2.37] by using more than one microwave frequency to obtain a set of absorption curves by which the non-uniform mode excitations may be removed.

Needless to say, the resonance frequency is highly dependent on the field each spin feels inside the ferromagnet. The intricacy of H has already been discussed so it's easy to see how the oscillation conditions can be quite complicated and even vary across a single thin film (this fact will become significant to our results). Vonsovskii discusses, among other things, the effect of many different parameters on the resonance frequency[2.3], including shape, crystal anisotropy, and domain structure. Some recent work gives an aspect of spatial resolution to the FMR experiment by measuring an array of non-interacting particles[2.38] and even undertakes some discussion of the magneto-static mode effects (non-uniform modes).

Our experiment uses a pulsed excitation applied to the sample instead of a sinusoidal one (akin to pulsed-NMR). This has the disadvantage (or advantage) of introducing a band of frequencies for excitation. Monitoring of the oscillations can be done directly by observing the magnetization of the films. In fact, with the time resolved scanning Kerr effect microscopy (TR-SKEM) system described in "time resolved set-up", we can spatially localize response detection and possibly even see differing resonance in differing locations for the non-uniform case. This has the advantage over the bulk FMR of looking at small particles. It has the advantage over particle arrays of looking within a single particle (spatially) and directly observing magneto-static mode effects. Finally, TR-

SKEM is not limited to FMR information; the temporal resolution (with the spatial resolution) allows elucidation of all dynamical problems.

2.7 Introduction to the Magneto-optic Kerr Effect (MOKE)

In its most basic form, the magneto-optic Kerr effect is the interaction of electro-magnetic radiation with a magnetic field upon reflection from an interface. MOKE is one of a class of magneto-optic effects including the Faraday effect (which takes place upon transmission through a magnetic material). Derivation of these effects are basically from solutions to the Fresnel equations that incorporate the magnetization of the material. In simple terms, one can think of an incident polarization vector (E_i) interacting with magnetization in a surface through the cross product $E_i \times M$. A rigorous derivation of the MOKE is omitted. Refer to Freiser[2.39], Robinson[2.40,2.41], Argyres[2.42], and Voigt[2.43] for more detailed discussion and derivation.

2.7.1 Definitions and reflectance coefficients

Consider the dielectric tensor for the magnetized slab[2.39]:

$$\begin{bmatrix} \kappa_1 & \kappa_2 & 0 \\ -\kappa_2 & \kappa_1 & 0 \\ 0 & 0 & \kappa_3 \end{bmatrix}$$

where off-diagonal elements contain the magnetic information. Other notations replace κ_2 with $\kappa_2 = -i\varepsilon Q$ where Q is the complex magneto-optic parameter and is a function of the material and wavelength of illuminating light (ε is the dielectric constant). The magnitude of Q (and κ_2) is proportional to H (or M inside the ferromagnet).

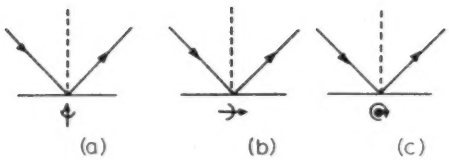

Fig 2.10 The orientation of magnetization M with respect to the plane of incidence (plane of the diagram) for **(a)** polar, **(b)** longitudinal, and **(c)** transverse Kerr effect[2.43].

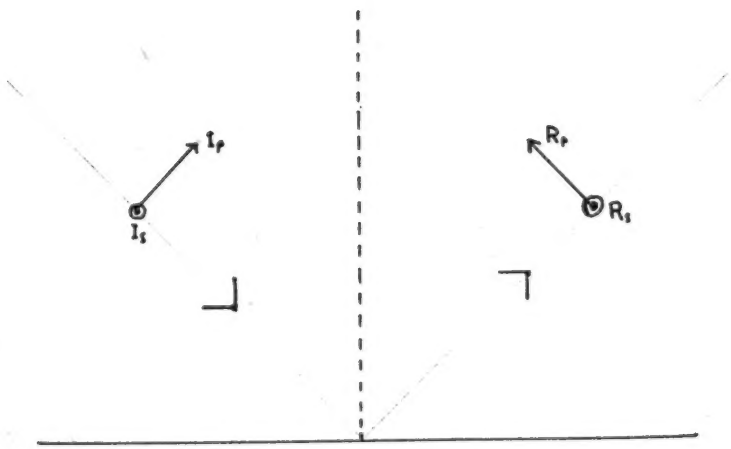

Fig 2.11 Definition of p- and s- polarized light and Intensity and Reflectivity I_p, I_s and R_p, R_s respectively; p-polarized light lies in the plane of incidence and s- polarized light is perpendicular to it.

There are three configurations for the MOKE (fig 2.10): polar, longitudinal, and transverse (sometimes named polar, meridional, and equatorial, respectively) depending upon the orientation of magnetization within the sample with respect to the plane of incidence and the surface normal (polar for M perpendicular to the surface, longitudinal for M in the plane of incidence and parallel to the surface, and transverse for M perpendicular to the plane of incidence). The definition of p- and s- polarized light is also given in figure 2.11 with p-polarized light lying in the plane of incidence and s-polarized light perpendicular to it. The reflectance coefficients[2.39] (or Fresnel coefficients) for the three configurations are given below (to first order) where θ is the angle of incidence, n is the index of refraction of the magnetic material and κ_2 is the off-diagonal element in the dielectric tensor ($|\kappa_2| \propto |M|$):

polar and longitudinal: $$r_{pp} = \frac{n\gamma - \gamma'}{n\gamma + \gamma'} \qquad r_{ss} = \frac{\gamma - n\gamma'}{\gamma + n\gamma'}$$

polar: $$r_{sp} = r_{ps} = \frac{\kappa_2 / n}{(\gamma + n\gamma')(n\gamma + \gamma')}$$

longitudinal: $$r_{ps} = -r_{sp} = \frac{\gamma\beta}{n\gamma'}\left[\frac{\kappa_2 / n}{(\gamma + n\gamma')(n\gamma + \gamma')}\right]$$

transverse: $$r_{pp} = \frac{n\gamma - 1}{n\gamma + 1}\left\{1 + \frac{\sin(2\theta)\kappa_2 / n}{(n\gamma + 1)(n\gamma - 1)}\right\}$$

$$r_{ss} = \frac{\gamma - n}{\gamma + n} \qquad r_{sp} = r_{ps} = 0$$

$$\gamma = \cos\theta \qquad \gamma' = \cos\theta' = \sqrt{1 - \frac{\sin^2\theta}{n^2}} \qquad \beta = \sin\theta$$

where $\begin{pmatrix} R_p \\ R_s \end{pmatrix} = \begin{pmatrix} r_{pp} & r_{ps} \\ r_{sp} & r_{ss} \end{pmatrix} \begin{pmatrix} I_p \\ I_s \end{pmatrix}$ is the complex reflectivity matrix for incident intensity $\begin{pmatrix} I_p \\ I_s \end{pmatrix}$.

As can be seen in the above equations, in the polar and longitudinal case, pure s- or p- reflected modes (s- to s- and p- to p-) are not affected by the sample magnetization, however mixed modes (p- to s- or s- to p-) are introduced with reflection proportional to M. κ_2 also introduces a phase shift, in general, with the result that incident linearly polarized light becomes elliptically polarized with a rotation of the major axis proportional to the magnetization. It is this rotation of polarization that most measurement schemes of the MOKE try to detect and interpret as magnetization at the surface. In the case of the transverse Kerr effect, there is no mixing of polarization states (and thus, no rotation) though there is a linear effect on the pure p- reflected intensity (and phase) with the surprising result of elliptically polarized light with no rotation but a small change in intensity. In our case, we concentrate on detection of polarization rotation so limit our measurements to polar and longitudinal Kerr effects.

Both effects allow larger rotations for p- polarized light. This is true because p- to p- reflectance (r_{pp}) is always less or equal to s- to s- reflectance (r_{ss}) but the magnitudes of r_{sp} and r_{ps} are the same so crossed modes have more of an effect when in vector addition with the smaller r_{pp} (giving larger rotation). Also mixed incident polarized-light (not pure p- or pure s-) should be avoided as off-diagonal terms are introduced that are independent of κ_2 (that is rotation non-magnetic in origin). The equations also tell us that the Kerr effects are a function of angle (the longitudinal effect has a broad maximum around 60°). Along with the magneto-optic parameter being dependent on material and wavelength, this gives a wide range of variation for Kerr rotation; several studies have been done on

permalloy to this effect (see, for example, figs 2.12 and 2.13). Finally, the polar effect is, in general, five to ten times larger than the longitudinal effect and is thus easier to detect in practice.

2.7.2 Generalized scanning Kerr effect microscope (SKEM) set-up:

Figure 2.14 generalizes a MOKE set-up. Light reflects off the surface defining some angle and plane of incidence from zero to ninety degrees and rotation in the plane of polarization is detected. We will begin the discussion with the reflection portion of the apparatus.

In general, light could be collimated as it strikes the surface (giving the advantage of one defined angle of incidence) or it could be focused and recollected by regular optics for an improvement in spatial resolution. For very high spatial resolution a microscope objective (μO) is needed, but this is hard to set at an oblique angle to the sample because two bulky μO's won't fit side by side. This is no problem for the polar case, in fact, we prefer the angle of incidence to be zero to maximize the signal. Light would need to come in and out on the same path, but this can be solved by using a beamsplitter. When we want to measure the longitudinal effect, we must have a non-zero incident angle which can be accomplished in two ways (figs 2.15 and 2.16). If we block half of the light falling on the μO aperture (either before or after the beamsplitter) the circular symmetry will be broken and light will have a net non-zero average angle of incidence and an average plane of incidence perpendicular to the cut (fig 2.15). The same could be achieved by using a mirror edge to illuminate half the aperture (fig 2.16) giving the advantage of four times the intensity (not having the beamsplitter twice).

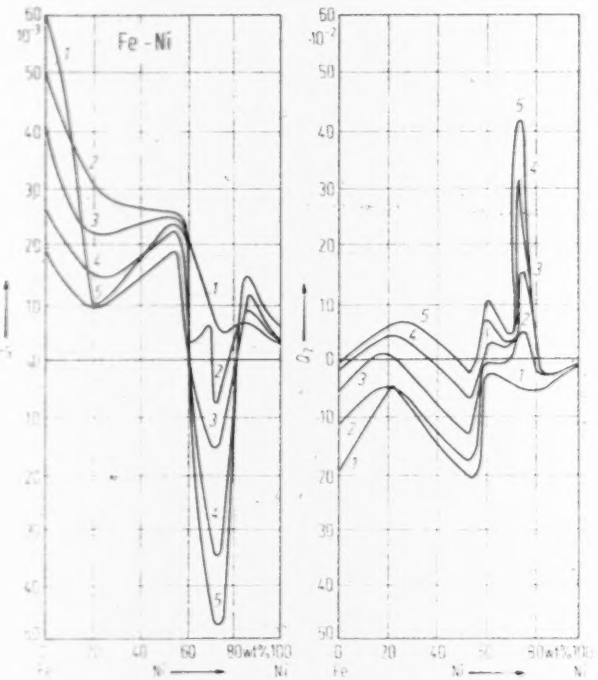

Fig 2.12 Components of the magneto-optical parameter $Q=Q_1-iQ_2$ as dependent on the composition of Fe-Ni alloys for several wavelengths of the light, as derived from the transverse Kerr effect. Curve 1:6700A, 2:6000A, 3:5400A, 4:4700A, 5:4400A[2.44].

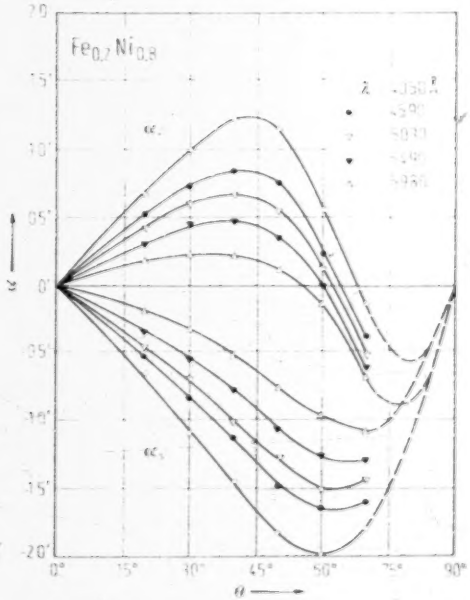

Fig 2.13 Longitudinal Kerr rotation angles α_s and α_p for light polarized normal or in the plane of incidence, repectively, as dependent on the angle of incidence θ for $Fe_{0.2}Ni_{0.8}$. The wavelength of the light is a parameter. The sign of the Kerr angle is chosen positve when the rotation and the direction of the reflected beam form a right-handed screw[2.44].

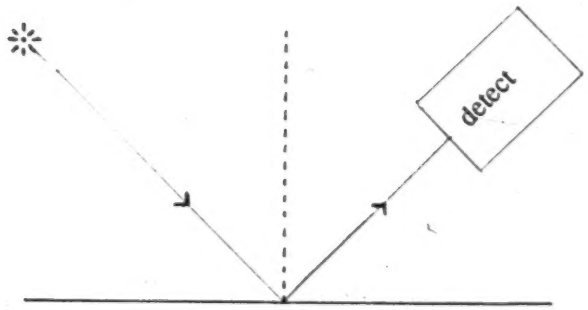

Fig 2.14 Idealized MOKE set-up. The rotation of the plane of polarized light reflected off a surface is detected.

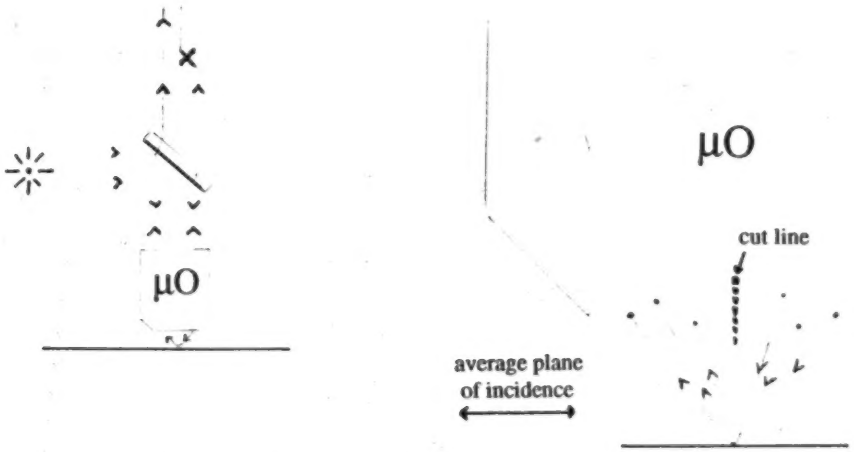

Fig 2.15 Schematic illustrating blocking of half the beam. A range of angles of incidence (and planes of incidence) accompanies focussing with the μO. The average plane of incidence will be perpendicular to the cut line and net average angle of incidence will be non-normal. Cutting may occur before the beam-splitter as well.

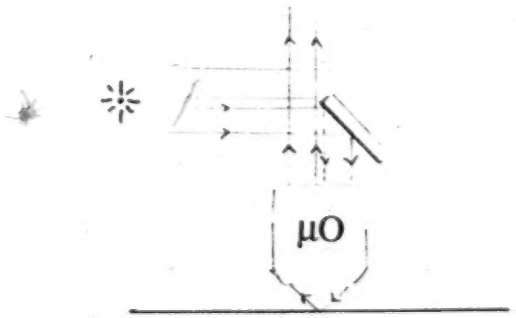

Fig 2.16 Schematic showing beam cutting by illuminating a mirror on its edge (a "half-cut" mirror).

We now consider the means of detection. As has been mentioned, measurement of polar or longitudinal effects is by detection of polarization rotation. The problem is that this rotation tends to be very small for most materials (the Faraday effect is easier to see simply because of the distance of material traversed: centimeters through some insulators as opposed to the 20 nm optical depth for reflections from metals). The most obvious way to measure a signal would be to cross two polarizers (polarizer and analyzer) before and after the interaction (fig 2.17) though this detection near extinction makes signal to noise a problem and demands zero stray light on the photodetectors (the detectors could be photomultipliers or, more likely, photodiodes (PDs)). Also, a change in the polarization leads to a quadratic change in intensity which is extremely small for a small angle. The signal can be doubled in a split beam differential set-up[2.45] in which a Glan-Thomson cube is set 45° with respect to the initial polarizer to give two beams of equal intensity (fig 2.18) which are subtracted electronically. A small rotation in polarization increases the intensity in one beam and decreases (fig 2.18 inset) it in the other giving twice the signal (this technique makes extinction electronic not photonic so stray light doesn't spoil the measurement and signal to noise is improved). Furthermore, 45° is the point of maximum slope of intensity change vs. angle giving the maximum signal per rotation. Other attempts at improving the signal include "blooming the sample" in which an anti-reflectivity coating like zinc sulfide is deposited on the surface[2.46,2.47]. Attempts to subtract out background noise were also done since non-magnetic rotations and background can easily swamp the signal: Fowler and Fryer took a transparent positive in the magnetic saturated state (with photodetection by photographic plate) and superimposed a negative without magnetic saturation[2.48]. A more recent iteration of this

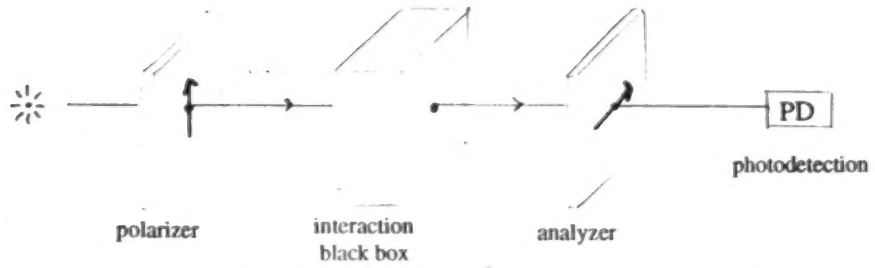

Fig 2.17 Crossed polarizers detection system. Any polarization rotation due to the black box increases the signal at photodetection quadratically.

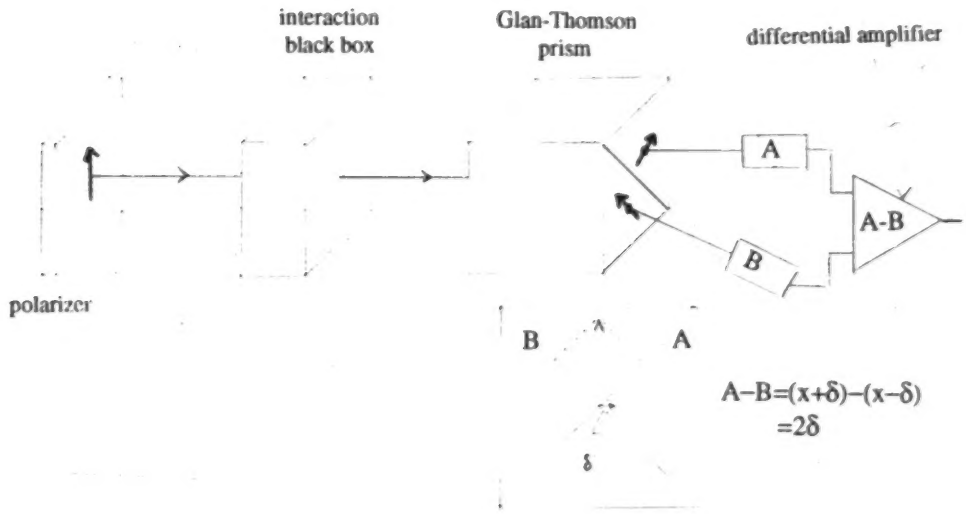

Fig 2.18 Split-beam subtraction using a Glan-Thomson prism. Background is still subtracted and rotation increases the signal linearly (inset).

idea is CCD imaging in which images of the sample are taken with and without magnetic field and immediately subtracted[2.49,2.50,2.51]. These have been particularly successful since the whole image is captured at once removing the problem of drift in a raster scanning system. Images may also be improved with time-averaging and image processing.

In general, though, the signal is too small, so modulation and synchronous detection is necessary. Light polarization modulation is an elegant way to achieve this and readily allows static imaging. Robinson uses a Faraday cell with an ac electro-magnet to modulate the magnetization in the cell along the optic axis[2.41] (which is passed onto the light as a Faraday rotation). Jasperson and Schnatterly modulated the light photo-elastically using a strain wave in a quartz crystal[2.52]. In our work, we use a commercial instrument, the Photoelastic Modulator (PEM), which stems from Jasperson's research. A strain wave in one dimension retards one component of electric field by $\lambda/2$ with respect to the other. In our case, rotation is picked up at $2f$. This technique has the advantage of being very sensitive to rotation and very versatile for ellipsometry (circular polarizations and rotations can be detected for different configurations of analyzer angle and f or $2f$ detection). The drawback to the above techniques is that they directly modulate the light which may be undesirable. More will be discussed on this in chapter 7.

Modulation of the magnetic field at the sample also serves for synchronous detection. Lee et. al. applied an ac magnetic field to image domain walls as the boundary moved back and forth across the light spot[2.53]. Re and Kryder drove a magnetic recording head with its own coils to check its magnetization response as a function of frequency[2.54]. In the time resolved case, "slow" (kHz) modulation is given electronically to a series of fast tipping pulses[2.55]; more will be discussed on this in the chapter 7.

3 PROPERTIES OF NiFe (PERMALLOY)

There is a very extensive body of literature on the properties of NiFe. Arnold opened a huge field of interest (known as "the permalloy problem") in 1923 when he found (78.5%/21.5% Ni/Fe) permalloy had high permeability only when quenched from 600 C[3.1]. Pioneering experimental work in the field was done by Elmen[3.2] and Dillinger and Bozorth[3.3] with temperature and magnetic annealing ideas. Several review papers have been written on the subject including works by Pfeifer and Radeloff[3.4], Chin[3.5], and Freedman[3.6]. Several classic papers are also cited including Hall[3.7], Ferguson[3.8], and Bozorth and Walker[3.9]. Finally, some good reference texts include Chikazumi[3.10], Thomson[3.11], and Prutton[3.12]. With the excellent reviews already done, it is the author's intention to merely touch on important parameters for this work.

3.1 "81/19" Permalloy

"81/19" permalloy falls into the category of "soft" magnetic materials. That is, it has high saturation magnetization ($4\pi M_s$=10000 G) and low coercivity (H_c<2 Oe). Furthermore, it can be made to have extremely high maximum permeability (100000). Other parameters that are important for technical reasons include uniaxial anisotropy K_u, crystalline anisotropy K_1, and magnetostriction λ_{111}, λ_{100}, and λ_s (λ_s is saturation magnetostriction). All of these properties are functions of various factors including stoichiometric makeup of the alloy, temperature annealing and type of cooling, substrate temperature, magnetic annealing, induced strain, cold rolling, grain size, and substrate or seeding layer and all properties may be selected and controlled (though not independently).

3.2 Annealing and Magnetic Annealing (Historical Work)

Let us discuss first the annealing and magnetic annealing effects. Figure 3.1 shows the effect on initial permeability of three different heat treatments as a function of Ni-percentage[3.11]. The treatment labeled "b" consisted of annealing at 900-950 C for 1 hour and cooling at a maximum rate of 100 C/h. The treatment "a" is a double treatment of "b" followed by reheating to 600 C and quenching in air on a copper plate (cooling about 1500 C/min). Treatment "c" comprised of a bake at 450 C for 20h after heating to 900-950 C. Figure 3.2 shows the effect of "field annealing" (slow cooling in a field) as a function of %Ni[3.2,3.3,3.11] (this time, on the maximum permeability μ_{max}). The field annealing[3.3], labeled "a", has substantial affect only for Curie temperature θ above 450 C. A rapid cool[3.2], "b", is given for comparison. Such treatments are probably tapping into ordering or disordering effect in the permalloy (slow or fast cool).

More effects for temperature annealing are given in figures 3.3 through 3.6. Bozorth and Walker[3.9] find the magnetocrystalline anisotropy K_1 has a definite dependence on cooling rate with the largest effect being for samples showing most long range order (Ni_3Fe) in figures 3.3 and 3.4. This long range order also affects the magnetostriction for the quenched or baked case in figure 3.5[3.9] (though not as pronounced). Similar reasons are cited for the success of cold rolling (really magnetostrictive deformation) and strain induced K_u. Ferguson finds an effect for uniaxial anisotropy K_u on the annealing temperature[3.8] in figure 3.6 and Neel discusses how short range ordering or "pairing" of Ni-Fe atoms could cause annealing and magnetic annealing effect on K_u[3.13]. Fujii et. al. give a very interesting analysis on the origin of induced uniaxial anisotropy[3.14]. By

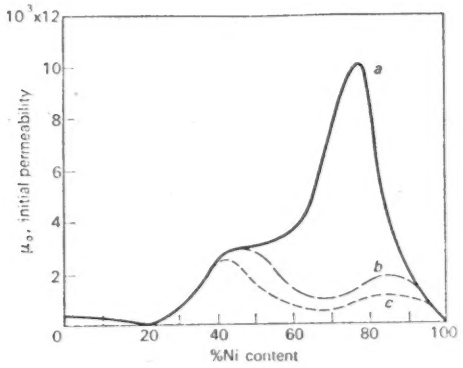

Fig 3.1 The effect of various heat-treatments on the initial permeability of various nickel irons: **(a)** double treatment, **(b)** furnace cool, and **(c)** bake[3.11].

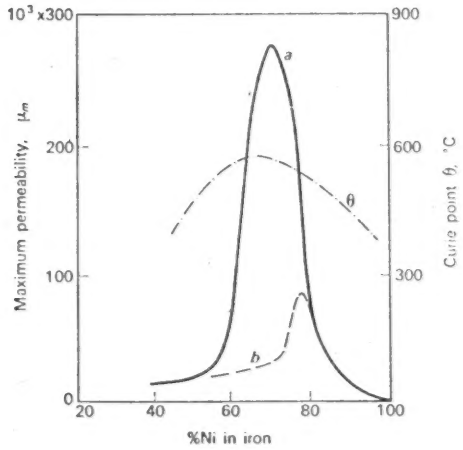

Fig 3.2 The variation of maximum permeability with composition for two rates of cooling after annealing at 1000 C: **(a)** slow cool in a field, and **(b)** rapid cool[3.11].

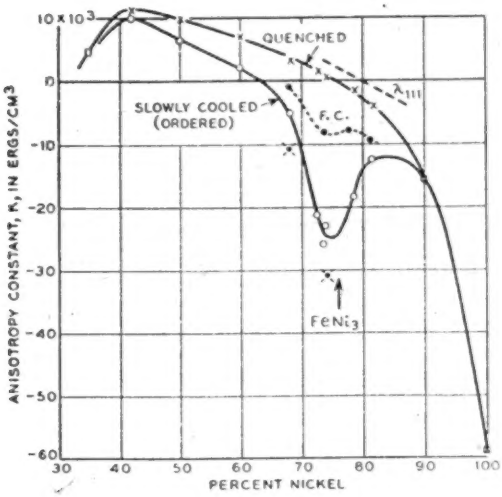

Fig 3.3 Magnetic anisotropy constants of quenched and of slowly cooled NiFe. Approximate rates of cooling are 10^5 and 2.5 C/hr respectively, from 600 to 300 C. Broken line F.C. shows values for 55 C/hr. Line λ_{111} shows composition at which magnetostriction in [111] direction goes through zero[3.9].

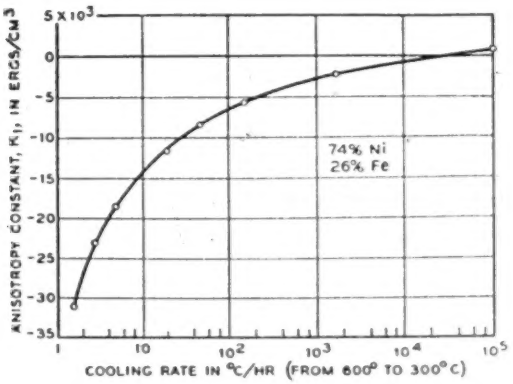

Fig 3.4 Anisotropy constants of 74 % Ni crystal as dependent on rate of cooling from 600 to 300 C. Highest cooling rate is approximate[3.9].

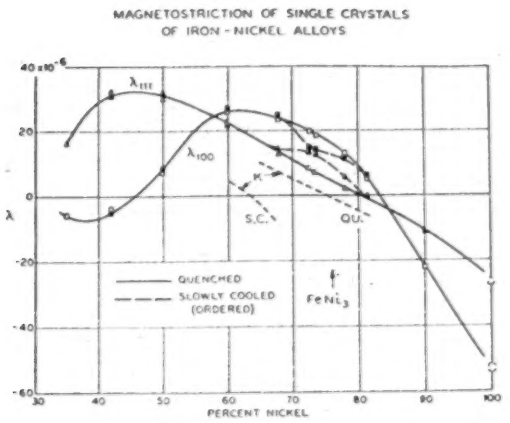

Fig 3.5 Magnetostriction of quenched and of slowly cooled alloys. Broken lines show compositions at which anisotropy of quenched (QU.) and slowly cooled alloys (S.C.) goes through zero[3.9].

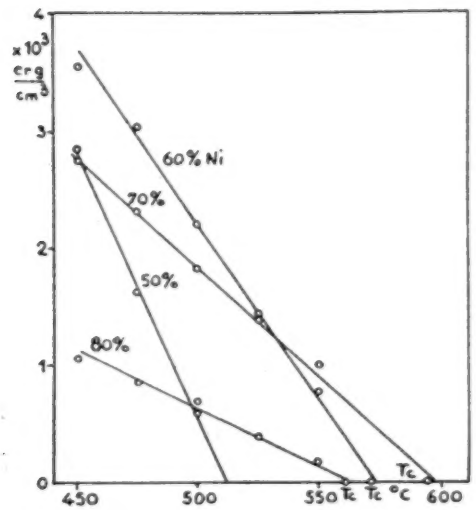

Fig 3.6 The dependence of the induced uniaxial anisotropy on the annealing temperature[3.8].

considering H_k as a function of annealing time they were able to identify six different contributions to the isothermal relaxation process and associate a relaxation time (and activation energy) to each which they could further relate to magnetostrictive induced, defect induced, and crystalline order induced uniaxial anisotropy.

3.3 The Technically Interesting Range of 70-90% Ni Content

Figure 3.7 shows a blow-up of figure 3.6 in the region where cooling rate has strong effect. This range of Ni content between 70 and 85 % is also technically interesting for several reasons as the zeros of λ and K and the maximum permeability all lie in this range. It is important for magnetic recording to have zero or small magnetostriction effects since wall motion will be easier (and quicker) especially along the easy axis direction (which is often <111>). Low anisotropy also means reversal is more likely to be by coherent rotation which is also desirable and quicker (see chapter 2). The combination of the two leads to high permeability, another positive feature. For these reasons much work has been done on tracking the zero lines of these parameters. From the physics point of view we choose permalloy of these qualities (e.g. 81/19) to tie research to technical interests. It is also important to have low anisotropy and low magnetostriction to more easily model time resolved reversal effects for comparison with experiment.

Thomson[3.4] summarizes several important features from Bozorth and Walker[3.9] in table 3.1. These features take place close to each other in this range but it should be noted that none overlap in the binary alloy (NiFe). However, with small additions of some non-ferromagnetic elements, the zeroes of anisotropy and magnetostriction can be made to occur simultaneously. Figure 3.8[3.4] and 3.9[3.5] show crossing zero lines for the addition of

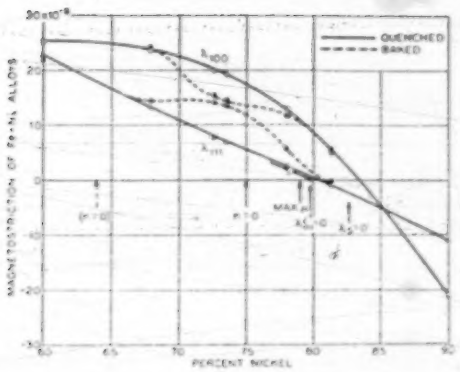

Fig 3.7 Magnetostriction of alloys in range 60 to 90 % Ni, showing unique points in series. Single point near λ_{111} curves is for specimen containing 0.5 % Mn[3.9].

Table 3.1 Some magnetic constants for single crystals of quenched NiFe alloys[3.9, 3.11].

Composition % Ni	K_1(10^3 ergs/cm^3)	λ_{100}($\times 10^{-6}$)	λ_{111}($\times 10^{-6}$)	Feature
75	0	18	6	$K_1 = 0$
78·5	−1·7	11	1	Highest μ_0
80	−2·5	9	0	$\lambda_{111} = 0$
82	−4·0	3	−2	$\lambda_s = 0$
83	−5·0	0	−3	$\lambda_{100} = 0$
85	−7·0	−5	−5	$\lambda_{100} = \lambda_{111} = \lambda_s$

Mo and/or Cu. Several lines are given for K_1 for both the case of different tempering and different cooling (ordering concerns have less of an effect on magnetostriciton).

Coercivity H_c and anisotropy field H_k are also important parameters which have interesting or unique points in the range 75 to 90% Ni. They are preferably lower for easier switching. Freedman discussed the dependencies of H_c and H_k on thickness, grain diameter, deposition method, annealing or deposition temperature, underlayer, and substrate temperature (fig 3.10)[3.6]. Motivation for our choice of 81/19 Ni% becomes clear in light of the above discussion. It should be noted that, in the case of permalloy, percentages are almost always given as a weight percent as opposed to atomic percent and will be referred to as such in this work.

The range of 50/50 Ni/Fe should briefly be mentioned here. This range of alloy of NiFe is much more resistive than 80/20, thus it speeds eddy current decay considerably so is of current technical interest in eddy current speed limited magnetic recording heads.

3.4 Recent Work in Property Engineering

Having this large body of literature to draw from by no means makes property engineering straight forward. More recent papers have continued to fill in data gaps (sometimes in contradiction to previous works) and add new methods for property control. Tsunashima et.al. have mapped out the thickness dependence of magnetic annealing behaviour[3.15] and Koo and Kasiraj have looked at magnetic annealing effects as well[3.16]. Krush has investigated the effects of sputter gas (1% N2 addition to Ar) and substrate biasing on λ_s[3.17] (with the ability to lower H_c). Takahashi et. al. apply a surface acoustic wave (SAW) to the substrate during deposition to change grain size dramatically and control H_c and H_k[3.18]. Nakatani et.al. and Gillies et. al. have used Nb, Ta, Ti, Zr, and

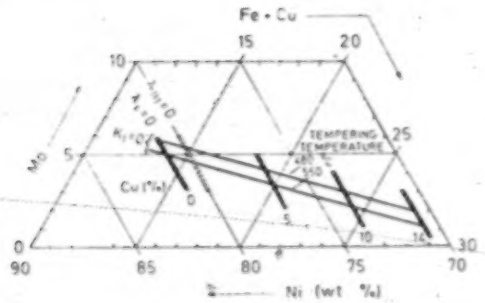

Fig 3.8 Lines for $K_1=0$ and $\lambda=0$ in Ni-Fe-Cu-Mo system[3.4].

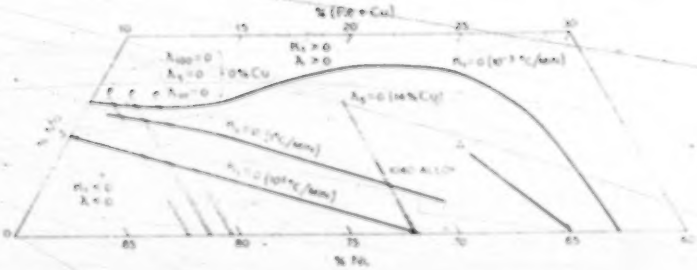

Fig 3.9 Nickel corner of Ni-Fe-Mo alloys in which Cu is substituted for Fe. Room temperature lines of $K_1=0$ for three cooling rates, and lines of $\lambda=0$ for 0 and 14 % Cu. At cryogenic temperatures, the $K_1=0$ lines are displaced toward the lower left. Line A alloys are highly responsive to magnetic annealing[3.9].

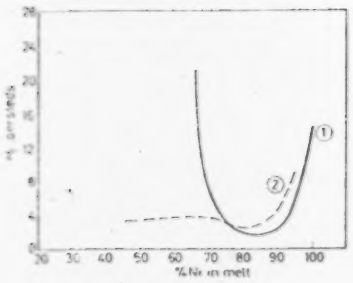

Fig 3.10 Wall coercivity of Ni-Fe alloys as a function of composition (of melt). Curve 1, evapourated films: 1000 A thick, substrate temperature 200 C. Curve 2, electrodepisited films: 1000 A thick[3.6].

Hf as buffer or seed layers to enhance <111> growth and minimize the effect of anisotropy[3.19,3.20]. Kim et. al. use ceramic intermediates to affect properties[3.21] and Grimes and Lee can enhance complex permeability using $Co_{79}Cr_{21}$ undercoats[3.22]. Finally Kim and Silva find abrupt increase in $|\lambda_s|$ for thicknesses below 7nm[3.23].

The complexity of permalloy and magnitude of parameter control techniques in the 80/20 range has been demonstrated in this chapter. Motivation for the choice of 80/20 permalloy has also been given. Discussion of the deposition and characteristics of our permalloy films will be given in chapters 5 and 6.

4 FABRICATION DESIGN

4.1 Introduction

In order to probe the dynamical properties of a range of sizes and shapes of permalloy microstructures, we needed to be able to magnetically excite these structures with ultrafast fields. This necessitated a concentrated, transient magnetic field pulse to occur in the sample. It needs to be in a perpendicular direction to the thin film substrate and ultrafast[4.1] (this necessitates an optical current switch). Photomasks would be made for photolithographic fabrication of appropriate features to fill these needs.

4.2 Mask 1: Lithographic Coils and Dots

Layout for this mask is in the appendix. The main mask for photolithographic fabrication was designed to have as much versatility as possible. The basic principle would transform a current transient into a magnetic field transient, perpendicular to the substrate, by using a one-loop conducting coil with transmission line leads (ultrafast current generation will be discussed in the next section) following the patterns of Mark Johnson[4.2].

In our case, seven different coil types were made with four different inner/outer diameter combinations: 8/12 (# 3, 5, and 7 in fig), 8/16 (# 2 in fig), 16/24 (#1 and 4 in fig), and 16/32 (#6 in fig) respectively (all diameters in micrometers). Their placement in the photomask "die" is shown in figure 4.1; smaller coils were closer to the center of the die as the lithographic process was alleged to give better resolution in the center if centered over a small substrate . This was not a necessary precaution in our case, because

the substrate could be placed under any part of the die in the mask. Coil # 7 had a 4x4 μm square in the center, coils 3 and 4 were to have 4 and 8 μm circles inside but the photomask company (Microtronics) erred in production. The different diameters allowed different possible conditions for transient magnetic field: the thicker line width coils could carry more current but would be less localized in magnetic field production than the thinner ones, and the two types of inner diameter allowed for two scales with the smaller coil able to give more concentrated fields for smaller particles. We wound up using coil #6 almost exclusively because it was the biggest and easiest to work with and the fields produced were adequate.

The layout was to allow any of the twenty-four particles from section 8 in figure 4.1 to be placed in the center of any coil with a subsequent lithography step by rotating the photomask and realigning (fig 4.2). Again more intricate or smaller features were made closer to the center. Only the three pointed alignment structures are visible with the magnification in this figure. These alignment marks correspond precisely with marks surrounding the coils; when overlapped a particle will be aligned in the center of a coil loop. Particles included 2, 4, 6, and 8 μm diameter squares and circles and a 10 μm diameter circle, 2x4, 2x8, 2x10, and 1x14 μmxμm rectangles in both orientations, 9, 6, 3 μm on a side equilateral triangles, 1 isosceles triangle, 3, 4, and 6 pointed stars, and a hexagon (see appendix for layout) but here also, several features (circles and squares) were lost by Microtronics, which was especially unfortunate as one of the things we most wanted to do was look for any dynamical scaling in circles and squares from 10 to 2 μm.

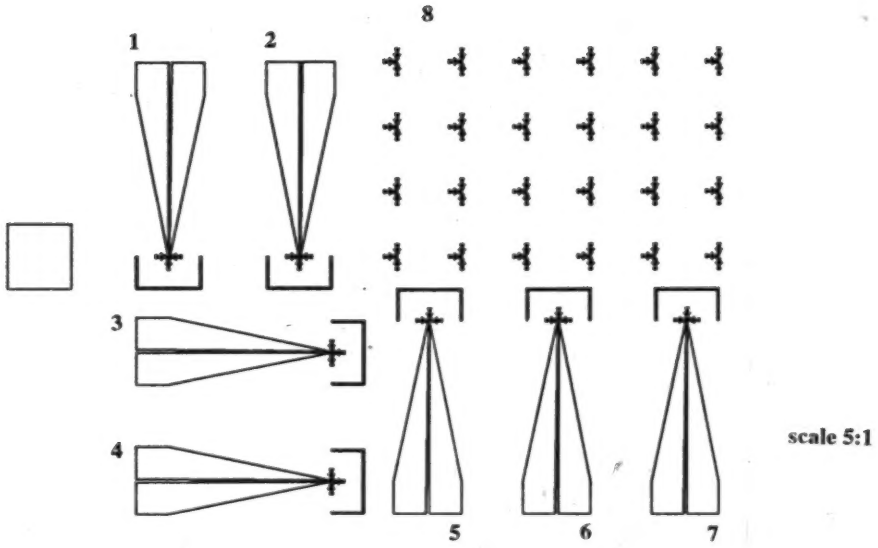

Fig 4.1 Layout of seven different coil combinations in the photomask "die". Coils #3, 5, and 7 are 8/12, coil #2 is 8/24, coils #1 and 4 are 16/24, and coil #6 is 16/32 inner/outer diameters respectively (in μm).

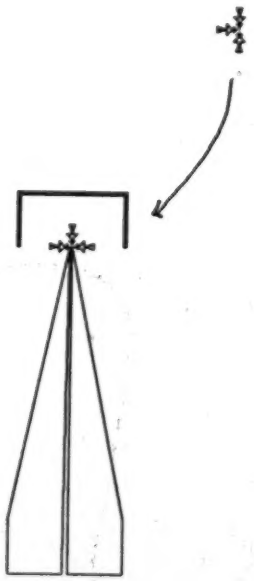

Fig 4.2 Selected microstructure placement by "double lithography": rotation and alignment of the triangular marks.

4.2 Mask 2: Photoconductive Switches

This design was also modeled after a source[4.3] and the layout is given in the appendix. The photoconductive switch is necessary to turn a laser pulse into an ultrafast electrical transient (photons generate electron-hole pairs across the band gap of a semi-conductor substrate allowing brief current flow in a thin layer, the optical depth (a few x100 nm for GaAs)). Interdigitated fingers allow a large surface area of semiconductor to flow charge at once giving a large current pulse. This pulse's temporal shape depends on the laser pulse width for its rise time and the carrier recombination time for its decay (though the rise time may be broadened by dispersion and reflections by the time it reaches the coil). For more information on photoconductive switches refer to Auston[4.4].

In each "3-set" die (fig 4.3), there are 2, 4, and 6 μm wide fingers and gaps in the 3 switches, respectively. These should each give slightly different response (still looking for versatility). The three switches are close together so that they could be bonded into the same circuit if one is blown (this function was never used in practice and each switch was individually diced). The original design had 100 μm bonding pads on each end of the switch; in our case, some had 100 μm pads and others had 300 μm pads which are much easier to work with. Because we had characterized its response (and it always survived well in lithography) we wound up using the switch with 6 μm fingers exclusively.

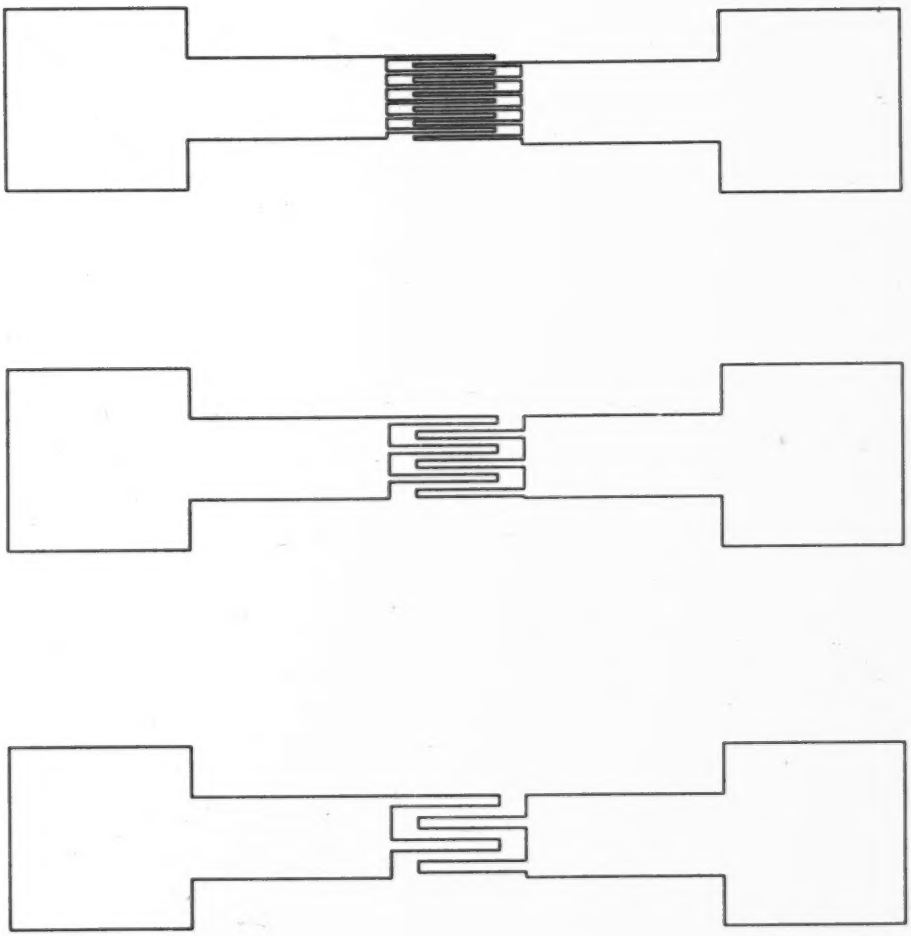

Fig 4.3 Photoconductive switches "3-set". The width of fingers is the same as the spacing between fingers in each switch. Widths include 6, 4, and 2 μm for 4, 6, and 12 fingered switches, respectively.

5 FABRICATION

5.1 Introduction

The idea behind fabrication was simple: transfer the pattern of the microcoil to a conducting thin film and transfer a shape pattern into permalloy at the center of the coil. Ways that these transferences occur are detailed in this section including: deposition of conducting and permalloy layers and pattern transfer through combinations of photolithography, wet chemical etching, "double lithography", ion-milling, electron beam lithography (ebl), and lift-off process.

5.2 Deposition

5.2.1 Conducting Layer

The final choice for conducting layer wound up being gold because it is highly conductive and the fabrication processes for it were well worked out at AMC. This became the choice of thin film for both the conducting coil and the interdigitated photoconductive switches. Gold needs an adhesion layer to glass and GaAs (the two substrates used for the coils and switches, respectively). Ti is always used as the adhesion layer in the case of GaAs; for adhesion to glass, either Ti or Cr had been used (Ti etch will etch glass, but was never a major problem). Also some multiple depositions were done in ultra-high vacuum (UHV) of Ti/Au/Ti/Py and Ti/Au/Py (where Py = permalloy). A Ti/Py beveling technique was known[5.1] as well as the use of Ti as a <111> seed layer for permalloy[5.2,5.3]. Early depositions of Ti/Au were done by electron beam evapouration but

the quality was always questionable. Now all Ti/Au (and Cr/Au) depositions are done in a commercial sputtering system (Perkin Elmer) at AMC. In general, thicknesses are 50 or 100 A adhesion layer and 1000 to 3000 A Au. As mentioned some Au depositions were done in UHV (especially for the multiple films) at 5 mtorr and 10 SCCM Ar. Though adhesion seemed fine, the quality was questionable as coils of this type were known to blow up more often and the UHV sputtering process was never finalized for Au.

5.2.2 NiFe layer

5.2.2A Electron-beam evapouration

The permalloy deposition process took a little longer to figure out. First attempts were with rf induction melted e-beam evapouration of powder mixtures of Ni and Fe in a graphite crucible. The induction melted permalloy target was also machined into a starter source, for use with the electron beam, and etched, for purity reasons. The base pressure of these was not spectacular (mid 10^{-6} torr) and the deposition rate was quite low (~2 A/s) so there was always large concern of contamination, especially oxygen contamination. A magnet was placed right behind the upside down substrate to induce uniaxial anisotropy but was sometimes found to twist during deposition due to the e-beam. There was also concern about the deposition system; being "well-used", it had many loose large particulates, many of which could become magnetized, so several films were ruined by attraction of these to the surface. Nonetheless, a couple of magnetically good films (but high resistivity) resulted from this type of process showing excellent hysteresis characteristics which will be discussed in section 6.4.2.

5.2.2B Perkin Elmer sputtered permalloy

One deposition run of permalloy was done using the commercial Perkin Elmer sputter system at AMC. The properties of these films were very questionable, though they were not suspected right away. Films exhibited very high resistivity (~400 μΩ-cm) and unidentifiable hysteresis loops using both the homemade hysteresis system (section 6.4.2) and the SQUID magnetometer (6.4.1). Unfortunately, these films were thought to be high quality and set back experimental work for quite some time including: calibration of the homemade hysteresis set-up, establishment of an etching process, and confirmation of the hypothesized resistivity. We believe they may have been full of oxygen and possibly non-ferromagnetic, forming a thick oxide on the surface.

5.2.2C Ultra-high vacuum (UHV) sputtered permalloy

To make the risk of oxygen contamination as small as possible, films were finally made using a UHV sputtering chamber to achieve very low base pressures. This proved to be a difficult process to set-up for several reasons.

First, the sputtering was done by a dc magnetron gun which contains the sputter plasma via magnetic field. Because the target that would be used (permalloy) has a very high saturation magnetization ($4\pi M_s$ =10000 G), the plasma containment would suffer. For this reason, a special highly magnetized sputtering gun was used. Other ways to get around dc sputtering magnetic materials (especially permalloy) have been discussed[5.4].

The second obstacle was how to have a sufficiently high in-plane field (~120 Oe) on the substrate in-situ to induce uniaxial anisotropy (discussed in chapter 3). The UHV

system was a two chamber system with a load-lock (the UHV chamber is not exposed to atmosphere regularly) so any magnetic assembly had to be small, self-contained, and UHV friendly, or it had to be external to the chamber. Helmholtz coils outside the chamber would be possible but would need to be very strong and would affect the field inside the whole chamber possibly ruining the plasma containment. A current flow induced magnetic field would give the best approximation of an in-plane field but would be hard to make and could also more drastically affect the plasma conditions inside the chamber (introducing a substrate bias). For these reasons, a magnet assembly was designed (for full description, see appendix).

The magnetic assembly was under definite size constraints due to the way the substrate was passed from the load-lock to the UHV chamber. Any extra material had to be directly behind the substrate and not to any one side. To make a perpendicular field this way would be easy as one pole of a large magnet would give fairly uniform conditions across a substrate. To make an in-plane field is more difficult. The way we chose to do it was to use several small magnets with their north and south poles head to tail lying in the plane of magnetization (fig 5.1). The magnets would serve as "point" dipoles and the field, some distance away at the surface, would average out to an in-plane field. Setting a line of these head-to-toe magnets side by side would fill out the plane. The magnets were sintered AlnicoV, designed to not outgas at the low pressures and to have very high Curie Temperature (850 C) to allow possible in-situ in-field temperature annealing of the films (chapter 3). The magnets could not be precisely head to tail (flux had to be allowed to escape some distance) so a gap was made of the order of the distance between the magnet plane and the substrate surface. A qualitative testing confirmed this and the magnetic

assembly was designed. Magnets were 0.500 inches long and the gap was 0.100 inches (fig 5.2). Two plates were made; one to contain the magnets and the other to be screwed on as a thin cover (1/16") on which would rest the substrate. Covers were made of both aluminum and stainless steel, though the aluminum cannot be used in UHV at higher temperatures (there was some concern about the weight of the magnetic assembly dragging down a load-lock transfer arm). The backing was made of copper for best heat conduction, though, in retrospect, stainless steel would have been better (it is sufficiently conductive and is "cleanest" with respect to outgassing). The backing was also tailored to have as little weight as possible and all components were made with mind for breathing (no blind holes, etc.) Small fasteners (both aluminum and stainless steel available) serve to hold on the substrate with stainless steel screws. Screw holes were designed to allow holding of several sizes of substrates up to slightly more than 2 inch squares. Small (<1 cm) substrates could also be fastened.

A quick and dirty determination of the biasing field strength was done with a gaussmeter held at the approximate height of the substrate surface. An interpolated chart is shown in figure 5.3 giving the approximate horizontal (in-plane) and vertical (normal) magnetic field components over the range of one cycle in the magnetic array (from center to center of two magnet rows). The horizontal field component is the one of interest and rises to about 200 Oe near the center of a magnet. It falls to 0 Oe near the ends and actually dips to -20 Oe in the gap. The vertical field could be troublesome if too large. It starts at zero in the center of the magnet and climbs to about 150 Oe near a pole. It then switches polarity in the gap and climbs to - 150 Oe on the other side. During deposition, areas of interest were purposefully placed near the center of a magnet to take advantage of

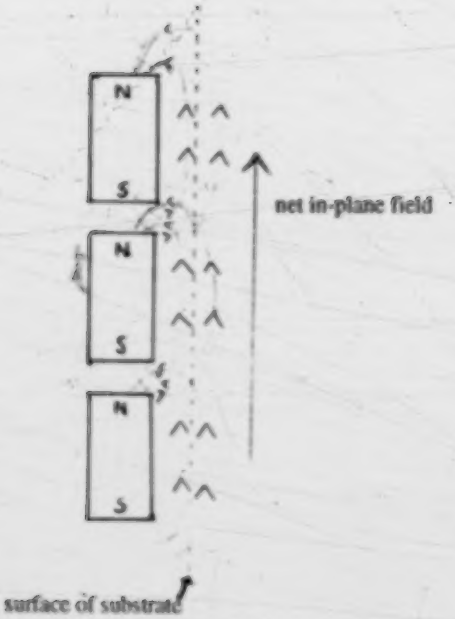

Fig 5.1 Cross-sectional cartoon view of an in-plane magnetic field assembly. The normal to the substrate plane is pointing to the right and the magnets are degenerate out of the plane of the paper.

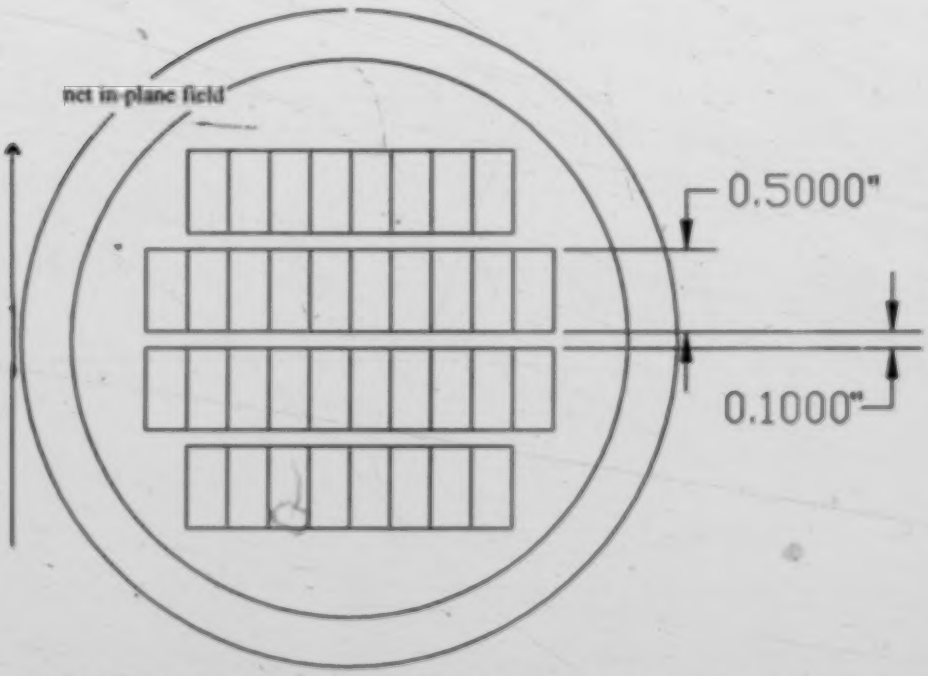

Fig 5.2 Frontal view of a magnetic assembly. The substrate plane is the plane of the page. Rows are 0.500" high with 0.100" gaps between them.

the high horizontal field and low vertical field. I would say that all samples of interest had at least 150 Oe external field during deposition and not more than 50 Oe perpendicular field.

Having solved these problems, the UHV sputtering turned out to give the best type of films and the films that gave most of our results. Sputtering itself is a tricky but repeatable process and I would like to stress that the work in this thesis was not sputter oriented, so the process arrived at was neither thorough nor exhaustive of the possibilities. The dc sputtering pressure is an important parameter as it determines what angle material will tend to come in at and its energy (mean free path in the sputter gas), the rate at which the material is sputtered off of the target, the amount of substrate sputtering, and the amount of sputter gas atoms trapped in the substrate. These points all affect the quality of the film in terms of purity, stress, adhesion, and type of film. I will not go into detail here about these processes. Some excellent references are: Thin Film Processes II by Vossen and Kern[5.5], which gives a clear and concise introduction and overview to sputtering, and Thin Film course notes by Brett[5.6], which gives more detailed account of subtle sputtering problems and techniques.

The deposition pressure was chosen to be 2.0 mtorr as an attempt to make a denser film (fig 5.4)[5.7,5.8]. Originally 5.0 mtorr was tried but these films peeled easily, presumably due to tensile stress. After success with 2.0 mtorr (no peeling), 1.5 and 1.0 mtorr were tried respectively (both near the limits of our dc power supply to hold a plasma) but these also peeled, most likely because of the compressive stress from the higher energy depositing atoms. The 2.0 mtorr pressure would also prove useful for successful lift-off processes with sputter deposition as the angle of incidence (measured

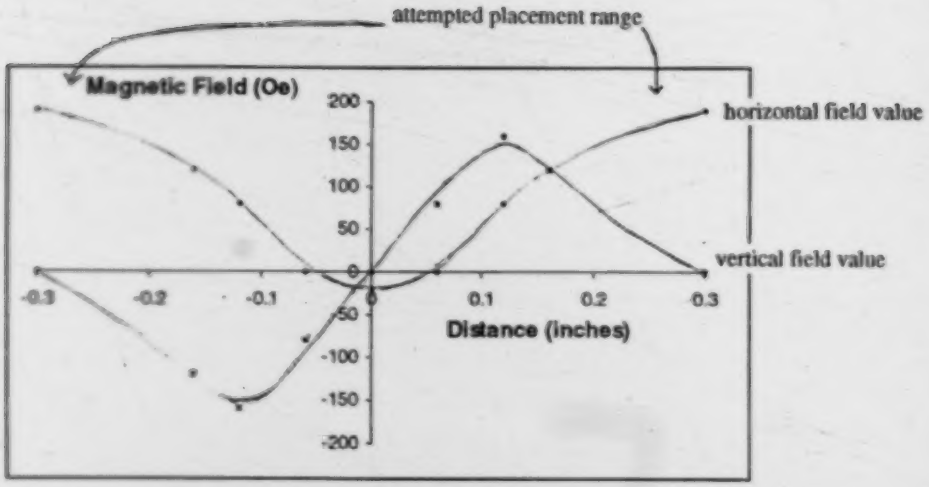

Fig 5.3 In-plane and normal magnetic field components of the magnet assembly as a function of position from center to center of two rows. Values given are very approximate.

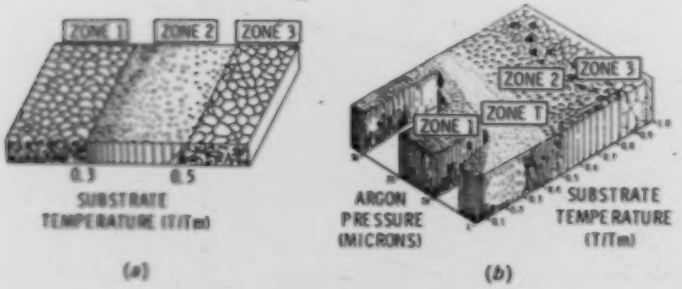

Fig 5.4 Structural zone models for coating growth. (a) Zones 2 and 3 are denser with less columnar structure[5.7]. (b) Zone T is a denser film resulting from sputter ions and neutrals "pounding" the film[5.8].

from surface normal) of sputter material is fairly low for this low pressure. Though the system was designed for possible substrate heating and substrate electrical biasing, both of which should improve the film quality (in terms of density, entering into zone 2 or 3), these techniques have not yet been tried. The parameters of the dc power supply were set at constant 300 mA and the voltage ranged around 420 or 430 V (giving power ~130 W) for the 2.0 mtorr deposition pressure. The argon flow rate was always 10 SCCM (standard cubic centimeters per minute); base pressures were usually in the 5×10^{-8} range.

Attempts were also made at multiple film depositions in the UHV chamber. Keeping in mind the possibilities of single time photolithography (obtaining the coil and the microstructure at the same time) and fearing the permalloy might not be conductive enough on its own, several multilayers of Ti/Au/Py or Ti/Au/Ti/Py were made. Both of these fulfilled the need for conductive and one-step lithography. The entirety of these films was questionable because of the gold layer (run at 5.0 mtorr with no other pressure trials) whose quality was always suspect. The titanium layers were good quality because their deposition process was well known in this particular UHV system, but the gold had never been done before in the system. The reasoning for making a Ti layer directly below the permalloy in some films was an attempt at inducing <111> order in the permalloy layer (as in chapter 3). The process eventually worked out for very successful lithography (the two-step or double litho) made these type of films obsolete regardless, as it was deemed preferable to have no metal below the permalloy for the experiments (to avoid interface effects, for instance, spin injection).

5.2.2D IBM electroplated film

Some films were not made by ourselves but ordered directly from IBM. These were high quality, electroplated, 2 μm thick permalloy films which had excellent hysteretic properties as will be discussed in section 6.4.2 and would even be appropriate for conduction to be single step lithography films. The only problem with these is they were too thick for our purposes: first, as we try to move to thinner films to enter a regime where exchange interaction insures uniform response through the thickness, and second, wet chemical etch lithography, being isotropic, limits our resolution capabilities of so thick a film by introducing a 4 μm (2 x thickness) error. These films could still be valuable when using ion milling (because of inherent anisotropy of this etch) and as possible tall/thin structures if used in combination with a nano-lithography technique like e-beam or AFM lithography.

5.3 Patterning

5.3.1 Photolithography and Wet Chemical Etching

In general, photolithography and wet chemical etching techniques were successful for any features above 2 μm. The standard process was used where a photoresist is exposed in the desired pattern and developed to act as a shield against etching this pattern when the entire substrate is immersed in a chemical etch. We used a commercial photoresist HPR 504 which is a positive resist (areas exposed to UV light are removed in development), which we spun on at 4000 rpm (for 25s) and soft baked at 110 C for 1/2 hour. The speed of 4000 rpm should give a photoresist thickness of approximately 12 kA.

We tried spinning at faster speed, including 5000 rpm, and including in a containment drum (which allows less solvent evapouration) to make a thinner photoresist layer which would enable higher ultimate resolution (light has less distance to diffract in the thinner layer). This was successful with help from lithography experts at AMC, but was not a regular "known process" so was abandoned in preference to the lower spin speeds.

The softbake at 110 C removes the solvent in the photoresist but also removes all of the water from the resist. For this reason, softbaked substrates must be given at least 15 min to rehydrate before they are exposed or the resist will not develop properly (this was learned the hard way by the author!). A soft-baked resist has had all the solvent (that was needed to allow it to spin onto the substrate) removed and so lasts indefinitely after its bake. Care must be taken, however, that it is not unintentionally exposed to any UV light in this time period.

The UV exposure was done with a Karl Suss mask aligner (at AMC) which was designed for uniformity across several inches. The Quintel aligner (also at AMC) may have been more desirable for our work being more accurate in the center of alignment, but being less uniform across inches. The Quintel was a more specialized machine, though, so was rejected for the same reasons as the thinner resist process. Exposures on the Karl Suss were precalibrated and took only a few seconds of exposing. Developing was done using commercial developer 352 diluted 6:1 (from AMC - prediluted) and took on average around 30 s. Endpoint detection was by viewing the disappearance of photoresist "sludge" that would cling to the surface of the substrate. The sludge would appear immediately upon immersion. Again, many tricks are available to the fabricator for fine resolution (for instance, further diluting the developer), but few were attempted due to

time constraints.

Developing was followed by hard bake at 120 C for 1/2 hour. The temperature of hard bake has to be fairly precise to prevent "flowing" of the patterned resist. Hard bake completely dries the resist to strengthen it for wet etching. The effect only lasts for about four hours after completion of the bake, so this process must be undertaken just prior to the etching (multiple hard bakes shouldn't degrade the quality of the pattern).

Wet chemical etching was the pattern transfer process successfully used in many of the samples. Each metal had its own particular etchant so I will talk more about this process when discussing the individual metal fabrications below.

5.3.1A Gold

All coils and switches were fabricated using the above mentioned photolithography technique. In the case of some gold coils where ultimate resolution was not a concern, resist was spun thicker (at a lower speed) and soft bakes were done with a vacuum bake (with 10s N2 purge after) at 110 C for 50 s as opposed to the half hour usual bake. The gold etch was a commercial one obtained from AMC. Endpoint detection is similar to the developing of photoresist in that the etch visibly dissolves the gold; when the brown sludge is no longer visible near the surface of the substrate, the etching is finished (this usually took about 15 s for 1000 A of gold). Titanium etch could be made with 10:1 H_2O:HF which is almost instantaneous for less than 100 nm of Ti. This results in better quality etching then you might think, because, the liquid has no time to get under the pattern protection. Two micrometer lithography had not been readily achievable in the gold but, for the most part, it was not needed. Early switch fabrication had only the 6 μm

lines turn out (this is one reason why these switches became the standard), but later fabrication had most 2 μm features recognizable with around 50% yield.

5.3.1B Permalloy

The first microstructures fabricated (the coil with the 4 μm square inside) were actually of gold for a concurrent project[5.9]. Upon fabricating with permalloy, however (coil and structure made of permalloy), the coil proved to be too resistive to pass the necessary currents (of note, the films used in this process were the Perkin Elmer permalloy which had high resistivity, so one shot lithography may still be a viable option). The combination films made in UHV of Ti/Au/Py were used in order to keep a one-step process from which some success came (sample "previous"), however, it was undesirable to have a metal layer underneath the permalloy which could skew results.

Chemical etching of many of the first structures attempted was unsuccessful. A permalloy etchant taken from reference 5.1 (call it Py etch) consisted of 3.9M H_2SO_4, 1.12M H_2O_2, and 0.4M HF. This was made by using 21.8 ml of 98% H_2SO_4, 17.8 ml of 30% H_2O_2 and 1.9 ml of 49% HF (the HF was later found to be unnecessary except for the specific Ti beveling use cited in ref. 5.1). This etchant first proved to disintegrate the permalloy (Perkin Elmer films). The suspicion was that the HF was etching the glass underneath and causing the problem. The etchant was tried without HF but had no effect on the Perkin Elmer films. Similarly HNO_3 (a Ni etch[5.5]) would change its rate of etch (an oxidation layer was suspected for this) and Fe_3Cl (an iron etch[5.5]) only gave 10 μm resolution. The major error made in trying to characterize a reliable wet etch process was that all of these etchants were tried on the Perkin Elmer films which we would eventually

discredit. The original etch used (Py etch) did eventually work well for other films and was even found to work without the need of the HF. The rate was previously established as 4 µm/min and our etching seemed to substantiate this. This meant most of our films (at 1000 A or less) took only a second or two to etch. Of note, the gold etch was found to etch permalloy which also posed problems for any samples that had permalloy on top of gold. Before it was known that the Py etch would work, however, wet chemical etching was proving fruitless and so was temporarily abandoned in favour of ion milling as an etch process.

5.3.2. Ion Milling

Ion milling is done by simply allowing an inert ion gas (Ar) to bombard the sample. It introduces the advantages of an isotropic etch (bombarding ions are accelerated "straight down") so that undercutting of the material is almost non-existent giving better ultimate resolution than wet etch pattern transfer. Ion milling systems were used both in the lab and at AMC.

The only concern with ion milling is the condition of the photoresist on top after the milling is complete. Because of the energetic bombardment, the PR gets oxidized to turn into a "sooty mess" which would not dissolve in regular acetone. Various solvents were used (Microstrip, Trichloroethane, Toluene, Dichloromethane, benzene and combinations thereof, with ultrasonic) to try and take it off with little success. Using an oxygen plasma barrel etch at AMC did take off the PR but caused some concern over oxidation contamination in the permalloy because the film actually grew in height 200-400 A during the process (which might mean an oxide of up to 600 A on the surface).

Specifications of the oxygen plasma were 10 min at 400 mtorr O_2 with 300W rf power. One method that was used to overcome this problem was a cycling of the milling. The ion current would be "turned on" for five minutes and then off for five to ten minutes to allow the resist to cool. Sample "previous" was made with this technique.

Another method that would allow getting rid of the problem of PR would use (for example) aluminum as the ion milling mask (this method has not yet been tried). In the case of (positive) photolithography, an aluminum layer would be on top of the permalloy. This layer could be wet etched and then used as a milling mask. In the case of electron beam lithography, aluminum could be deposited on top of PMMA and lifted off to provide the milling mask.

5.3.3 Electron beam lithography (ebl) and lift-off technique

Because large numbers of samples were not needed in our case, we were able to make use of electron beam lithography which would allow higher resolution features to be fabricated. In this case, we would start with approximately 1x1 cm^2 substrates with gold coils on them (obtained by dicing). The standard process had 3% PMMA (made from 3 parts chlorobenzene and 2 parts 7.5 % PMMA) spread for 3s at 1000 rpm, ramped at 100, and spun for 25s at various speeds (2000 to 4000 rpm were tried). The hardbake was at 150C for 1 hr or 150C in a vacuum bake for 50s (with 10s N2 purge). Exposure happened with a focused electron beam in a commercial SEM ebl exposure system at AMC and developed with 1:3 MIBK:IPA for 1 minute, IPA for 20s, rinsed with water for 20s and dried. With the positive results of double photolithography and success beyond expectations with the measurements, an ebl process was not fully solidified in this work.

For this reason, and because ebl efforts are currently in full force by a colleague some descriptions of the particular instrumentation and techniques will be brief or omitted (refer to manuals at AMC regarding NPGS - nano-pattern generation system and the thesis by Li[5.10]).

The use of ebl allowed us to literally draw structures inside the coil. Figure 5.5 shows some photomicrographs of "wagon wheels"* patterned in PMMA (details of exposure (by K.W.Marsh) are omitted). There are nine wheels with different exposure doses in a grid (the gold coil and alignment marks appear in the background). The three wheels in the middle are not visible because this section has been overexposed by the field of view of the electron beam in SEM mode (the circle to the left is the "dump point" for the beam). Because of this, the place of exposure could not be viewed before exposing.

To overcome this problem, the alignment marks were used as origins for the ebl patterns. The result is shown in figures 5.6 where a set of six 2x1 μm particles was lined up to land one in the center of the coil and the tip of the second alignment arrow was used as an origin. The dump point (or resting place of the electron beam) is on the origin (a guiding arrow points to its location). Several problems had to be solved for this method to work. There was a magnification factor in the NPGS program that affected the scale of the electron beam and it had to be adjusted to insure that micrometers in computer patterns were also micrometers in the PMMA. Our particular SEM microscope also had a peculiar tilt angle to the beam (about 2.5°) that was apparent in NPGS mode but not in SEM mode which had to be manually corrected for to insure proper placement in the coil.

---

* This particular shape was chosen to specifically test the ebl process. The spoke widths could give away possible astigmatism in the beam and the general design should elucidate the proximity effect.

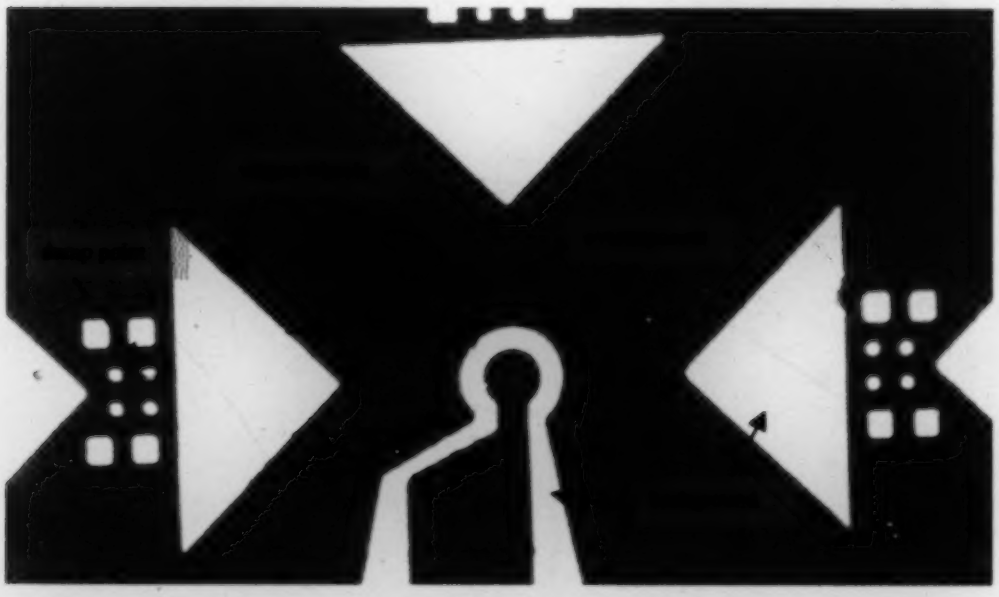

Fig 5.5 SEM image of electron beam lithography attempt in PMMA. In the background appears the coil with alignment marks. Visible is the field of view of the SEM in imaging mode which overexposed the center of the wagon wheel design.

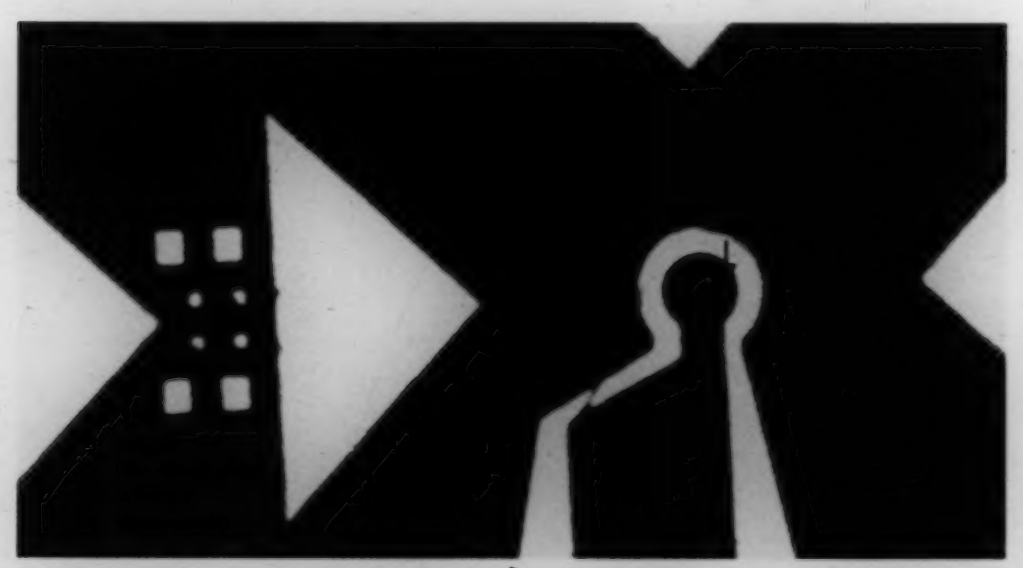

Fig 5.6 SEM image of ebl in PMMA. Six 2x1 μm particles are guided upon the center of the coil by using an alignment mark as origin. The large arrow points to the dump point at the origin.

Finally, grounding the gold and PMMA became a concern since, when SEM beam was moved off of the coil, the alignment marks charged up quickly and visibility was lost fairly soon unless very low filament settings were used.

Liftoff was successfully done with test aluminum and permalloy, by soaking the substrate upside-down in acetone for 30 seconds to a few minutes and sometimes using brief ultrasonic bursts to aid the lift of the film. The aluminum was evapourated which is the best technique to use with liftoff because the angle of deposition from the normal is smaller. Because a reliable sputtering process had already been worked out for permalloy, attempts at liftoff with permalloy were made with sputtered films, even though the flux angle of a sputtered film is much larger (in both cases, target size and sample-target distance is a major factor in angle). Surprisingly, these liftoffs worked! Figures 5.7 - 5.15 show SEM images of the first such sputtered permalloy liftoff results.

Figure 5.7 shows wagon wheels after exposing and developing (before deposition) of sample 1-6. The nine different wheels have different exposure doses and the dump point exposure and incoming beam line are clearly visible. Figure 5.8 - 5.11 and 5.12 - 5.15 show various views of samples 1-5 and 1-6 respectively after depositing permalloy and lifting off the PMMA. The first thing to note is that not all PMMA lifted off and not all of the desired metal stayed on. In figure 5.9 (magnification of fig 5.8) the black background is clean substrate, grey features are metallization (permalloy) and bright features are leftover PMMA. From this image, we see that the first four doses (three on top and middle row left) were too low for the pattern to develop right through the resist to the substrate. Only where the beam overlapped itself (at the center and corners) was exposure enough to make room for metal/substrate contact (this could be a promising

Fig 5.7 SEM micrograph of nine wagon wheel structures with different exposures in PMMA in electron beam lithography sample 1-6.

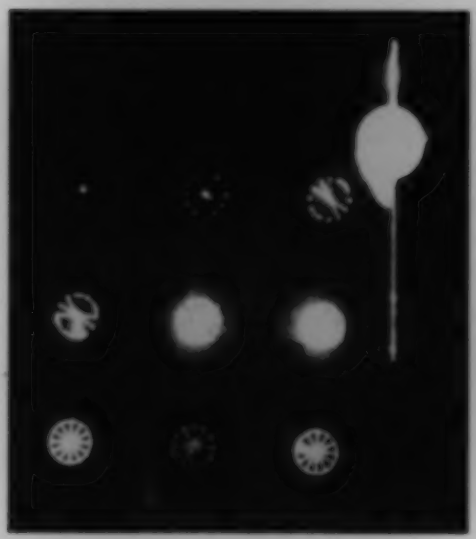

Fig 5.8 SEM image of wagon wheels after permalloy deposition and liftoff in sample 1-5.

Fig 5.9 Magnified image of figure 5.8. Dark areas are substrate, grey areas are metallization, and bright areas are leftover PMMA.

Fig 5.10 Wheel #8 showing proper liftoff. Some outlines are apparent on the spokes possibly indicating sidewalls.

technique for making small dots by overlapping two beam lines in a pattern). The 5th and 6th wheels (middle and right in middle row) have enough exposure to penetrate to the substrate, but the aspect ratio of the holes in the PMMA is still too high for our deposition parameters. I presume this because pieces of the PMMA are left; the supposition is that metal contacts the surface of the substrate but is also holding down the PMMA and/or preventing acetone dissolution from the sides. Wheels 7 and 8 (and almost 9) had good exposure doses for our conditions as the pattern transfer lifted off properly. Figure 5.10 shows a close-up of wheel 8. The center of the wheel is clean (proximity effect would have insured "open" deposition), but the spokes have some visible "outlines" which may indicate metal sidewalls or PMMA left. Wheel 6 is magnified in figure 5.11 showing how the gaps between PMMA pieces are very small.

Let us view figures 5.12 through 5.15 now. This sample should be identical to the sample identified in figures 5.8 through 5.11 (sample 1-5) because the PMMA spinning conditions, exposure dose template, and deposition run were all the same. The metal adhesion, and leftover PMMA, however, are slightly different. Now, the first six wheels are underexposed and all of the 7th, 8th, and 9th wheels have PMMA pieces left inside. This tells us our process was not repeatable and more work is needed for reproducibility. Figures 5.13, 5.14, and 5.15 show two of the wheels with wedges. 5.13 shows the best wheel (with just one wedge) corresponding to wheel number 7 or 8 in sample 1-5. Figure 5.15 is an angle shot of figure 5.14 (wheel #9). In this case, we see wider gaps between the wedges then figure 5.11 and, as indicated from 5.15, metallization is visible up the side of the PMMA.

Liftoff was also done with features of interest for measurement. Figures 5.16 and

Fig 5.11 Wheel #6 (middle right). Gaps between the PMMA pie pieces are small.

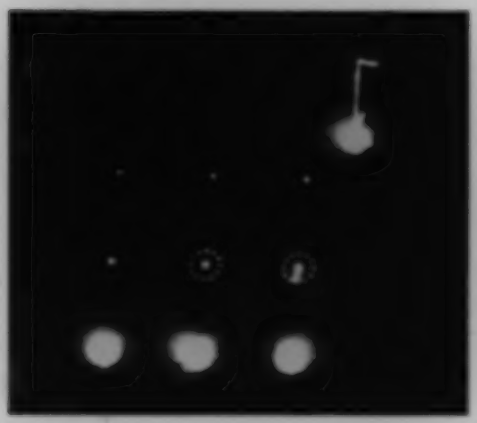

Fig 5.12 Sample 6-1 after deposition and liftoff. Wheels #1 through 6 are underexposed and wheels #7, 8, and 9 are full of PMMA.

Fig 5.13 "Best wheel" of sample 1-6 corresponding with wheel #7 or 8 in 1-5.

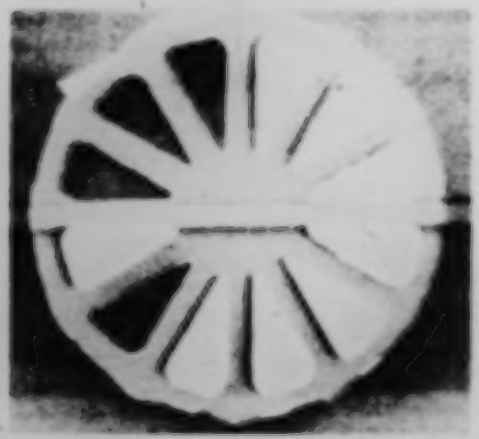

Fig 5.14 Wheel #9 in sample 1-6. Several PMMA pieces remain held to the substrate. The gaps are wider here than in figure 5.11.

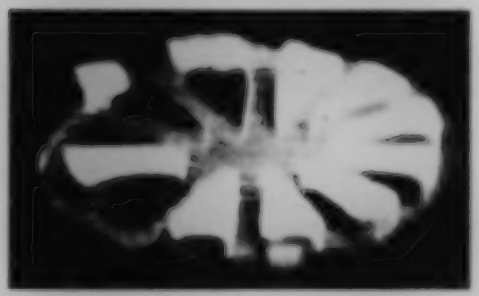

Fig 5.15 Angle shot showing metalization up the sides of the PMMA.

5.17 show angle views of a 2x1 μm permalloy particle after liftoff. The surface of the particle isn't entirely smooth but there are definitely no sidewalls visible. Either there never were sidewalls, or they've fallen off and are far from the particle, either of which leaves a situation acceptable for measurement.

The combinations of successful liftoff and pattern transfer with lack of repeatability tells us that the sputtered permalloy liftoff/ebl technique needs more characterization to be reliable. What is known is that the permalloy films must have good adhesion to the substrate to stay on and even hold sidewalls and PMMA on when the rest of the film lifts. Still, some effort is needed to insure the sidewalls can be eliminated or, at least, removed and that ebl exposure dose can be properly calibrated in order to have a clean process. The latter of these concerns has since been addressed by a colleague. One process that may work would combine liftoff with ion milling. The permalloy layer would be deposited underneath the PMMA and an aluminum layer would be used in liftoff to form an aluminum feature inside a coil (with permalloy film underneath). This would also solve the problem of PMMA charging in the electron beam. This whole structure could then be ion-milled using the aluminum as a mask (as referred to in section 5.3.2) to give clean, straight walls to the final permalloy microstructure and maintain the benefits of ebl resolution.

5.3.4 Double Lithography Technique

The technique that proved most effective in pattern transfer was doing two sets of photolithography on the same substrate. A gold film was deposited and gold coils transferred into it through photolithography and wet etching. A permalloy film was then

Fig 5.16 SEM micrograph (angle view) of a successful 2x1 μm permailoy liftoff particle. The surface isn't entirely smooth but there are no sidewalls.

Fig 5.17 Another 2x1 μm liftoff particle. This one has higher topography in the top left corner.

put on top of these gold coils and the microstructure transferred inside a coil by a second photolithography and etching step. This is what the mask was originally designed to do (as referred to in section 4.2). Before the process was taken on seriously, it was delayed as a last resort because of the complexity of the transfer. First, it was believed that a large substrate was needed to satisfy conditions of photoresist spinning because any substrate without a beveled edge will build up PR not allowing firm contact with the mask near the edge (aggravating diffraction effects). Second, because of the mask design, only one microstructure per exposure is possible and care must be taken to keep other areas of the substrate unexposed. These reasons, combined with the need for two lithography and two etching steps made this process seem undesirable.

The problem of PR buildup on the edge turned out to not affect the resolution noticeably if far enough from an edge, even for small substrates and even for features only 1 mm from the edge. This alleviated the second problem by allowing exposure of small substrates with single structures on them. Coils were diced into pieces approximately 1x1 cm^2 (as with the ebl samples) before permalloy deposition. This allowed more precise placement of the substrate in the most favourable in-plane field during deposition (for the sputter holder discussed in 5.2.2C). Any single feature could then be transferred to the center of the coil with photolithography and wet etching. Sometimes, the second photolithography step introduced structures that partially covered the coil. These could be simply removed by using a small gob of half dry PR on top of the freshly etched feature and dipping in the etch again.

Several samples were fabricated this way including the prize sample 3.6.8. Refer again to the appendix for the types of microstructure features that are available for this

double lithography process.

5.4 Fabrication Summary

Several metal deposition techniques were shown and a reliable and repeatable deposition technique for each metal (permalloy, chromium, gold, titanium) was demonstrated. In particular, some discussion regarding the UHV sputtering of permalloy was given in detail allowing for future UHV sputtering experimentation.

A "double lithography" photolithography and wet chemical etching technique gave a reliable and straightforward process for the fabrication of desired permalloy microstructures. The merits and drawbacks of ion-milling were discussed, a successful process was demonstrated, and further use and adaptation of the ion-milling process was suggested. Electron beam lithography was investigated and a technique worked out. Evapourated aluminum and sputtered permalloy films were successfully lifted off, problems with the technique were identified, and an effective solution suggested, making ebl a very promising and readily designed possibility for sub-2 μm lithography.

In summary, techniques were shown for the successful (reliable and repeatable) simultaneous transference of a conducting coil and permalloy microstructure onto a non-conducting substrate to fulfill the needs of the measurement process of this work.

6 CHARACTERIZATION

6.1 Introduction

Early into experimentation, especially with the problems caused by the first sputtered permalloy at AMC, it became clear that it was imperative to know what the properties of the thin films were. Characterizations were done on the content (%Ni/%Fe) and resistivity, static magnetic imaging was done with magnetic force microscopy (MFM), and hysteresis loops were taken by SQUID magnetometery and magneto-optic Kerr effect (MOKE) detection.

6.2 SEM Thin Film Stoichiometry

In any technique for the deposition of an alloy, the percentage makeup of the alloyed target or evapouration melt does not necessarily reflect the final stoichiometry of the thin film. For instance, the nature of sputtering being closely tied with cohesive energies and atomic-scale kinematics means different atoms will sputter at different rates. Quickly after a target is first used, one element becomes depleted enough that a steady state is reached where thin films will always have the same composition thereafter (though it need not, and probably won't, be the same as the nominal composition). In this work, using a scanning electron microprobe on the final film to detect the x-ray emission lines of elements, allows the assignment of percentage of nickel and iron in the film. Table 6.1 summarizes the results for two films of the permalloy sputtered in UHV (all percentages are given as weight percent). The first determination was done after only a few depositions so the target may not have reached equilibrium. The second film was

Table 6.1 Composition of two UHV sputtered permalloy films. Film 2 should reflect current and future film compositions. All percentages are weight percent.

	%Ni	% Fe
Film 1	83.8	16.2
Film 2	84.2	15.8
Nominal Sputter Target	81.0	19.0

produced after the sample 3.6.8 with similar deposition conditions (only base pressure would be different) and should reflect all future runs of the particular sputtering target as well as the composition of 3.6.8. The composition is not as close to 81/19 permalloy as we would like but is still acceptable*.

6.3 Magnetic Force Microscopy (MFM)

Magnetic Force Microscopy has been a very successful tool for static domain imaging. In our case, it was useful for qualitative comparison to domains imaged with SKEM, as well as for confirmation that films were magnetic and for checking patterning techniques such as liftoff.

Figure 6.2 shows an AFM/MFM image of one of the UHV sputtered multi-layer films ("previous"). The image on the left is topography of the structure with light areas being higher. On the right is the magnetic information of this same topography. These images were taken with a DI Nanoscope III in "lift" mode[6.1] (see fig 6.1). The AFM cantilever tip scans one line in contact with the surface to measure the topography through piezofeedback ("classic" SPM). The magnetized tip is then lifted and immediately scanned over the same line in "tapping" mode (the tip can be modeled as a damped harmonic oscillator) remembering the topography and maintaining a constant height over the surface (fig 6.1). Because of the magnetization of the tip, the magnetic flux near the surface of the substrate changes the force on the cantilever, and so can be picked up as a change of resonant frequency (or, because it is easier to detect instrumentally, as a phase shift in the

* The measurements were precise to at least 0.1% (ie. repeatable) but there was some concern over accuracy of the particular x-ray analysis instrument used. Systematic error as high as 10% has been suggested.

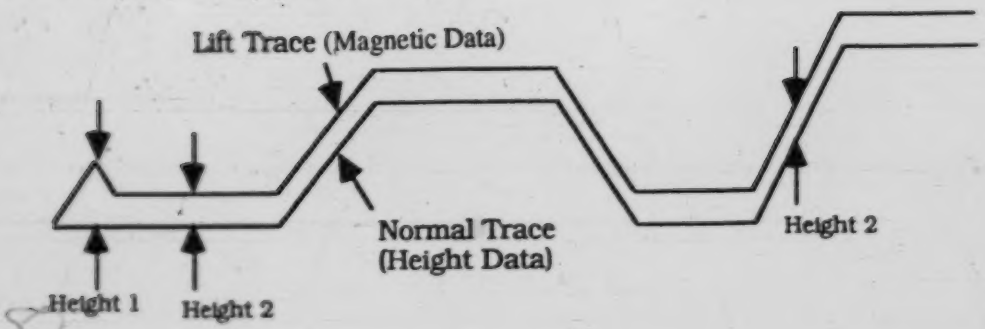

Fig 6.1 Lift mode of a magnetic force microscope (MFM). The original trace determines topographic data, while the lifted trace determines magnetic data by maintaining a constant height[6.1].

resonant frequency). The component of magnetization that actually exerts the force is often modeled as the second derivative in the perpendicular direction of the magnetic field, though this is only an approximation and thorough analysis of the interaction between the tip and the surface is currently an open topic of research[6.2]. In this sense, it is hard to quantify magnetic images to determine the precise magnetization structure of the film. We must be satisfied with the contrast revealing qualitative domain structure.

As can be seen, this ion-mill transferred pattern was not particularly clean; it should be noted that scanning was from right to left in these images and "tails" seen to the left of structures are scanning artifacts. Figure 6.3 reveals definitive magnetic information. The outer coil shows magnetic contrast mostly where there is topographic contrast, but elsewhere as well. The particle in the center shows domain structure as if cut into a 6 piece pie. Figures 6.4 and 6.5 are close-ups of this particle showing a topographic "dot" near the center that may have caused the domain structure; in 6.5 there is also a flux leak across the middle of the particle apparently reflecting some of the subtle topography.

Figures 6.6 through 6.11 show MFM scans of some of the ebl/liftoff wagon wheel structures (cf. section 5.3.3). The left image of figure 6.6 shows that extra exposure of the PMMA may lead to a thicker film in deposition as the center and intersecting edges of the wheel show higher topography. This topography is reflected in the magnetic image on the right; visible in the center hub of the wheel is what might be a bright flux stream exiting on its right and a darker line reentering on its left but may also be an artifact. One of the major concerns in force microscopies is interpretation of data. The wave-like background is again just a scanning artifact (e.g. electrical feedback loop pick-up which would be scan rate dependent).

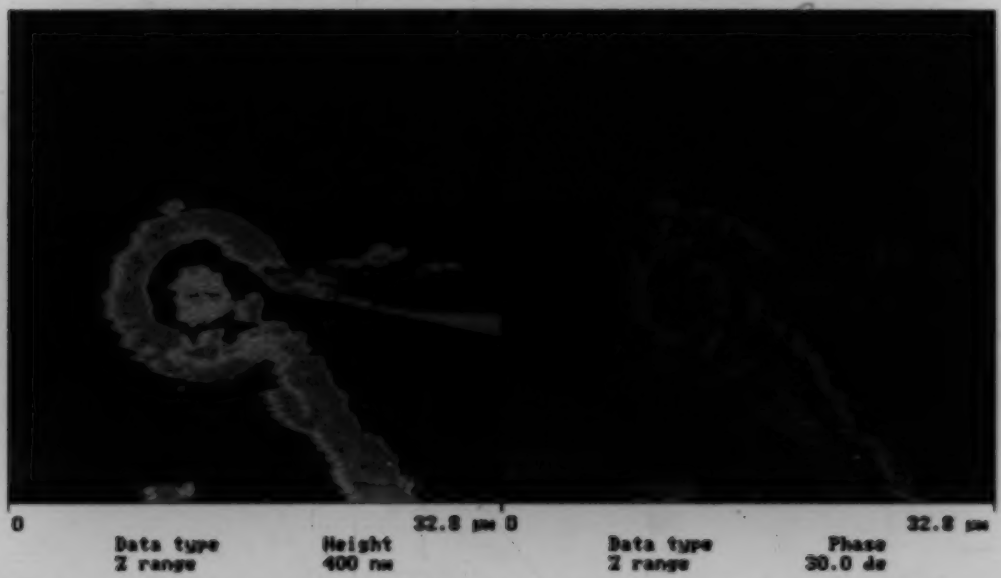

Fig 6.2 A magnetic force microscope (MFM) image of sample "previous". The figure on the left is topography. On the right is magnetic information.

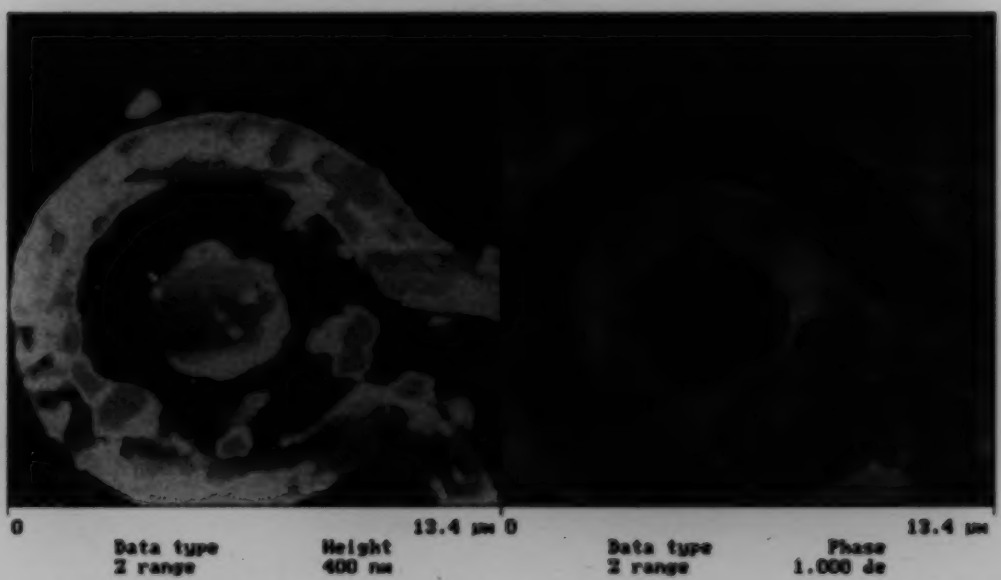

Fig 6.3 MFM image of sample previous. Magnetic contrast in the right image reflects topography. A six-piece pie domain structure is visible in the center structure.

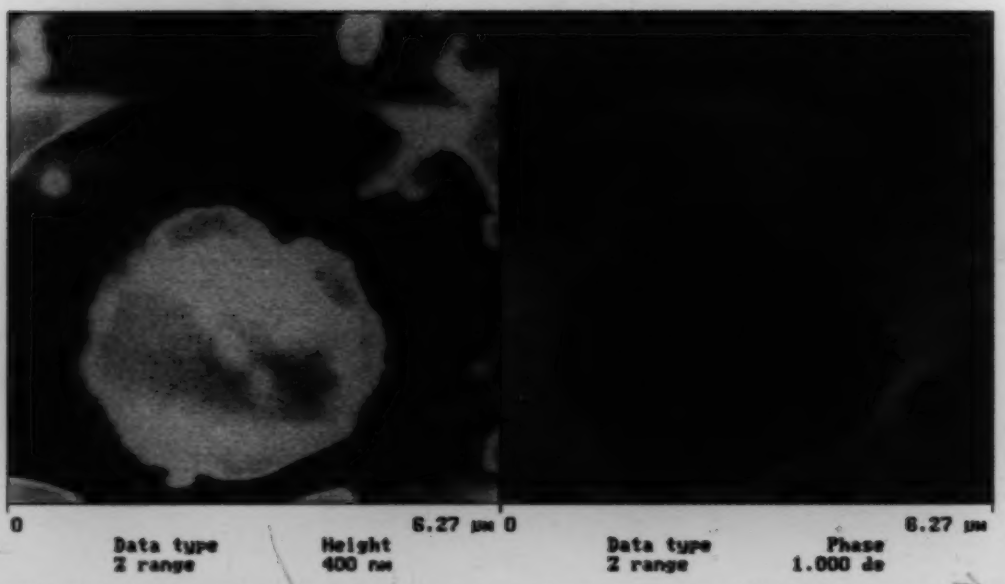

Fig 6.4 MFM image of the microstructure in sample "previous". The topographic defect in the center of the circle may have caused the domain structure.

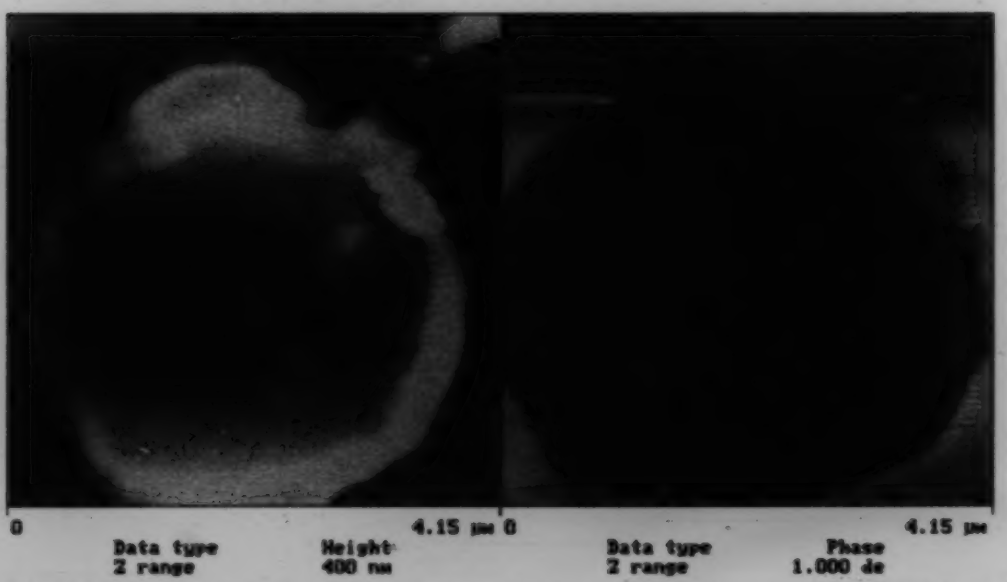

Fig 6.5 MFM image of microstructure in sample "previous". A flux leak exists across the middle of the structure.

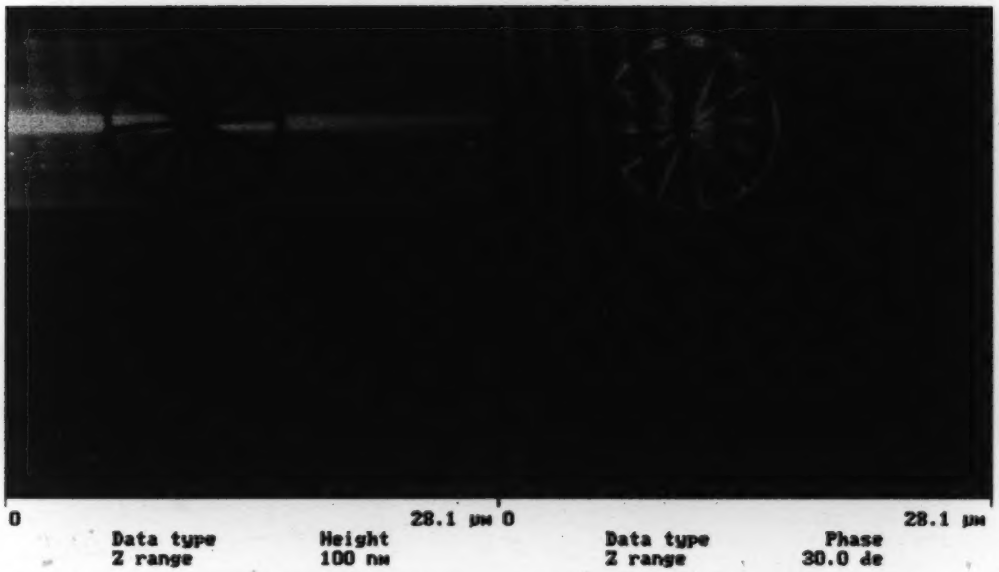

Fig 6.6 MFM images of ebl/liftoff permalloy wagon wheels. Topographic magnetic information is reflected on the right. Bright and dark sections of the hub may signal flux lines or a scanning artifact.

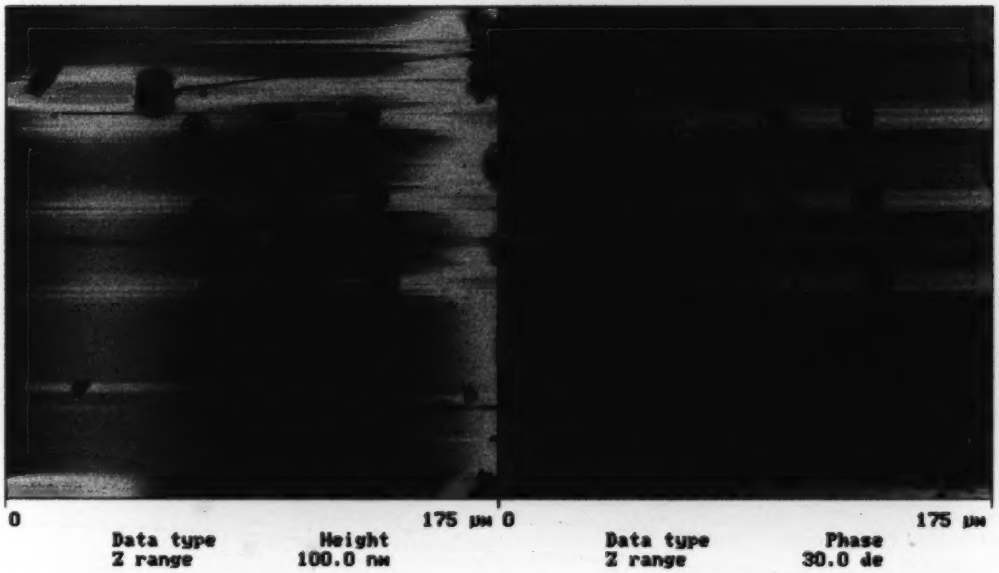

Fig 6.7 MFM image of liftoff wagon wheels. Domains in the lettering to the far right and in the wheel hubs give indication of critical size for this permalloy film.

Figures 6.7 and 6.8 confirm the wheel pieces are tending towards two or three domain splitting (look at the wheel hubs for example) and start to give us a feel for the size a particle will need to be to satisfy single domain regime (each full wheel is 10 μm diameter). Also visible on the right of 6.7, some lettering reveals domain structure and critical size. Close-up images of the top right wheel in figures 6.9 and 6.10 show that many of the spokes may even be single domain (as evidenced in magnification in fig 6.11). The hub in these figures is notably absent of magnetic information. This probably does not indicate the material there is non-magnetic though it may be completely demagnetized for some reason. It may instead be telling us that the center portion of the particle has its magnetization lying squarely in the plane of the substrate and flux is being channeled through the spokes at either end. In figure 6.10, we do see a subtle bright highlight on the right and dark on the left. This also gives us a feeling for how big the particle needs to be to make demagnetizing at the edges only negligible. If we go back to figure 7, we see various sized hubs for different exposures; as the hubs become smaller, the demagnetizing effect (darker areas) becomes more noticeable.

Figures 6.12 and 6.13 take us back to the ion-milled sample "previous" again. This time we look at some of the alignment marks to see if we can identify any square domain structure. In fact, all four squares visible in 6.12 exhibit reasonable domains. Three of them are split into four triangular closure domains while the fourth forms closure by sticking in an extra domain around the defect. Figure 12 is a close-up of the upper corner of one of the larger squares showing the domain there actually splits to accommodate the rounded corner (see, for instance, Ding and Zhu[6.3]).

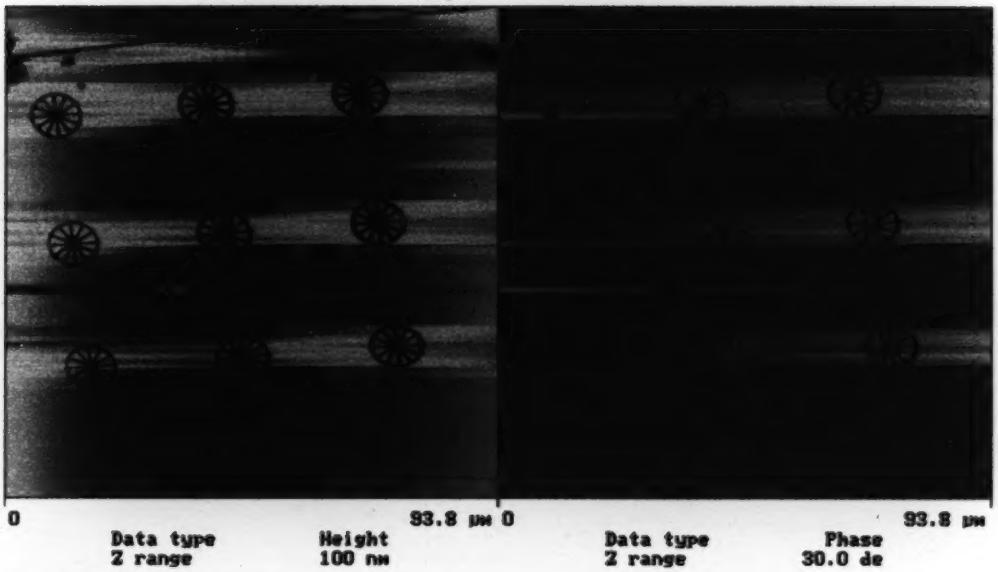

Fig 6.8 MFM image of liftoff wagon wheel. The magnetic response of the wheel hubs changes as the size of the hubs grows qualitatively revealing critical size and demagnetizing effect.

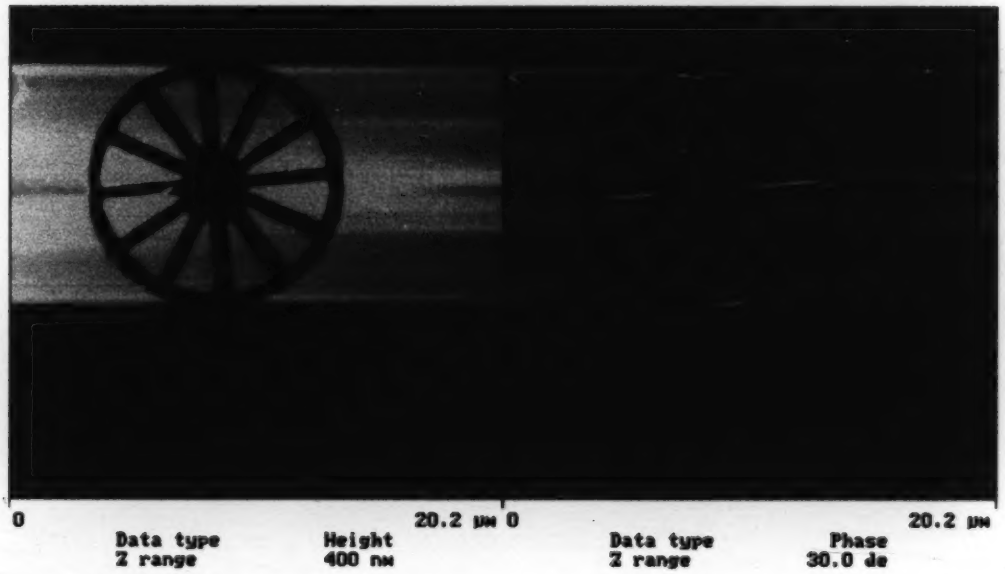

Fig 6.9 MFM image of wagon wheel. The spokes seem to be single domain and the hub is absent of magnetic information.

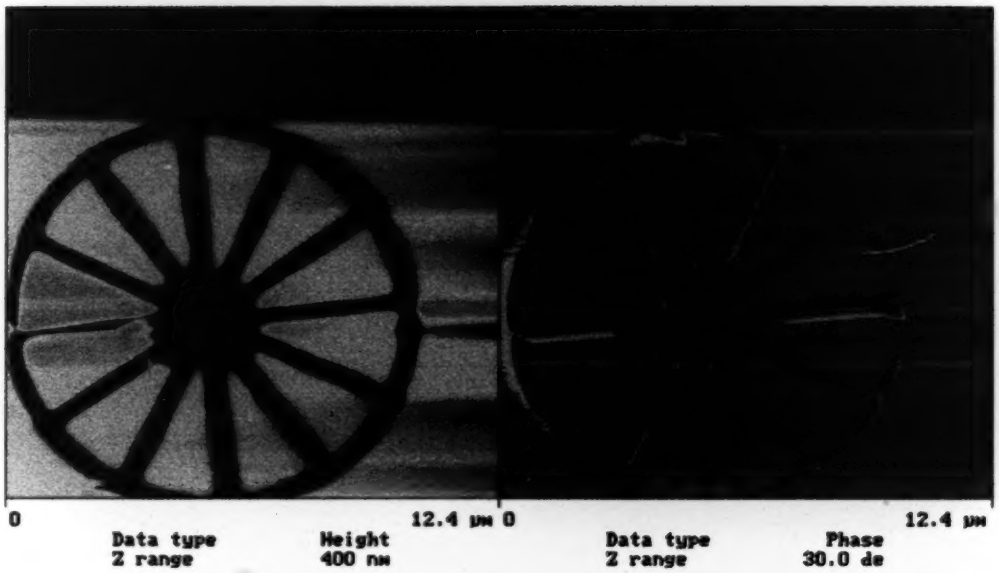

Fig 6.10 MFM image of wagon wheel. There is a possible dark highlight on the left of the hub which may indicate flux or artifact.

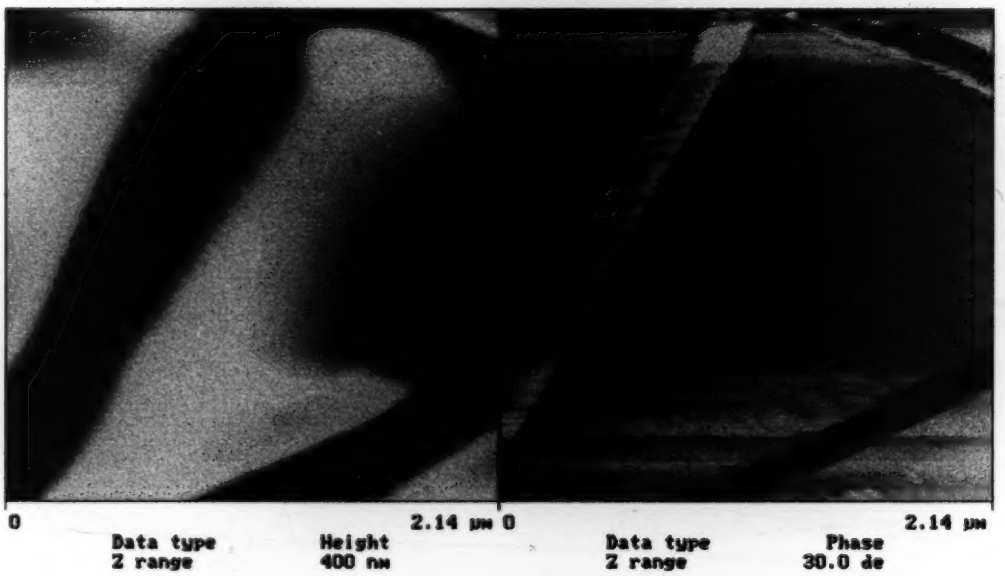

Fig 6.11 MFM image of spokes in a wagon wheel. Spokes are single domain.

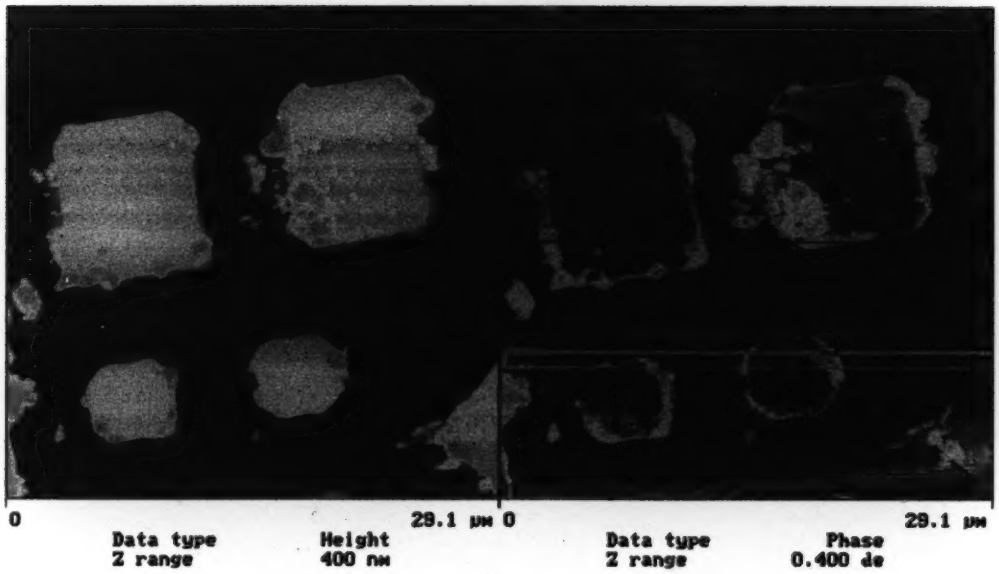

Fig 6.12 MFM image of some alignment marks on sample "previous". Classic closure domains are evident in these square microstructures.

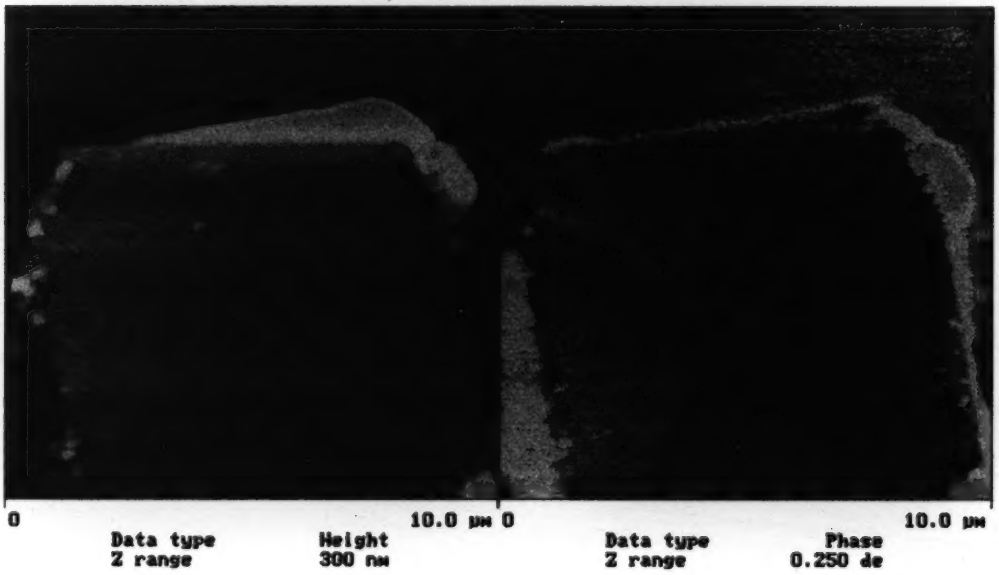

Fig 6.13 MFM image on "previous". The four-domain closure structure splits to accommodate rounded corners.

Hysteresis Measurements:

Further static magnetic measurements were done to ascertain the properties of the NiFe, specifically the hysteretic properties. These were accomplished both with homemade laser MOKE detection and with the more standard process of SQUID Magnetometery.

6.4.1 SQUID magnetometery:

As a check on the MOKE hysteresis measurements, hysteresis loops were recorded in a SQUID magnetometer. The MOKE measurements were giving sometimes erratic results and confirmation was needed. Figures 6.14 and 6.15 summarize these results. The first figure shows the hystereses for both the assumed easy and hard axes ((a) and (b)) of the lower quality permalloy referred to in section 5.2.2B. These measurements convincingly confirm the suspicion that the films were very low quality. The first thing to note, is that the easy and hard axes hystereses look very similar. This would mean that there was no easy axis induced in this particular sample. Secondly, the magnetization does not saturate, even at 1000 Oe. In fact, past about 400 Oe there seems to be linear slope (the signature of a paramagnetic background). It is possible that the magnetometer was contaminated with a paramagnetic material, though it is very unlikely to be so contaminated as to give signal in the 10^{-4} emu range. More likely, what we see as a paramagnetic background is the sample itself, indicating the permalloy might be very oxygen contaminated and comprised partly of paramagnetic oxide. Furthermore, resistance measurements on a patterned sample indicate resistivity of the order of 400 μΩ-cm (we would expect around 20 μΩ-cm). There is still visible some hysteretic behaviour

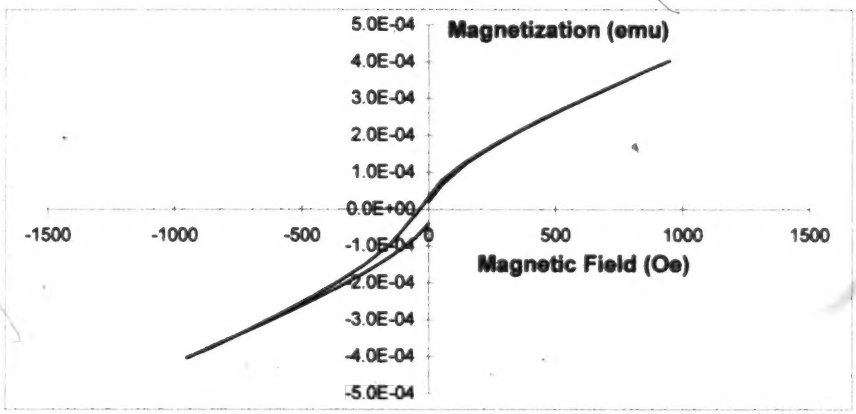

Fig 6.14(a) Hysteresis loop of Perkin Elmer sputtered permalloy. The material is apparently a mixture of paramagnetic and hard ferromagnetic (linear slope and low remanence respectively).

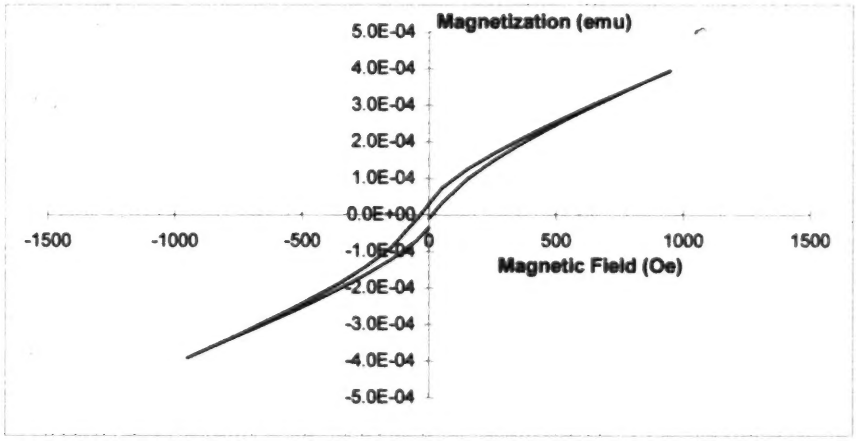

Fig 6.14(b) Hysteresis loop of Perkin Elmer sputtered permalloy at 90° indicating no uniaxial anisotropy was induced.

between -400 and +400 Oe indicating that the film also contains some ferromagnetic material. Nevertheless, this measurement confirmed that a new deposition technique was needed.

Alternately, figure 6.15 shows much more desirable magnetic behaviour from a sample of UHV sputtered permalloy. The film diagnosed in this case was the same one used for SEM stoichiometric determinations; it was a result of a deposition under identical conditions to the deposition resulting in sample 3.6.8. Figure 14(a) shows the easy axis of the film. The fact that it is offset from 0 Oe is due to a remanent field in the superconducting coils inside the SQUID and has nothing to do with the magnetic properties of the sample. The hysteresis loop is quite square as we would expect for 81/19 permalloy with a low value of coercivity of 0.9 Oe. This square loop also confirms that the technique to induce an easy axis by in-situ in-plane field is successful. Saturation for this particular sample is about $2x10^{-3}$ emu. The sample was approximately 5mm x 5mm and 1000 A thick giving a volume of $2.5x10^{-6}$ cm^3. Thus the saturation magnetization (M=emu/V(in cm^3)) is 0.8 kG (so $4\pi M_s$ ~ 10 kG) agreeing well with the indications for 3.6.8 of 10.8 kG found in the chapter on results.

The hard axis viewed in fig (b) also corroborates our expectations of having a very small hysteresis, and quick to saturation (saturation indicates a value for H_k between 4 and 4.5 Oe. Because of the uncertainty in precise easy axis direction (substrates are aligned by eye in the deposition system), in addition to the alignment by eye of the sample in the magnetometer, the axes measurement may have been off by a few degrees (perhaps as much as 5°) as is indicated by this hard axis measurement showing a tiny amount of easy switch near the origin.

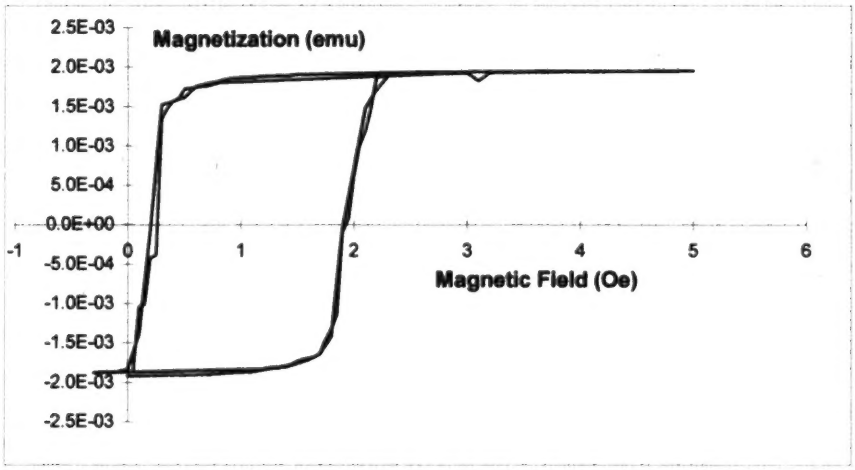

Fig 6.15(a) Easy-axis hysteresis loop of UHV sputtered permalloy indicating coercivity of 0.9 Oe and saturation magnetization of 800 G ($4\pi M_s$=10kG).

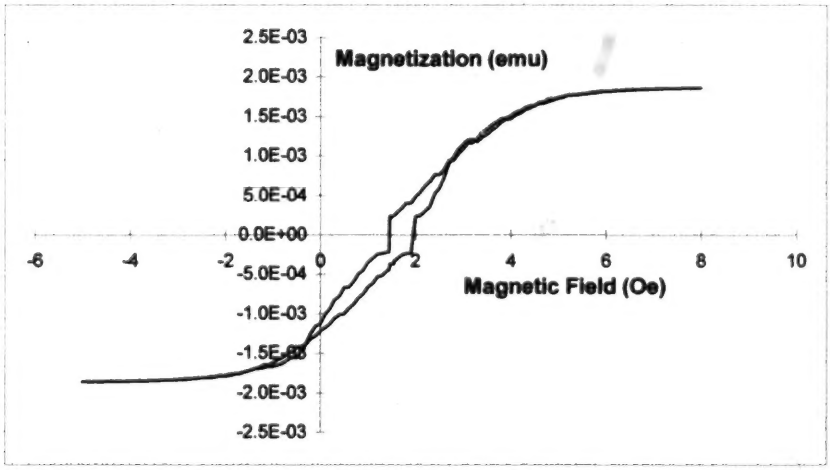

Fig 6.15(b) Hard-axis hysteresis loop of UHVsputtered permalloy indicating anisotropy field of 4 to 4.5 Oe. The loop is well closed with some easy switch visible near the center.

6.4.2 Optical measurements: static longitudinal MOKE

The magneto-optic Kerr effect (MOKE) was described in chapter 2 and generalized set-ups for the technique were given in figures 2.3-2.9. Hysteresis measurements were not only made to characterize the sample, but also to work out possible problems for the experimental time-resolved scanning Kerr system. Problems with consistency of hysteresis measurement and success of the scanning Kerr system on its own eventually led to the abandonment of the optical hysteresis measurements and the use of the SQUID for hystereses.

The major danger in the Kerr detection scheme is drift of the dc signal. Because the detection is of a very small rotation in polarization (down to the order of microradians) any movement of any component in the beam path is likely to be fatal to the reproducibility of the system. Measurements taken with the set-up were characterized by both abrupt changes in signal and slow floating. It would not be until setting up the time-resolved system that a minimum level of constant stability was accomplished, though stability remains a problem in the very delicate system. Further discussion regarding the experimental set-up will be given in chapter 7 where polar Kerr detection will be shown to give reliable and repeatable results and proposals for the longitudinal detection system will be given.

Figures 6.16 through 6.18 show several hysteresis loops for the first three samples of electron beam evapourated permalloy films. The y axis is the Kerr signal in arbitrary units and the x axis is external field in Oersted. The easy and hard axis for the first film show excellent characteristics. The easy axis defines a very square loop with H_c = 1.5 Oe,

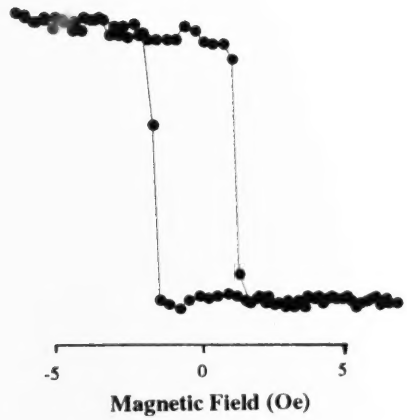

Fig 6.16(a) Easy loop of first electron beam deposited film using optical hysteresis measurements. H_c = 1.5 Oe.

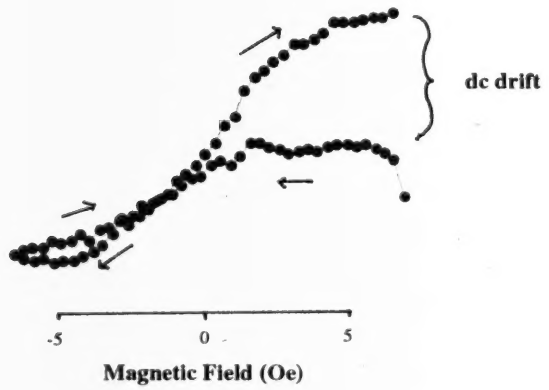

Fig 6.16(b) Hard axis loop of first e-beam deposited film. The loop is well closed (accounting for the dc level drift on the 0 to 5 Oe leg) and saturates at 5 Oe.

while the hard axis goes quickly to saturation (by 5 Oe) and is almost completely closed. Figure 6.16(b) also demonstrates some of the problems with the measurement system. The scan followed a reasonable curve until crossing O G field on its final leg when the saturation level changed (characteristic of floating).

Film # 2 was not as good quality as the first film, though none of the deposition parameters had been changed. Figure 6.17 shows a series of easy axis scans taken in a row of film #2. The loop is not as fully square and the coercivity is also higher at 5 Oe. Figure 6.17(b) also typifies the problems with the scanning system, giving a very poor trace and showing no visible hysteresis, though nothing was changed between this scan and the ones before and after.

Film # 3 (fig 6.18) was the first film deposited from the induction melted pellet (as opposed to powder) and the deposition rate was slower (0.6 A/s). The coercivity given by this easy axis is apparently very low but also hard to identify because the saturation seems much lower this time. As mentioned, one of the recurring problems with the measurements was inconsistency; in this case we could not be sure if the film properties were different or the scanning system had changed. Specifically, in the case of the initial sputtered films (non-UHV) where the surface was more paramagnetic, we were not able to identify this fact immediately with this system.

The 2 μm permalloy films from IBM were also measured. These were certainly the films of highest quality (as one might expect from the electroplating). Resistivity was also very good (~10-15 μΩ-cm). Figure 6.19 shows the easy axis loop which is extremely square with a very low coercivity of 0.18 Oe. The gaussmeter used to monitor the external magnetic field was even able to pick up the switch from the film because of

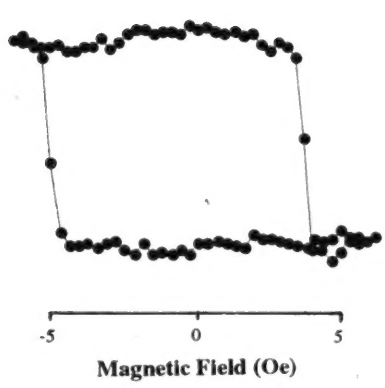

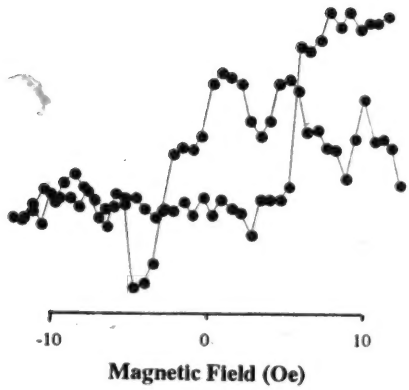

Fig 6.17(a) Easy loop of second e-beam deposited film. H_c = 5 Oe. **(b)** Easy loop taken on the same film with the same parameters demonstrating problems with the measurement system.

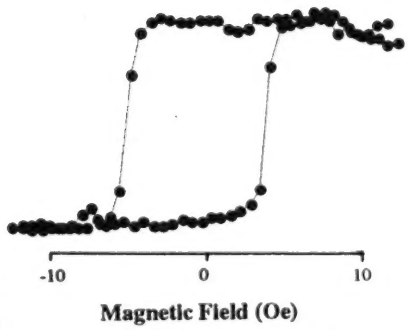

Fig 6.17(c) Easy loop again from a scan moments later.

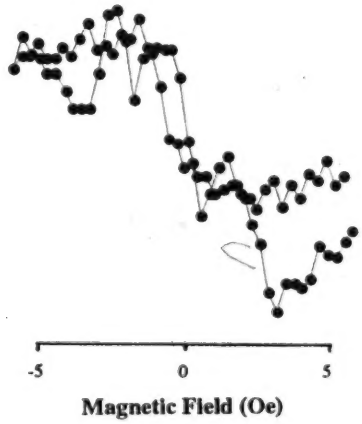

Fig 6.18 Easy loop of third e-beam deposited film. There may be a hysteresis in the center indicating H_c < 1 Oe though it is not definitive.

permalloy's high saturation magnetization.

Two of the UHV sputtered films were tested for hysteresis using the Kerr effect. Some examples of the result for film 1.2.1 are shown in figure 6.20. The film generally exhibited a square but not fully square easy loop with coercivity of 15 to 20 Oe. In trying to evaluate the success of the magnetic assembly (referred to in section 5.2.2C), which would've introduced different biasing field conditions for different areas of the substrate during deposition, measurements were taken at several points across the sample. Unfortunately, the unreliability of the system prevented a detailed analysis or even qualitative discussion. Sample 1.3.1, however, did support the merits of the magnetic assembly giving nice easy loop with 2 to 2.5 Oe coercivity (fig 6.21). Finally, sample "previous" was focused onto with a microscope objective (adding new problems which will be discussed in chapter 7) to show an easy axis hysteresis loop with 3.5 Oe coercivity (fig 6.22).

What we can conclude from these film characterizations is that the IBM electroplated films are the best quality. These, however, have the problem of not being of use with small feature wet chemical etching or with simple liftoff technique. The UHV sputtered films, also, have become reliable and reproducible and show characteristics suitable for our purposes. Of note, resistivity measurements on various UHV sputtered films did confirm their quality with values below 20 $\mu\Omega$-cm.

SEM stoichiometric determinations, MFM microscopy, and optical and SQUID magnetometer hysteresis measurements have confirmed the characteristics of our permalloy films. The UHV films have been shown to be suitable for fabrication and time-resolved measurements. An optical hysteresis measurement system, using the longitudinal

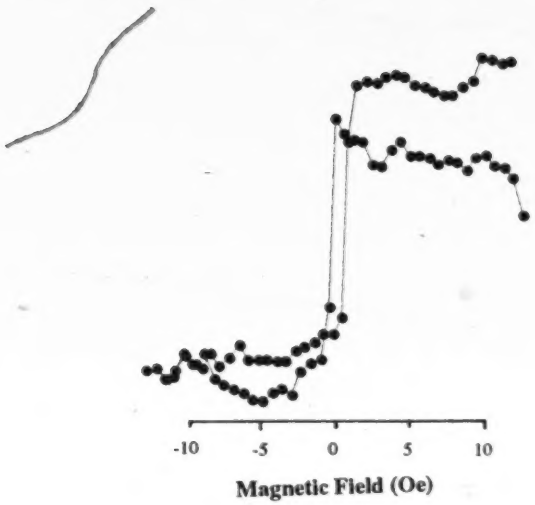

Fig 6.19 IBM electrodeposited permalloy film. H_c ~ 0.18 Oe.

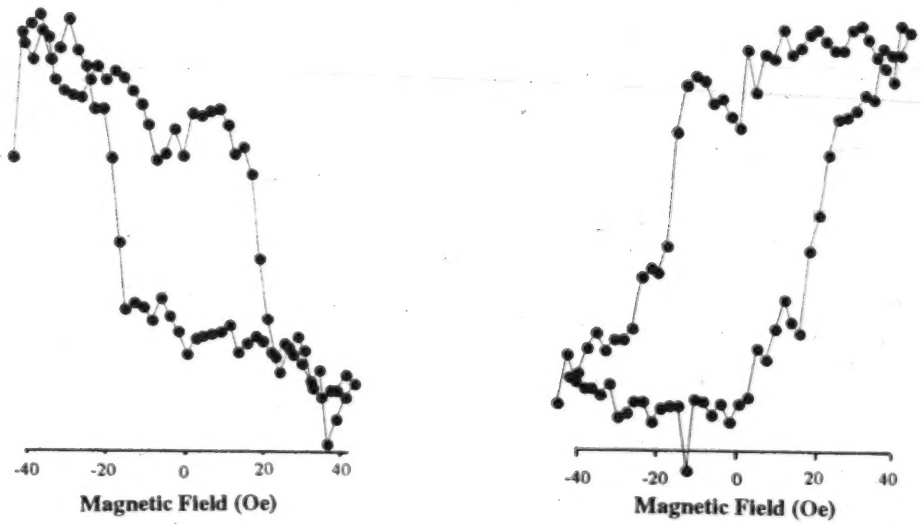

Fig 6.20(a),(b) Early UHV sputtered film (1.2.1) using the magnet assembly during deposition. H_c ~ 15 to 20 Oe.

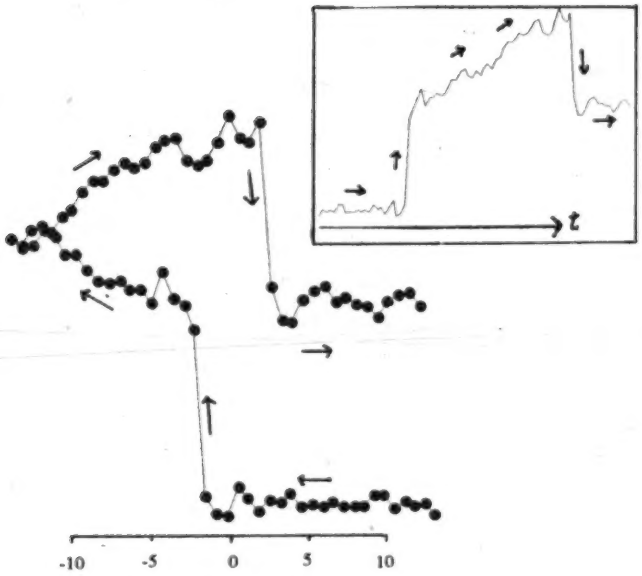

Fig 6.21 UHV sputtered film (1.3.1) using the magnet assembly. H_c ~ 2 to 2.5 Oe. This loop again demonstrates dc drift with (inset) signal vs time. In this case, the drift is as large as the hysteretic switch!

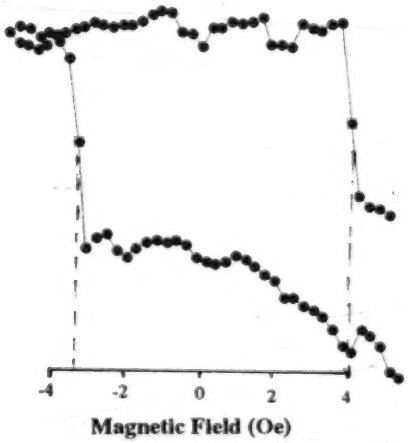

Fig 6.22 Easy loop of sample "previous" giving H_c = 3.5 Oe.

magneto-optic Kerr effect, was briefly discussed, shortcomings were pointed out, and some preliminary results were given. Repeatable success with and suggestions for improvement of a longitudinal Kerr experimental set-up will be discussed in the next chapter.

7 EXPERIMENTAL SET-UP: TIME RESOLVED SCANNING KERR EFFECT MICROSCOPY (TR-SKEM)

7.1 Introduction

The magneto-optic Kerr effect was discussed in chapter 2 and several diagrams were given for the generic set-up such detection would need (for both longitudinal and polar Kerr microscopy). Because of its optical implementation, MOKE allows for time-resolution by using a pulsed laser in the pump-probe experimental technique. This chapter deals with the experimental setup of the time-resolved scanning Kerr technique.

7.2 Polar TR-SKEM

The detection scheme that was successfully used for the FMR measurements discussed in chapter 8 is specifically polar SKEM detection and is demonstrated in figures 7.1 through 7.3. Details of this experimental technique have been presented[7.1]. The output of a mode-locked dye laser (tuned to 591 nm, cavity dumped at 4 MHz with an energy of 25 nJ per 2 ps pulse or about 100 mW average power) is split into a pump beam (90%) and a probe beam (10%). The pump beam is focused onto a biased GaAs photoconductive switch sending a current pulse around a lithographic gold coil, creating a transient magnetic field H_i at the center of the coil, perpendicular to the plane of the substrate (fig 7.2 and inset). The probe beam undergoes a variable optical delay and is focused onto the permalloy structure at the center of the gold coil with an 80x (0.75 N.A.) microscope objective, giving better than 0.7 μm spatial resolution. The photoconductive switch is ac biased at 40 V_{pp} and 4.234 kHz giving an RMS current of 0.3 mA. The

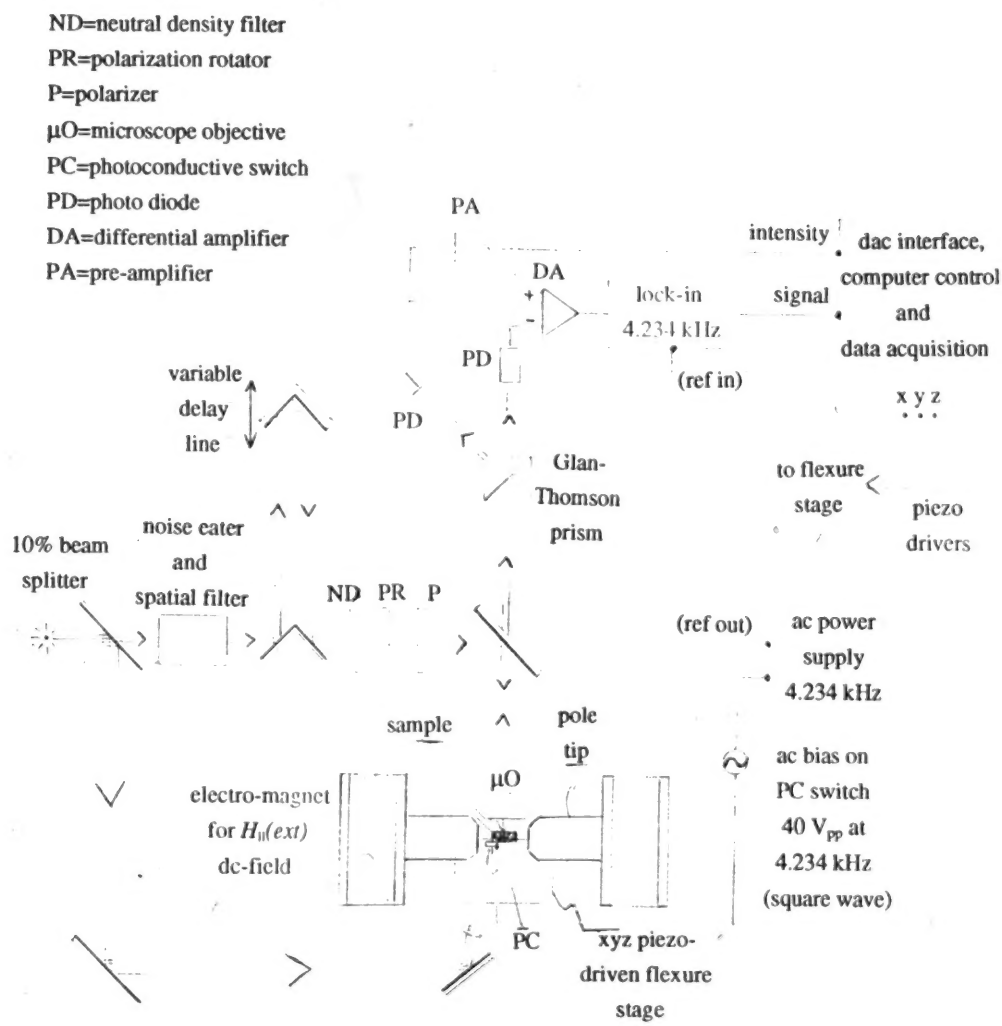

Fig 7.1 Full schematic of the polar TR-SKEM set-up used for FMR measurements.

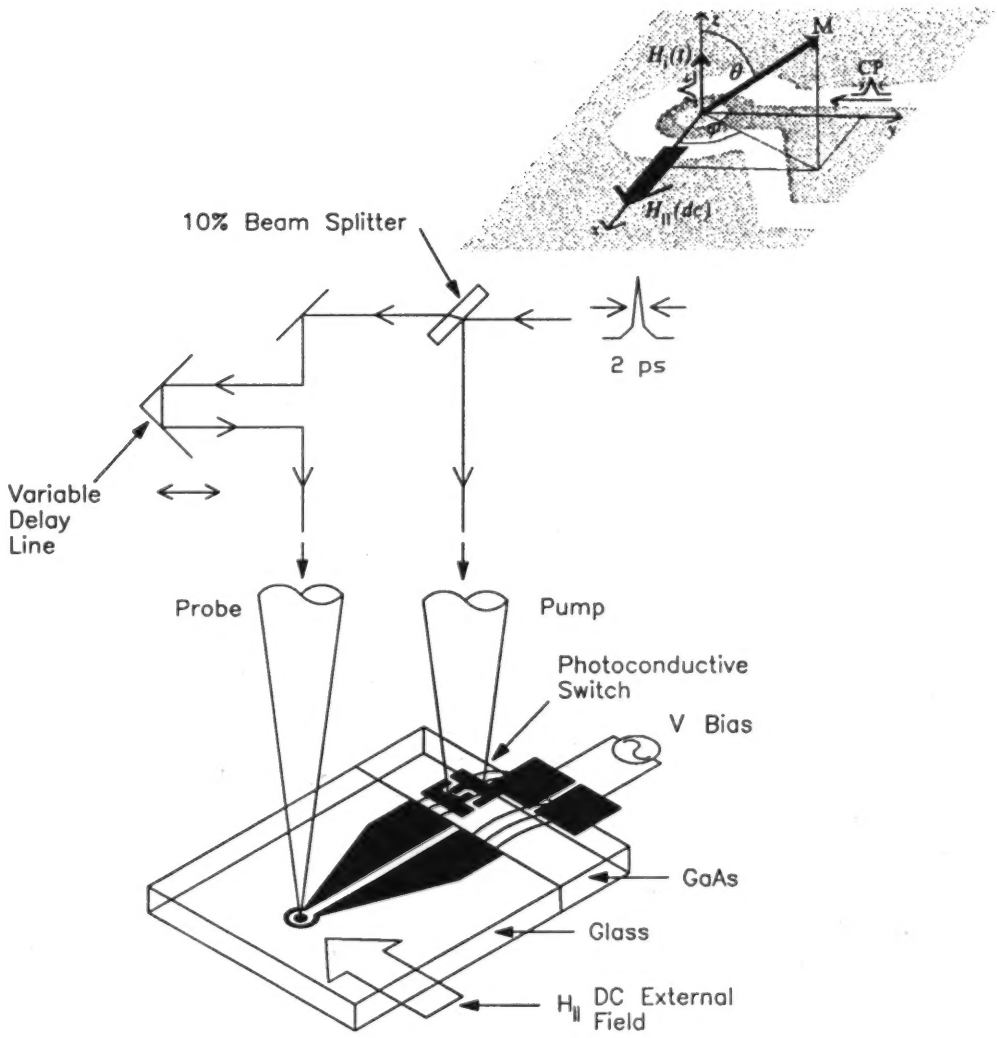

Fig 7.2 Cartoon of the pump and probe beams striking the sample. (inset) Perspective SEM image of the coil loop with axes definition overlaid.

permalloy particle is magnetically saturated in the x direction by a dc biasing magnetic field ($H_{\parallel}$) and the transient magnetic field ($H_{\perp}$) (fig 7.2 inset) sets the spins precessing. The change in polarization of the laser light, due to the polar magneto-optical Kerr effect, is differentially detected upon reflection from the permalloy giving the perpendicular magnetization component at the surface.

In the probe beam path, an electro-optic noise eater stabilizes the probe laser beam and the neutral density filter protects the sample surface from spot burning. The polarization rotator allows easy manipulation of the desired p- and s- polarized planes and the polarizer and Thomson cube complete the rotation detection optics. The split photodiode set-up allows for twice the signal compared to a simple polarizer/analyzer scheme. The amplified signal is locked into by modulating the photoconductive switch bias as demonstrated in figure 7.3[7.2]. The x-y-z piezo stage allows for scanning over the surface; the scan rate is limited, practically, by signal averaging time.

7.3 Sample Mounting and Electrical Considerations

Several issues need to be taken into consideration when mounting the sample, including stability, electrical contact and pump and probe line of sight among others. The need for stability dictated gluing the sample substrate to a printed circuit board and then gluing the ensemble to a larger mounting holder that would be screwed down to the flexure stage.

Both the photoconductive switch and the coil were connected to circuit board transmission lines by indium bonding (being a much quicker method than wire bonding). Problems occurred in our system because of the high numerical aperture microscope

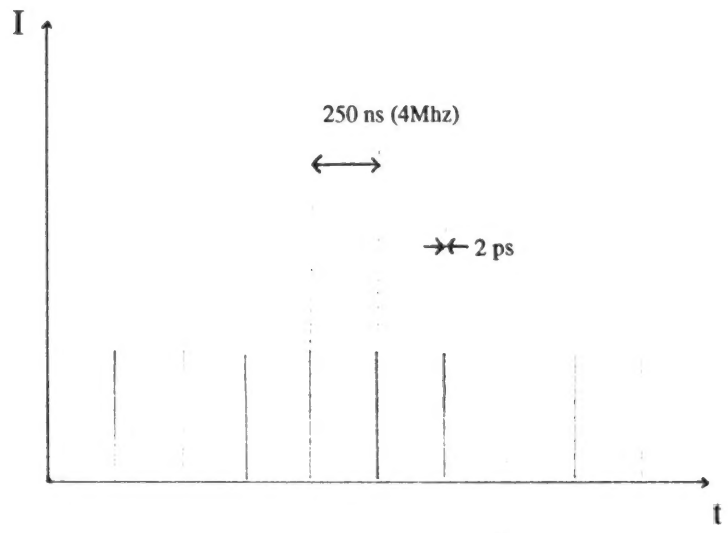

Fig 7.3(a) PC switch with dc bias: current vs time (cartoon).

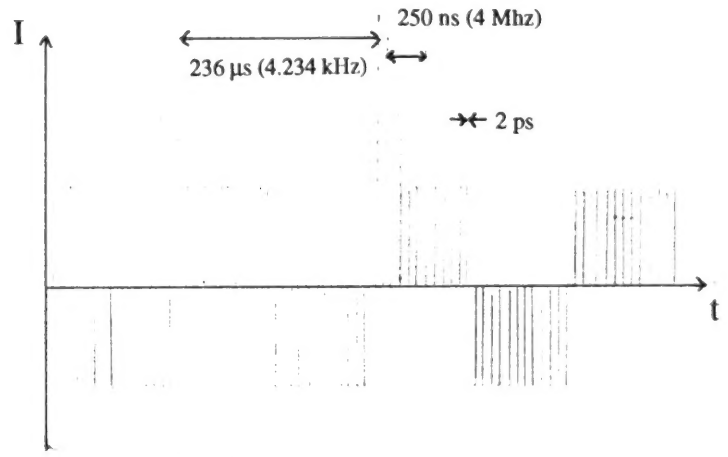

Fig 7.3(b) PC switch with ac bias: current vs time.

objective blocking the line-of-sight of the pump beam to the photoconductive switch. This necessitated a longer distance between the switch and the coil, aggravating the effects of current pulse broadening. The transmission lines of the circuit board were soldered either directly to a co-axial cable or soldered to intermediate leads which were connected to the coax. The interconnection between the coax and wire leads proved to give a very large reflection (more on the effect of electrical reflections will be given in the chapter on results) as did the wire lead to transmission line connection. The switch itself and the indium bonds did not give obvious reflections in the current pulse but probably contributed to broadening it out. In fact, the coil itself (because of the tapering width and resistance) probably increases the pulse width as well. In any case, our current pulse rise times were much larger than expected by the time they reached the coil loop (over 100 ps when they should've started under 10 ps at the switch). Some of the reflection problems were rectified by eliminating as much as possible the wire leads between the coax and transmission line. The broadening problem has to be dealt with by making the switch as close as possible to the coil loop. One idea would be to incorporate the switch right into the fabricated coil transmission line in a mask design, though this has its own problems of needing to fabricate the sample on expensive semi-conductor instead of glass. Another possibility is to shorten the coil transmission line.

Electronics considerations also played a role. A coaxial cable was needed close to the circuit board to minimize rf pickup by the wire leads. The diodes had to be selected to have a higher natural RC rolloff than the lock-in frequency. This wasn't usually a problem except when modulation was done by the photoelastic modulator (instead of the ac bias) whose 2nd harmonic was at 100 kHz. Also, the co-axial cable that carried the ac current

to the switch had to be kept as far away as possible from the cable carrying the signal; when they were running side by side the signal cable was able to pick-up enough ac even through both ground shields to add a background to the signal.

The dc external field also caused problems. The large electro-magnet coils that were used heated up at high field values which was the suspected cause of considerable thermal drift (micrometers). This was corrected by incorporating a fan. The magnet bulk also made it necessary to lower the flexure stage and have longer (higher) mounts which increased the sensitivity to temperature changes. In desiring to achieve as high fields as possible, the pole tips of the electromagnet were made close to the sample so the mount also had to be quite thin which further decreased mechanical stability. Of note, the pole tips were also made so close to try and localize flux and minimize the field in the microscope objective (expecting Faraday rotation in the lenses) but this was only necessary for hysteresis measurements, as microscope induced rotation would only give a background dc signal which would be ignored by the lock-in.

7.4 Static Longitudinal MOKE Detection Revisited

In the previous chapter much was discussed regarding the static measurement of a longitudinal Kerr system: specifically, obtaining the hysteresis curve. On first inspection, it seems that a static measurement should be easier to implement than a dynamic one, however, our experiences indicate otherwise in the case of the hysteresis.

The nature of the hysteresis curve is, of course, its irreversibility. The material's response to an external field depends upon the direction from which the field is being swept. Once critical field values are reached (coercive field, for instance) a removal and

reapplication of the field will give a different result (domain walls have moved to the other side of pinning sites, etc.). This means, when measuring the curve, the external field sweep must be monotonic and modulation is not possible. For lock-in detection we must therefore rely on the photoelastic modulator (PEM) which raises problems of its own.

Contrary to what I've just stated, however, for a very small field change (smaller than Barkhausen steps), magnetization in the material should be reversible. Alternately, for fairly small field changes, we cycle around minor hysteresis loops which close. Relying on this assumption, we lightly modulate the external field as it is swept and lock-in at the frequency of modulation (removing the PEM). This is known as the "dither" technique (see section 2.7.2). Because of the sharpness of permalloy's easy axis, using a small enough dither for reversibility is fairly difficult. Even when successful, the hysteresis curve itself would not be the result but the derivative of the curve since our signal is now from small change in magnetization and no longer magnetization itself. Figure 7.4 shows a dithered field sweep taken while defocused on a large triangle from sample "previous". Two peaks, one negative the other positive, identify the slopes of the hysteresis curve we'd expect (because of the noise, conversion to a hysteresis curve by numerical integration is not possible). Figure 7.5 is taken while defocused on a 10x10 μm square and shows more than two peaks. In fact, some peaks are traced in both directions possibly indicating a different switching mechanism (rotation instead of wall movement for example).

Further use of the dithering technique can be made for static domain imaging. Leaving the field set near an irreversible switch on the 10 x 10 μm particle should trigger domain wall jittering which shows up in spatial scans in figures 7.6(a),(b). These were

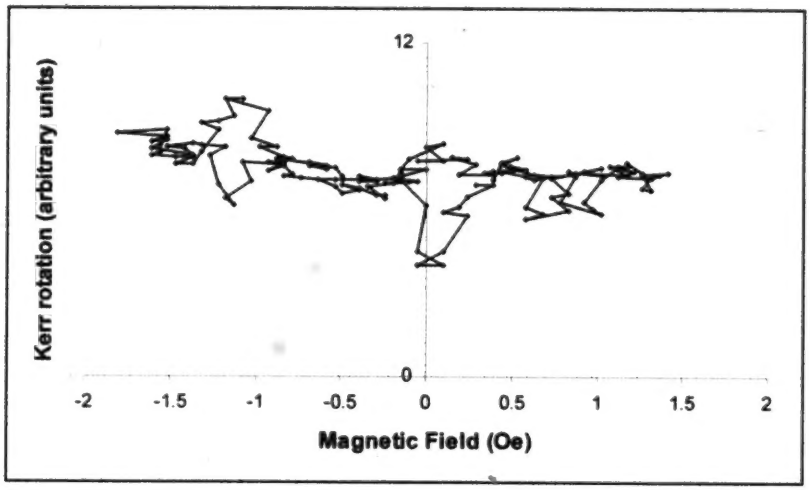

Fig 7.4 Dithered response of a triangle on "previous" to a field sweep. The positive and negative non-retracable areas signal non-retracable hysteresis slopes.

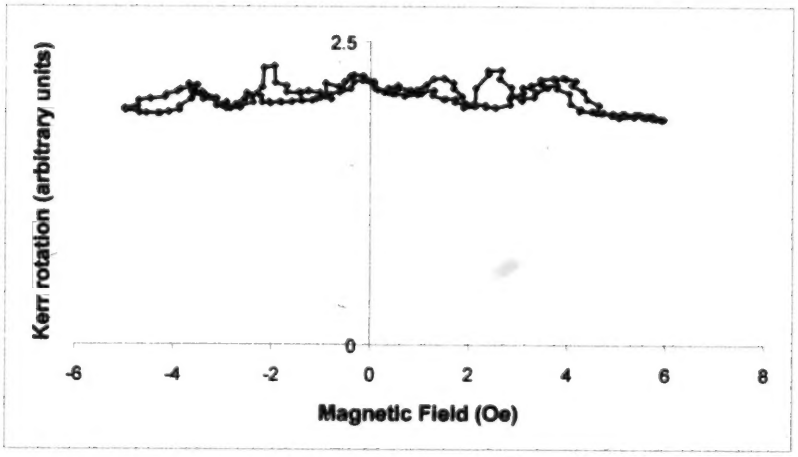

Fig 7.5 Dithered response of a 10x10 μm square on "previous" to a field sweep. Some steps are are non-retracable and some retracable possibly indicating different mechanisms for switching.

taken by maximizing the signal in the center of the particle and indicate this 10x10 μm structure is split into four closure domains. MFM images (figs 6.12 and 6.13) are of the same 10x10 μm structures and give a similar result.

I've made reference to the idea that the PEM is undesirable to have in detection. Part of the reason (which will be expanded on later) are the non-magnetic polarizations in the system. In our case, the beam splitter was discovered to be degrading the polarization information. This was solved by using a mirror cut in half (sending only half the beam into the μO as discussed in chapter 2) or obtaining a special "stress-free" beam splitter that would interfere much less, both of which worked. The μO was also found to be seriously degrading the polarization. Again, a special "stress-free" or "polarizing" μO was obtained but this did not fully solve the problem because of a spatial variation of degradation known as the "polarizing cross" (fig 7.7(a)). Light incident on a boundary that is perfectly s- polarized or perfectly p- polarized is safe in retaining its polarization. However, light incident at an oblique polarization that is some combination of p- and s- will automatically suffer degradation of the p-/s- information as it crosses the surface (Kerr effect aside) simply by virtue of the Fresnel equations. Collimated light entering the optics of a microscope objective will have pure p- or s- or close to pure p- or s- interaction only in the area designated by the central cross in figure 7.7(a) and the four "corners" of the objective will degrade the polarization. To try and restrict this problem a mechanical slit was installed to let through only the center portion of the beam (fig 7.7(c)). This introduced a host of problems not limited to the loss of spatial resolution. The amount of light being cut meant a much lower photon count (and correspondingly lower signal-to-noise ratio). The slit also added the problem of very finicky mechanical dependence; any

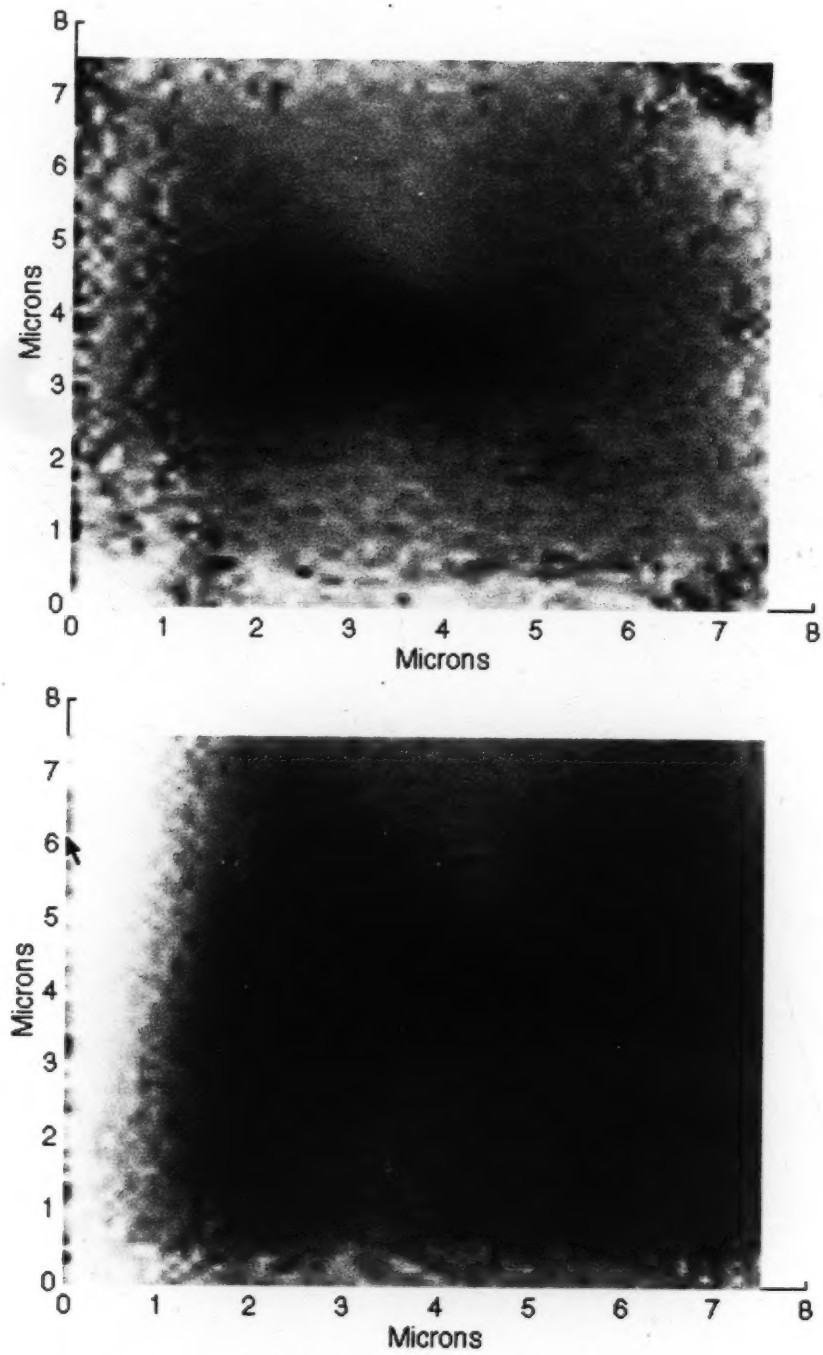

Fig 7.6(a),(b) Kerr rotation of a 10x10 μm particle from sample "previous" by dither technique showing closure domain structure.

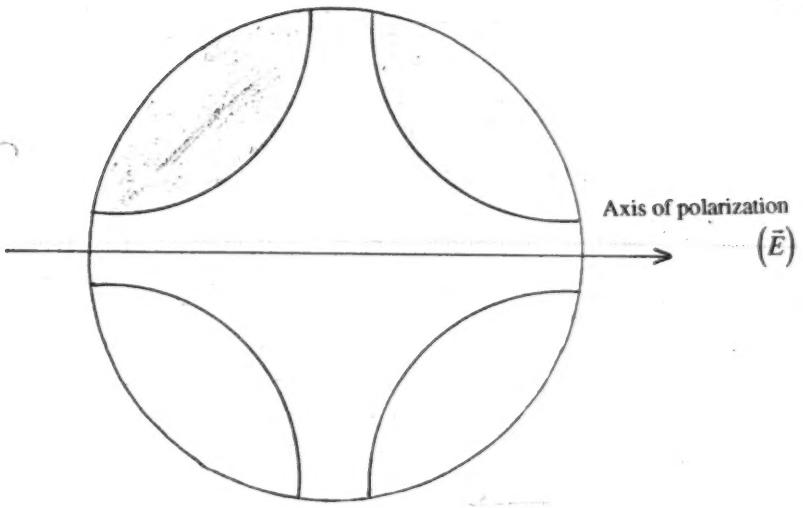

Fig 7.7(a) Collimated laser light entering the aperature of a microscope objective. Light that strikes the lenses at oblique angles (non pure p- or s-) is degraded creating the "Polarizing Cross".

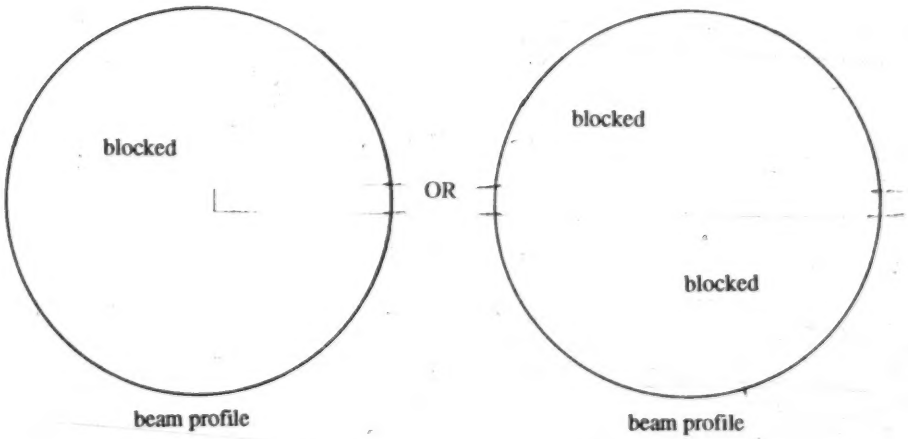

Fig 7.7(b) Introducing a mechanical slit to restrict illumination of the objective aperature.

slight movement of the beam on the slit could drastically change the signal.

Further, non-magnetic polarization rotations of the sample are picked up by the PEM (de-polarization at the edge of a sample) and can swamp the signal. One solution to this was to subtract a spatial scan with magnetic field on from one without magnetic field which would leave only magnetic rotation information (like CCD detection referred to in section 2.7.2). This proved to be unsuccessful because of the localization of the effects (at edges) being finer than spatial drift in our system. Finally combination of PEM and dither and two lock-in amplifiers was conceived of to eliminate non-magnetic polarization rotation, though this technique was not attempted.

The accumulation of improvements that removed almost all depolarizing effects made measurements with the PEM possible again. As a result Fig 7.8 shows our first hysteresis curve of a microstructure from defocusing on a large triangle of sample "previous". The hysteresis shows the structure is still very bulk like (as expected). Fig 7.9 was taken while defocused on the 10x10 μm square and reveals some of the single step switchings hinted at with the dither technique and that one would expect from the smaller size regime; this confirms the possibility of static hysteresis loop microstructure imaging with the PEM and a highly stable system.

7.5 The Generalized TR-SKEM

Some of the experimental techniques for longitudinal Kerr detection have been discussed in chapter 2. Indeed, the sensitivity and delicacy of the system were expanded upon in the previous section in discussing hysteresis measurements and critical problems were touched on. Here, we continue the discussion and set clear objectives for the

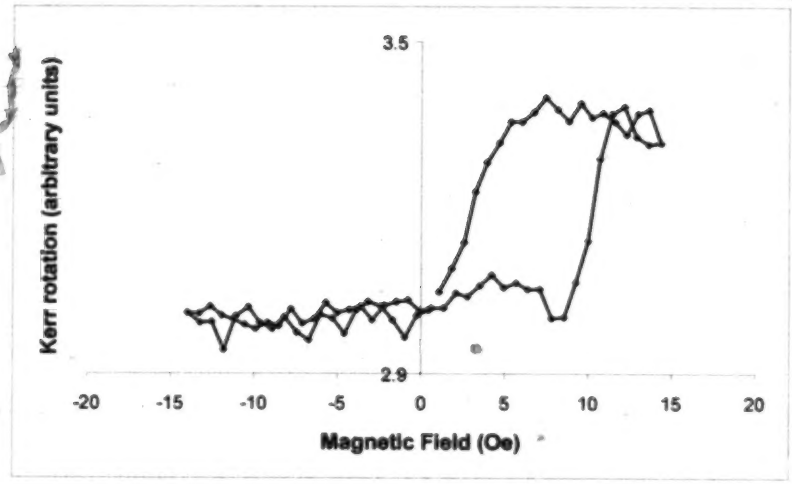

Fig 7.8 Static response of a triangle on "previous" to a field sweep. Succesful hysteresis loop measurement of a microstructure.

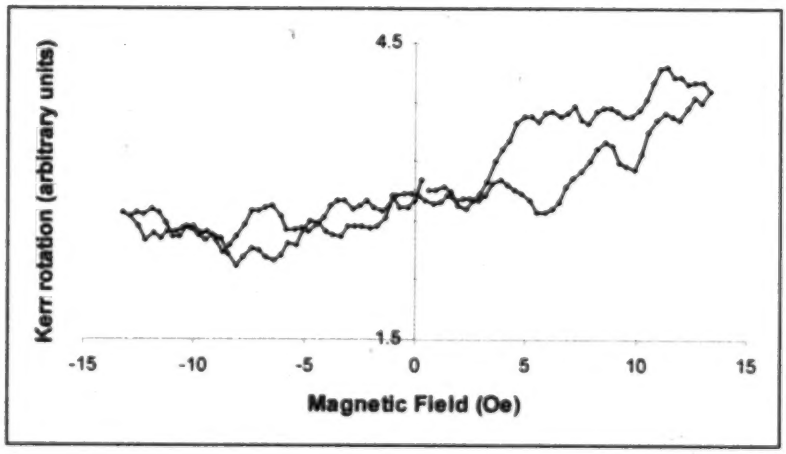

Fig 7.9 Static response of a 10x10 μm square on "previous" to a field sweep. More succesful hysteresis measurements on a permalloy microstructure, this time showing individual switchings.

successful scanning longitudinal Kerr detection system.

Because the signal tends to be very small, any depolarization interference can ruin the measurement system (especially with PEM modulation). This includes all optics in the beam path between the polarizer and analyzer so these should be minimized. In our system, elements that must sit in this path are a beam-splitter or half cut mirror, a microscope objective, and the sample itself. If the PEM is used, it must also sit in this path. Inherently, the PEM and beamsplitter (because of their "flat" interfaces with the collimated light) should be able to be completely non-polarizing (the PEM we use has been questionable in its ability to null, however, possibly due to some non-horizontal component in its modulation). The microscope objective, even if strain free, maintains its polarizing cross as discussed in the previous section. Removing all light except that which goes through the cross may be necessary to eliminate this depolarizing but using the whole objective may also be possible. If a solid immersion lens (SIL) is used[7.3] it also carries the same problem as the μO but compounded. Since the SIL sits right on top of the area of interest, the pulsed laser induced excitation may cause a time-resolved effect in the glass as well as the sample. Finally the sample itself could induce non-magnetic polarization at non p- or s- polarized reflection sites (especially edges and defects).

The other factor that is essential for several reasons is extreme stability of all elements between the polarizer and analyzer, including the beam (especially when using the PEM). With the sensitivity possible with this system, it may need to be considered as delicate as an STM or AFM scanner and kept in vibration isolation (more than just an optical table). This may include a quiet box and/or vibration platform, though bungee cord isolation is not possible unless the beam can be coupled in with a fibre. When using

the μO with a slit, very slight movement of the slit would seem like a signal as cross depolarization is introduced.

In this light, the detection system should not include the PEM unless absolutely necessary. In the case of the hysteresis tracking, it was undesirable to modulate the magnetic field in any way because of the irreversibility, so the PEM was needed. With the time resolved measurements, however, some modulated magnetic field is present anyway (fulfilling its name as a pump/probe experiment) and this can be easily adapted to lock-in detection (as in figure 7.3 with ac bias). In this way, modulation is introduced directly to the desired effect (for instance: dynamic reversal) instead of assigned to the light. It is desirable to decouple light modulation from signal modulation so that detection is unquestionably of magnetic origin (this is why the repetition rate frequency is not used for synchronizing).

In fact, the elimination of the PEM does much to eliminate the problem with the polarizing cross. Since the PEM modulates all polarization rotations, the de-polarizing due to the μO (and SIL) is picked up by the lock-in amplifier. If, however, the sample itself is modulated, rotation due to the cross becomes background which can be removed. The only catch is, since the SIL lies so close to the sample, a modulation (like, for instance, $H_i(t)$ referred to in the results) could be passed onto the SIL as either Faraday rotation in the glass or onto cross de-polarization.

The difficulty of longitudinal detection over polar detection comes from the inherent polar axis of the μO. Consider the full beam entering the objective, reflecting off the sample and coming back through (polar detection). Any irregularities in the μO (even, in theory, polarization rotation outside the cross) will be canceled by the time-reversed

path because of subtraction in our split-beam system. Furthermore, the information of the entire beam is used for optimal resolution.

When the beam is cut for detection of in-plane components, however, the symmetry is broken and depolarizing effects become severe problems, necessitating restriction of light to the polarizing cross (with a slit). This, in turn, creates the problems of a system more susceptible to mechanical movement and, a cut beam, since it only has half of the light (or worse with a slit), only retains half of the spatial resolution.

One solution that has been proposed[7.4,7.5] to overcome the latter problem relies on the time reversal symmetry breaking of the longitudinal Kerr effect. As opposed to the μO which keeps time reversal symmetry the longitudinal Kerr effect does not restore the original light polarization upon reversal. This fact may be used to subtract the two "halves" of the full Gaussian beam allowing detection of longitudinal components with the added bonus that, not only is spatial resolution retained, the time reversed polar Kerr effect is subtracted out as well.

Though this proposal uses the full beam it introduces new problems that must be addressed. Since this technique involves physically cutting the beam and subtracting the two halves, mechanical stability of the beam becomes very critical. When the two halves subtract perfectly (with respect to intensity), slight mechanical movement will create a very large non-magnetic signal as one half gains intensity and the other loses. Even still, treatment like an STM could overcome the instability and create a working system.

A proposal by the author could eliminate this dependence on beam movement and eliminate interference from μO as well with the addition of a "physical beam" subtraction to the "two half beams" subtraction system. This is done by using the Glan-Thomson and

two split PD's to work with four beams in total (fig 7.10). Split PD detector A/B by itself achieves the goal of using the full beam (to retain spatial resolution). The addition of detector C/D into the system allows the full physical beam intensity to subtract itself (eliminating the problem of the previous paragraph) because A's intensity is equivalent to C's (A and C are subtracted) and similarly, B's intensity is equivalent to D's, independent of slight movement in the full beam. Detector C/D also makes all time reversible effects in the μO (or SIL) subtract out, eliminating concern over defect in the objective (especially de-polarizing effects).

The advantage of the author's system is that it makes longitudinal Kerr measurement identical to polar Kerr measurement for the purposes of inherent favouritism of the μO polar axis and retains the advantage of a lower stability requirement. In fact, the detection scheme outlined in figure 7.10 may be toggled between polar detection and longitudinal detection merely by changing each split PD from addition to subtraction, making it an extremely versatile system.

7.6 Summary

Full details for the set-up of the time-resolved polar SKEM measurement system used for our FMR results were given including details on mounting, and electrical considerations. Discussion on the difficulties of longitudinal detection in the static case were continued, isolation and correction of the problems done, and the static hysteresis measurements of microstructures proven in principle. Thorough scrutiny of the problems of longitudinal measurement was taken, including discussions on the modulation technique and the natural advantage of the polar axis to polar effects. Finally, a combined detection

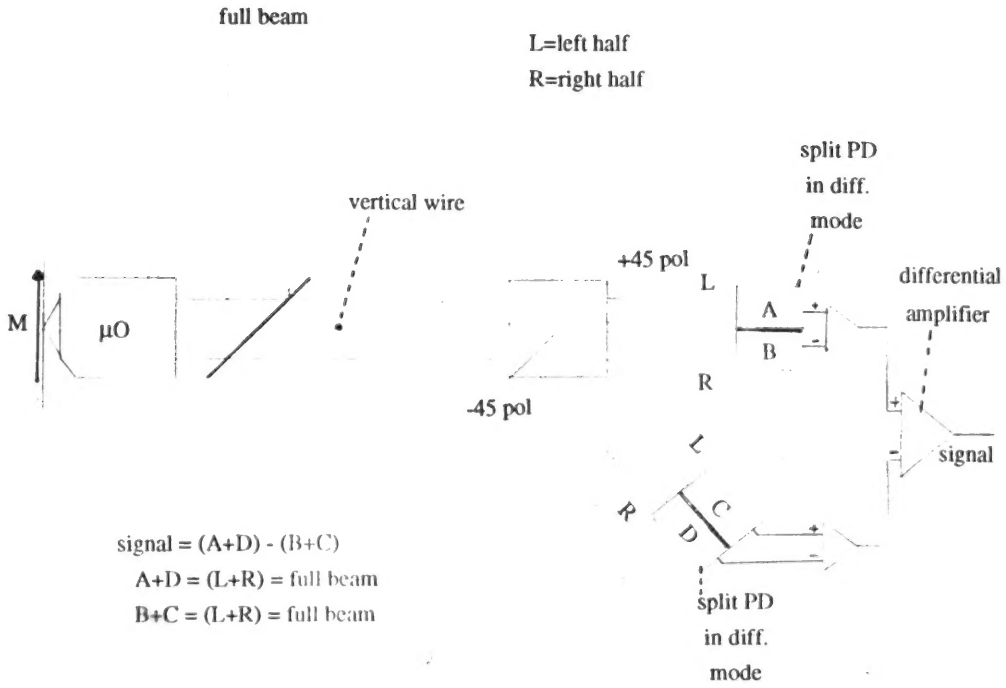

Fig 7.10 Schematic of a generalized SKEM measurement system. Physical beam intensity subtraction accompanies longitudinal effect subtraction allowing advantages of the polar axis for the longitudinal case.

scheme for both polar and longitudinal SKEM was proposed that completely differentiates between the two effects while not preferring one over the other, utilizes the full beam, maintains spatial resolution, and does not rely on extreme mechanical stability.

8 RESULTS

8.1 Introduction

A brief letter concerning many of these results can be found in a publication by the author in Physical Review Letters[8.1,*] . Initially, the goal was to use the time-resolved Kerr microscopy to study the ferromagnetic resonance and dynamic properties of a permalloy microstructure, including modeling and comparison, and to directly measure the Gilbert damping parameter. This goal broadened as the experimental technique allowed for unique analysis resolved in both time and space. Direct evidence of spatially varying magnetization response spurred a novel qualitative examination of the different resonance conditions across the microstructure.

8.2 Probe Beam "Lithography"

Direct observation of ferromagnetic resonance using the time-resolved scanning Kerr microscopy was first done on a bulk thin film as proof of principle (the film was placed face-to-face onto a coil containing glass substrate and the probe beam was focused through the glass) to obtain a characteristic time domain image (see fig 8.1(a),(b) for example). Remember that detection is of the perpendicular component of magnetization so the spin precession, about the in-plane field direction, appears as an oscillation in time.

Observation proceeded on microstructures fabricated using the double lithography technique, discussed in section 5.3.4, with the intention of measuring the characteristic

---

* A version of this chapter has been published. Hiebert, Stankiewicz, Freeman 1997. Physical Review Letters 79 (6), 1134-1137.

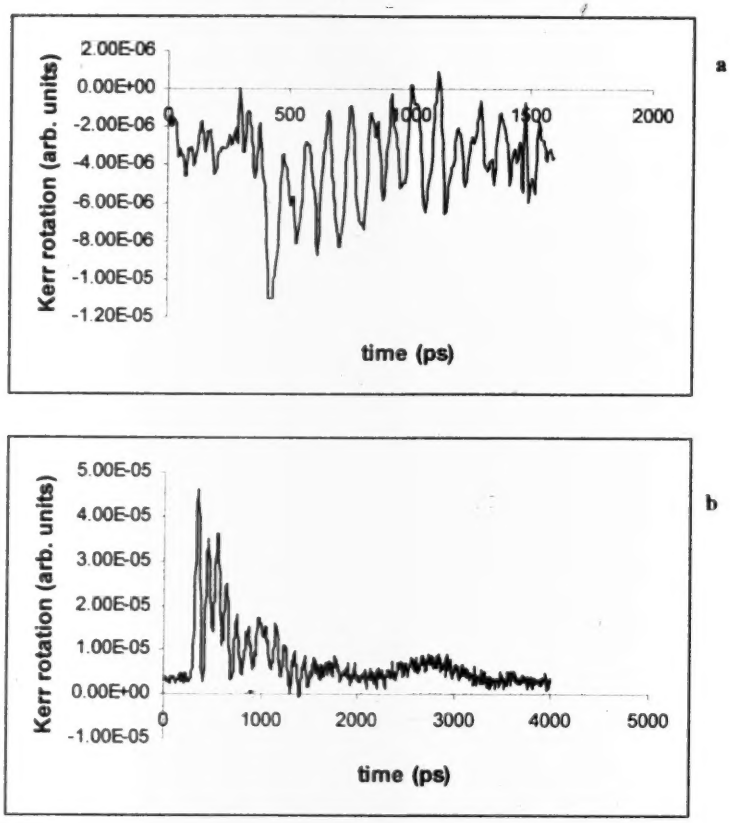

Fig 8.1 Characteristic time domain images of magnetization response. The oscillatory signal represents FMR: **(a)** sample 3.1.10, **(b)** sample 3.4.10.

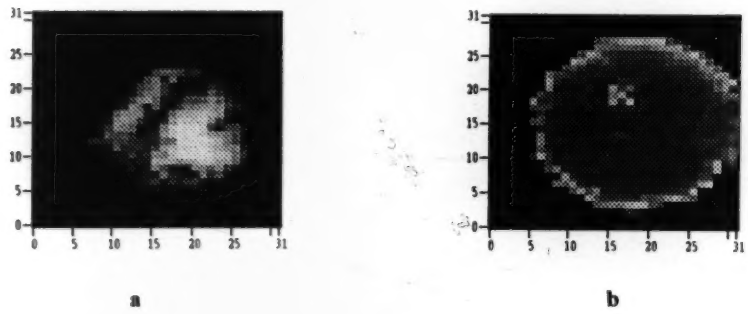

Fig 8.2 Examples of spot burning on permalloy microstructures. Samples **(a)** 3.1.10 and **(b)** 3.4.10 were lost to these defects caused by the laser.

"modal" frequencies as a function of external field strength. However, many of the samples were plagued by problems of "spot burning" on the surface (fig 8.2(a),(b)). To avoid this, the probe beam average power had to be kept under 100 μW, though the problem was never fully resolved (as will be seen even the prize sample, after a month of scanning with no problems, developed a "hole" one day with no change of the set-up or laser power). The most likely reason, because of their haphazard nature, is that the defects were caused by laser instability due to old arc lamps in the Nd:Yag pumping laser.

Could these "burns" literally be holes melted in the permalloy? A quick calculation of the energy absorbed from the laser beam could raise the temperature of the permalloy by 50 or even 100 K. This is unlikely to melt it but it could cause a change in magnetic properties (defects migrating, changing domain structure, or permalloy lifting), especially on recalling the sensitivity of permalloy properties to temperature annealing conditions discussed in chapter 3. Alternatively, the adherence properties of the thin film to the substrate could have been catastrophically altered upon the heating (due to stress change, etc.) causing a partial lifting of the film and the creation of a hillock. Finally, they could be caused by a piece of passing dust "welded" onto the surface by the probe beam. This should have less effect on the magnetic properties but could result in something as simple as domain wall pinning which could be seen as magnetic information.

Unfortunately, the sample which garnered all the results discussed in this chapter, eventually fell victim to this "burning" process, limiting its use for further experiments. SEM micrographs in figure 8.3 show pictures of the coil with permalloy microstructure inside at various magnification factors. As the image is magnified, it becomes clear that the defect is above the surface of the permalloy and has formed a hillock. This defect also

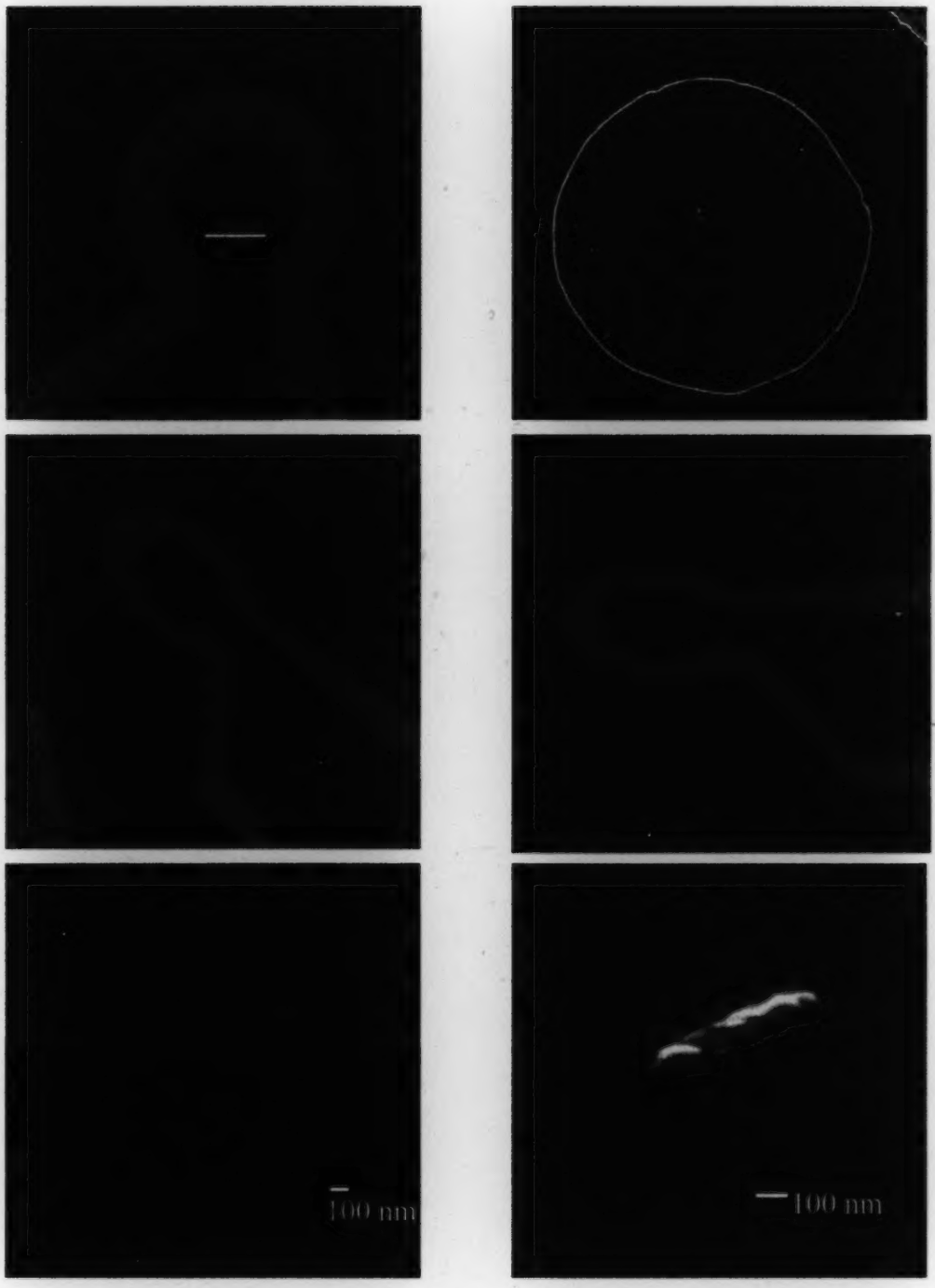

Fig 8.3 SEM micrographs at various angle and magnification of sample 3.6.8. Bright outlines in **(a)** and **(b)** and shadow in **(e)** are signatures of an undercut profile. A hillock-like defect is visible in most images.

was visible in intensity images as well as magnetic ones which tells us this particular burn was probably caused by either "spot welding" or permalloy lifting. Figure 8.4 shows spatial snapshots of the permalloy microstructure. The three images are due to the lock-in signal detecting polarization rotation and show the magnitude of the polar magnetization component with darker regions representing higher signal (of note, these and all future grey-scale images have been normalized to the min-max data range in each image). These represent a few different points in time during a tipping pulse excitation. The defect is definitely influencing the magnetic signal as can be seen in panel 1 where the defect seems to be causing some sort of quasi 360° domain wall as viewed on the top side of the picture (I say "quasi" to remind the reader that this is not a static measurement but a dynamical sampling of magnetization distribution that exists in a few picosecond window). The 2nd and 3rd panels reveal some magnetization variation as well but each is different from the other and from panel 1 also. This hints at the exciting ability to dynamically probe this type of magnetic structure spatially.

As an aside, the SEM micrographs also reveal the type of lithographic process used in this case (optical lithography and wet chemical etch). The bright outlines seen in figures 8.3(a) and (b) are signatures of an undercut profile of the patterned metal. The thickness of this outline also indicates the amount of undercutting and thus gives the viewer a feel for how thick the metal layers are compared to the patterning features (the thickness is the same order as the width of the bright lines). Figure 8.3(e) shows an angle close-up of the permalloy disk confirming that the wall edge is invisible from this angle and, therefore, does not come straight down.

This anomalous burning problem may not be totally negative. If the properties of

Fig 8.4 Spatial snapshots of polar magnetization of sample 3.6.8. The grey scale is Kerr signal showing dynamical magnetic information probably related to the defect.

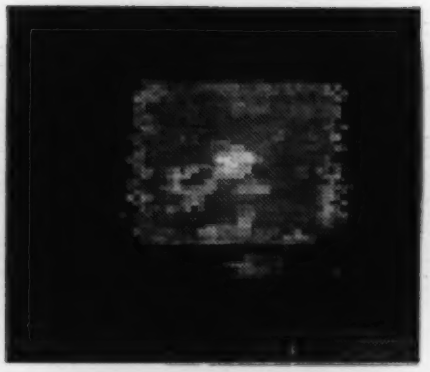

Fig 8.5 Probe beam "lithography". The field of view of this intensity image is within the borders of a topographically structureless "large triangle". The square is "writing" done by a spatial (raster) scan of the probe beam. The bright feature in the center of the square is "stronger writing" done by scanning a smaller area at higher intensity.

the burning are better understood it could even be used as a possible optical direct write lithography technique. A proof in principle of this was done on one of the large permalloy triangles (which served the purpose of alignment mark for the UV double lithography). Figure 8.5 is an intensity image taken in the middle of this large triangle after doing two scans: one in a very small area at high intensity and one in a medium sized area at medium intensity. The square that is visible is the "writing" done by the "medium" spatial scan (similar to the trace box left after an SEM high magnification image). Inside "the box" is also visible the "extra writing" of the high intensity scan. The beam average power was 120 μW on /60 with a .75 NA Olympus objective. If this lithography is a result of energy transferred heating the material, this technique might be used to temperature anneal only selected parts of a permalloy microstructure giving the novel ability to "pattern properties" into a substrate!

8.3 Time Scans: FMR Frequencies

Figure 8.6 shows time scans at the center of 3.6.8 (prior to spot burning) for various external field strengths. The oscillation envelopes have two peaks due to a reflection in the transmission line. Notice that the amplitude of oscillation generally decreases as the field strength increases. This behaviour has previously been observed in magnetic garnet films[8.2] and is related to the finite bandwidth of the magnetic pulse. Note also that the frequency of oscillation increases with external field, as is expected for the Larmor precession, and the amplitude of oscillation decreases with time due to damping.

The characteristic or modal resonance frequencies are obtained by taking the Fourier transform and looking at the maximum in the power spectrum. From this, we can

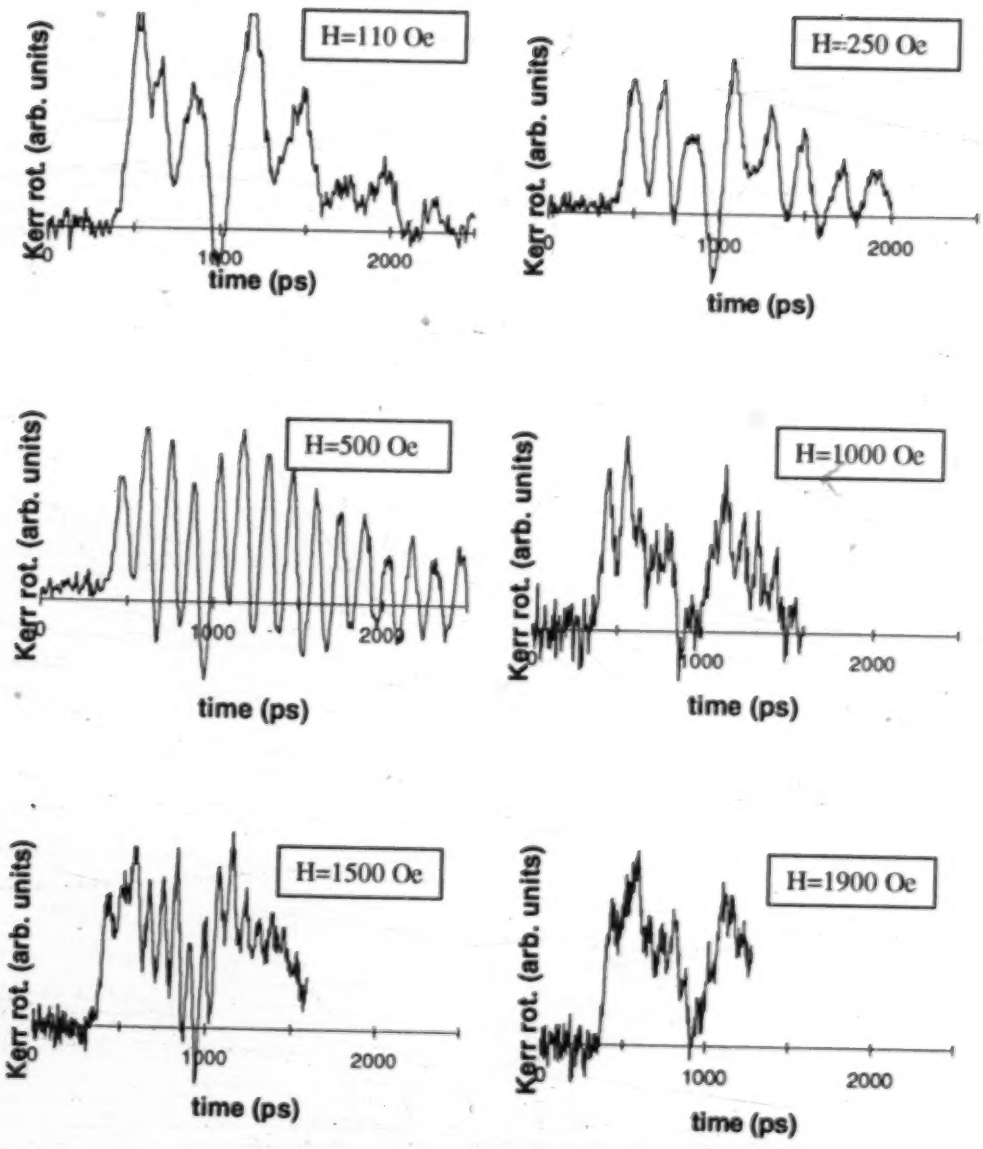

Fig 8.6 Time domain images of magnetization response for external fields of 110, 250, 500, 1000, 1500, and 1900 Oe, respectively. FMR oscillations of differing frequencies are visible.

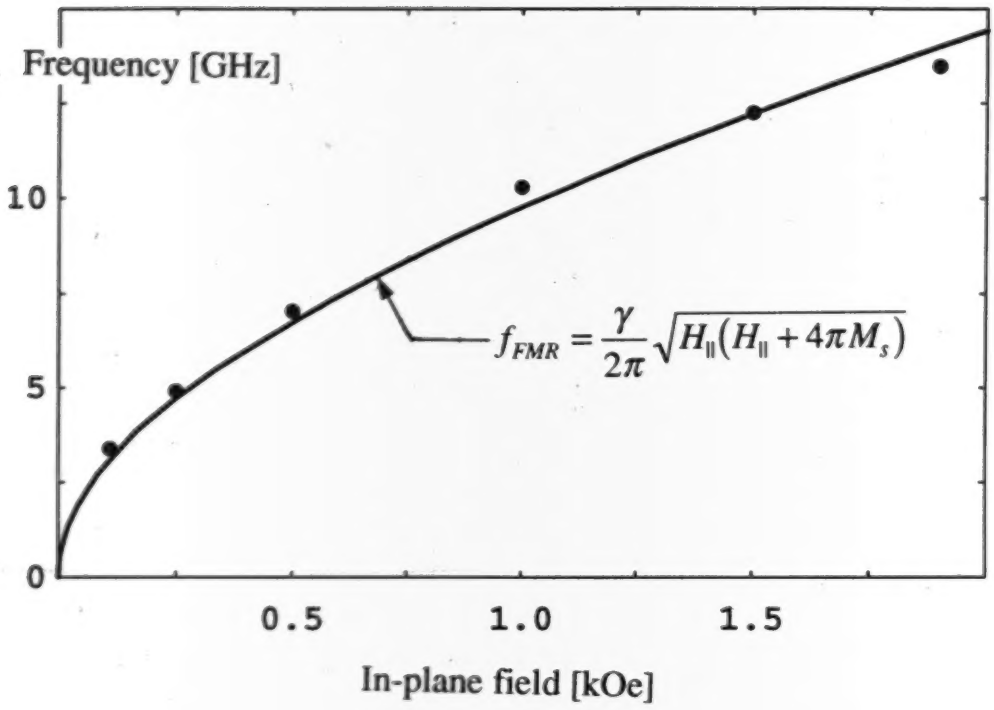

Fig 8.7 Frequency vs field for modal FMR in a permalloy microstructure (3.6.8). The solid line is the expected FMR (from Landau-Lifshitz equations) for a uniformly magnetized easy-plane ferromagnet, fitted to the experimental points by using $4\pi M_s$=10.8kG.

determine the frequency vs. field for the oscillation (fig. 8.7). This can be compared to the expected resonance frequency for a uniformly magnetized easy-plane ferromagnet (cf. section 6.3) and shows excellent agreement with a value of $4\pi M_s = 10.8$ kG. As referred to in chapter section 6.3 this value was measured for a bulk film of permalloy using SQUID Magnetometery and disagrees by only around 20 %. A similar analysis (using an alternate experimental technique) which culminates in this frequency vs. field measurement appeared recently in Applied Physics Letters and agrees with our result quite well[8.3].

8.4 Non-Uniformity: Spatial Variation of Magnetization

Though the above agreement suggests a secondary role for non-uniform oscillation behaviour, one would expect some non-uniformity in the magnetic response of the structure. First of all, the excitation field will vary spatially over the sample because: (i) the radius of the coil is not large compared to the size of the particle (16 μm compared to 8 μm), (ii) the particle isn't centered in the coil (it is closest to the top or "north" part of the coil as seen in fig 8.3(a)), and (iii) the fact that the coil is only 3/4 of a complete circle. Furthermore, free pole demagnetizing energy changes the resonance conditions at the edges of the structure. For these reasons, a study of the spatial response of the magnetization as snapshots in time was undertaken.

Figures 8.8 and 8.9 demonstrate the uniqueness of the TR-SKEM technique in its ability to resolve both time and space simultaneously. The first figure is in the time domain and representative of previous figures. Spatial scans were taken at each of the oscillation peaks in this time domain figure (to maximize signal) to obtain these grey scale images (fig 8.9).

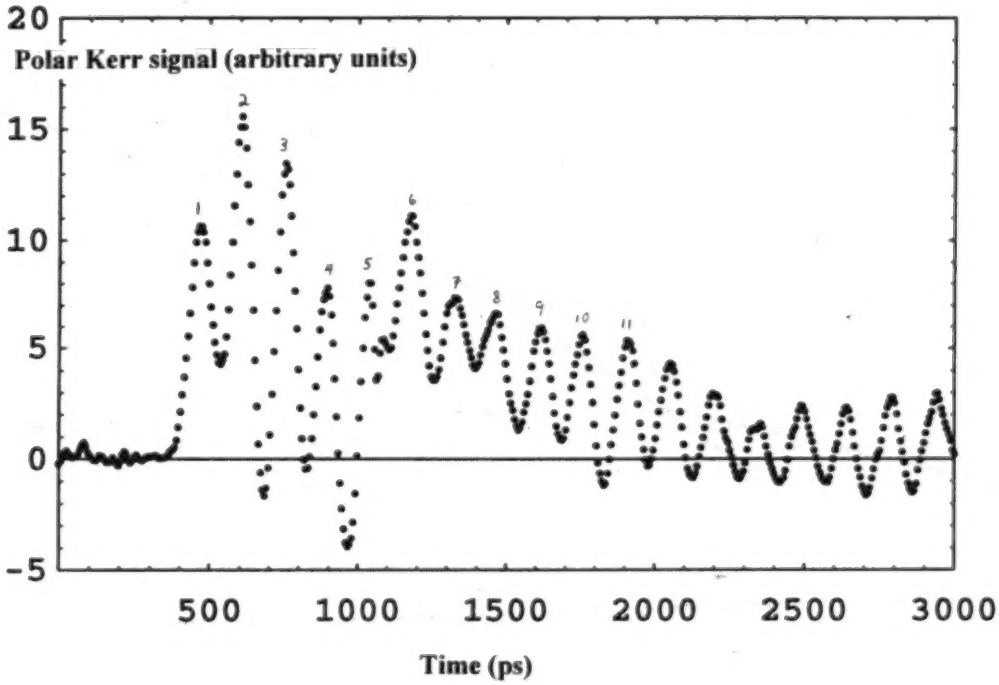

Fig 8.8 Time domain response at $H_{\parallel}(ext)$=500 Oe. Numbers above the peaks correspond to spatial magnetization response snapshots at these times and are represented in figure 8.9.

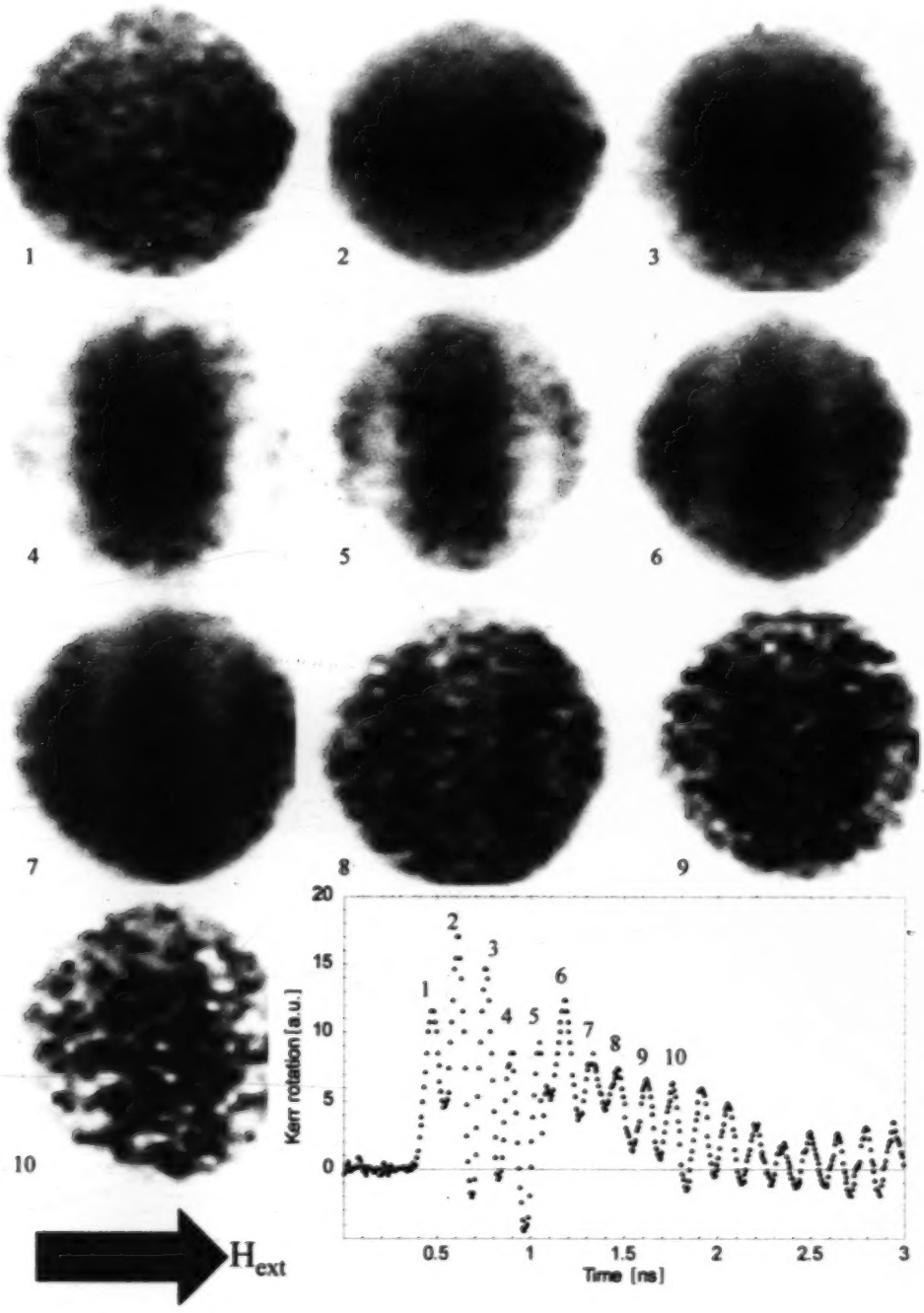

Fig 8.9 Evolution of spatial magnetization response. Broken circular symmetry, imposed external field direction symmetry, and "top/bottom" asymmetry are all evident in the response.

The first thing to note is that these images show breaking of the circular symmetry. This might be due to the fact that the coil is a broken circle or from the anisotropy field but these reasons are unlikely because, as will be seen later, the symmetry is similarly broken on rotation of the sample by 90°, not dependent on these substrate defined directions. It is very likely, then, that the external field acts to break the symmetry, which it can do in a couple of ways (fig 8.10). First, the demagnetizing energy is preferentially lowered or raised for edges parallel or perpendicular to the external field, respectively (fig 8.10(a)). Second, the oscillation is not circular in θ/φ space because of the strong planar demagnetizing energy.

We consider the first explanation (fig 8.10(a)) to be most likely. Consider the spins at edges parallel to the external field. A cross section perpendicular to the external field (first inset of fig 8.10(a)) reveals that these spins would require no extra energy to align with the field because they are parallel to an edge. Now, consider the spins at edges perpendicular to the field (i.e. the cross section parallel to the field). The demagnetizing energy is directly at odds with the external field energy. Furthermore, we should note two important magnetic properties here. First, the sample thickness is much greater than the range of exchange forces ($\propto \sqrt{A/\left(2\pi M_s^2\right)} \approx 100$ Å). This means that the spin direction can change through the thickness without adding much energy. Second, permalloy has a saturation magnetization ($4\pi M_s$) of ~ 10000 G while the external field is only 500 Oe so $H_1 << 4\pi M_s$. It is thus likely that the disk is not saturated right to the edge in the dc state, but rather but more like the latter cross-section (second inset) in 8.10(a). These magnetically softer regions would surely respond quickest or with greatest amplitude to

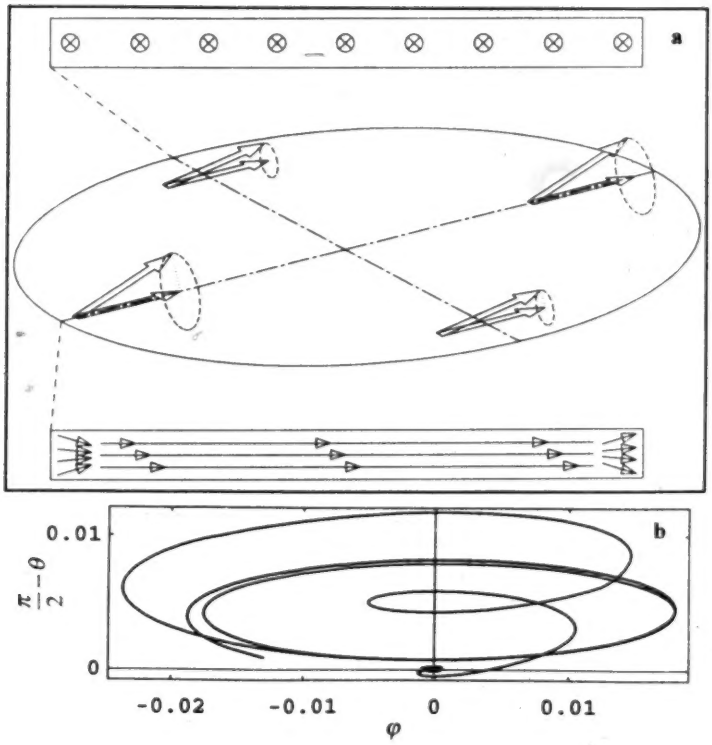

Fig 8.10 Possible reasons for symmetries observed in figure 8.9: **(a)** demagnetizing effects at the edges carrying free poles, and **(b)** asymmetry of the magnetic vector phase trajectory.

the pulsing field as seems to be indicated in panels of 8.9, and could even act as sources of propagating non-uniformity ("shock wave" sources).

The second explanation (fig 8.10(b)) is less compelling. Because of the large out of plane depolarizing energy the tip of the oscillation vector would follow a strongly elliptical path with major axis in the plane (see fig 7.2 for polar coordinate definition). If one considers this vector oscillating at a parallel edge, the large φ has to work against demagnetizing energy making oscillation unfavourable; at a perpendicular edge, large φ actually decreases demagnetizing energy making oscillation favourable.

Let us go back now to the figure 8.9. Panel 1 starts at the first peak of the time domain oscillation (fig 8.8) and seems to show excitation of the statically demagnetized edge as might be expected. As we move from peak to peak along the time domain we can see these excitation points moving in towards the center meeting in the 4th peak image. If we look at peak 5 now we can see the excitation beginning again at the edges. This corresponds to the onset of the transmission line reflection giving the particle another "kick". This continues on through peak images 5, 6, and 7, this time with the center remaining excited from the initial pulse, giving very rich spatial structure associated with this double kick. The propagation of an asymmetry between top and bottom is now even visible in images 5, 6, and 7 which is likely due to a combination of incompleteness of coil circumference and off-centeredness of the sample. The incomplete circle will cause the tipping field to be stronger near the "north" side of the disk (away from the coil gap) while the physical positioning of the structure being closer to the "north" will also break symmetry, though it is not clear whether it will make a stronger pulse in the north or south side. In images 5, 6, and 7, "north" is at the bottom of the figures and it seems the tipping

field is more strongly felt in the south initially (during the onset of the second pulse) so this section exhibits higher response in figure 5 which then propagates north in figures 6 and 7 as the tipping field recedes. It may also be that the tipping pulse is largest in the north but takes time to saturate there (that is, it doesn't saturate until peak image 7) and what seems like a pulse pump in the south in 5 and 6 may be leftover response from earlier excitation. The reason that only the second pulse and not the first gives rise to top bottom asymmetry may be due to the lower bandwidth contained in the second pulse. The second pulse, having a shallower slope, has less ability to "spark" resonant response then the first pulse which means it is easier to see the overall tipping amplitude reflected in the second pulse (the tipping amplitude is what carries the top/bottom asymmetry information) Peaks 8, 9, and 10 seem to be far enough away from the initial pulses to have decayed into a more uniform mode of oscillation as their spatial profiles reveal very little structure. This seems reasonable, as the amplitude of the tipping pulse at these peaks is diminished and its slope is very shallow, meaning the leftover pulse does little further excitation allowing decoherence effects to level out the spatial response.

8.5 The Tipping Field: $H_1(t)$

Much analysis has relied on the shape and strength of the tipping pulse at different places on the disk. Modeling work will be shown which requires this shape and its features for numerical solutions. Yet to theoretically determine the field values, with an incomplete coil loop, undetermined current density profile through the coil, and reflections adding to the irregularity and complexity of the pulse, any attempts to calculate or model the tipping pulse profile would be impractical. For this reason, the scanning procedures

were repeated at high external fields, following the ideas of reference 8.2. A time domain trace was taken (focused on the center of the particle) at 2.17 kOe. At the higher fields magnetization response to the permeating tipping field becomes sufficiently rigid to mimic that field; once high enough, the resonance oscillations reveal the shape of the pulse up to the bandwidth of oscillation. If one then uses (low pass FIR and median) low pass filters (to remove the resonance frequency information) and interpolates the point scanned time-chart, a continuous tipping pulse function $H_i(t)$ is created accurate up to the low pass cut-off frequency (fig 8.11). As long as we keep enough bandwidth, this treatment does not alter the pulse features important for particle excitation in smaller in-plane fields.

A note should be made here about the sensitivity of modeled results to the initial slope of the interpolated tipping pulse. Because the oscillatory modes that are excited are very much dependent on a strong component of their particular frequency with the bandwidth of this rising edge, some of the modeling results for some frequencies are extremely sensitive and sometimes entirely dependent on minute changes in this initial slope. This problem was best handled by solving for several different external fields (therefore several different modal frequencies) using the identical tipping pulse for each. In this way, only a very small range of initial slopes would reproduce each modal excitation keeping the same overall normalization, and we could expect these slopes to fairly accurately represent the true tipping pulse. In practice, this was done by truncating the pre-pulse excitation whose initial curve to the slope we believed was trimming a lot of higher frequency excitation in the bandwidth (results of this simultaneous fitting are given in section 8.8).

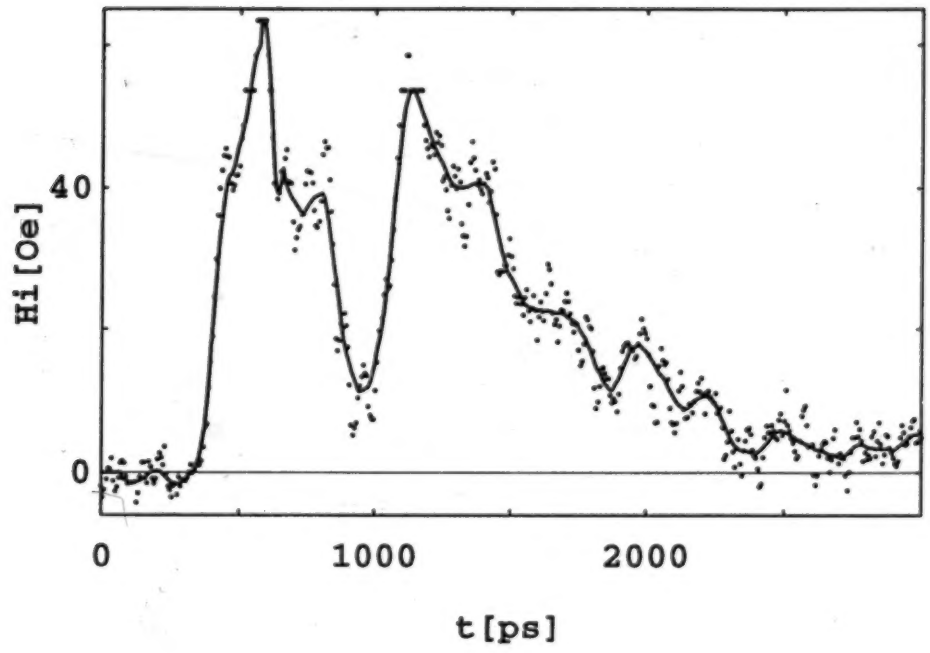

Fig 8.11 Time domain image of magnetization response in a high field (2.17 kOe): *points* - experimental data; *solid curve* - interpolation of the point scan to a continuous function (with filtering) to create the tipping pulse function $H_t(t)$.

Finally, once an interpolating function was formed for $H_i(t)$, the area underneath it (multiplied by the repetition rate) could be calibrated with the RMS current measured in the switch-transmission line circuit allowing an approximate, absolute magnetic field scale for the tipping field vertical axis. To convert current to magnetic field, the simple assumption was made that the coil was a 20 μm diameter one full loop turn. Because the inner and outer diameters were 16 and 32 μm respectively, a better choice for diameter might have been 24 μm (noting that the current density through the coil width was probably fairly uniform). Furthermore, since the circle was not a complete loop, we could assume some weakening of the field. Because of this, qualitatively, the vertical axis on the tipping pulse may be about 20 % too large, but it was only given as approximate anyway.

We have also seen that this tipping function should vary spatially over the disk. Spatial scans at high field were taken to try and elucidate this behaviour as well as to see the change in demagnetization effects. Figure 8.12(a) shows the spatial response on the first and second peaks of the 2.2 kOe oscillation. As we would expect, the magnetization varies little (the amplitude of oscillation is small) and only a "crescent moon" is visible on the "north" side of the first peak, presumably corresponding to the asymmetry of particle placement (closer to the north in the coil) and/or the gap at the south side of the coil. This gives us some qualitative feel (which we will be limited to) for the spatial dependence of the tipping pulse (a numerical modeling of tipping field distribution inside the coil would help to make this semi-quantitative). For all calculations the interpolating function taken *at the center of the particle* will be used. Demagnetization (dc-field) symmetry is almost non-existent which is consistent with the higher field doing a better job of saturation in the static state. For the lower field of 1.1 kOe (fig 8.12(b)), the demagnetizing symmetry has

Fig 8.12(a) Spatial response of 3.6.8 under 2.17 kOe external field. Tipping pulse asymmetry is visible and external field imposed symmetry is notably absent.

Fig 8.12(b) Spatial response of 3.6.8 under 1.1 kOe field. Some external field symmetry imposition has been restored at this lower field but is gone by the second peak.

reappeared on the first peak but is undetectable by the time the second peak is reached confirming that demagnetizing energy plays less of a role at higher fields.

8.6 Magnetic Modeling: Numerical Solutions to the Landau-Lifshitz-Gilbert Equation

So far, the time domain images have been intuitively insightful for viewing the particle response and oscillatory behaviour. They have also provided a check against the ferromagnetic resonance model for the easy-plane ferromagnet by assigning a modal frequency to the oscillation. Much more information may be extracted however with more detailed modeling by solving the Landau-Lifshitz equation using the actual shape of the tipping pulse we have "derived" above and later, in fact, through iterative procedure.

In the angle variables (θ,φ) defined in figure 8.13 we have a constant length magnetization vector of $\mathbf{M} = (M_x, M_y, M_z) = M_s(\sin\theta\cos\varphi, \sin\theta\sin\varphi, \cos\theta)$. Using this form of magnetization, the Landau-Lifshitz-Gilbert equation takes on the form:

$$\begin{cases} -\dfrac{d\theta}{dt}\sin\theta = \dfrac{\gamma}{M_s}\dfrac{\delta w(t)}{\delta\varphi} + \alpha\dfrac{d\varphi}{dt}\sin^2\theta \\ \dfrac{d\varphi}{dt}\sin\theta = \dfrac{\gamma}{M_s}\dfrac{\delta w(t)}{\delta\theta} + \alpha\dfrac{d\theta}{dt} \end{cases}$$

where α is the dimensionless damping constant and w is the free energy density. In our case, we limited the free energy density to demagnetizing and Zeeman contributions for an infinite layer (i.e. uniform in the whole volume of the particle) to make the calculation tractable (edge demagnetizing contributions are not included because of the complexity they would have with the circular particle, though can be used in the future with

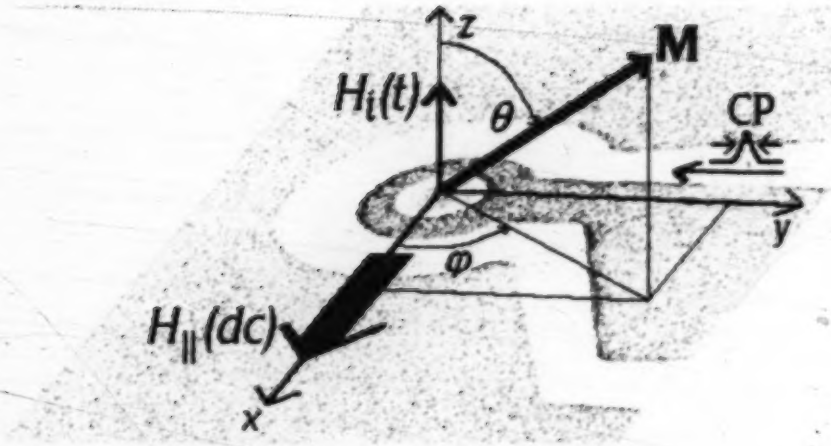

Fig 8.13 SEM of the permalloy particle in coil, annotated to show alignment of the magnetic fields $H_{||}$ *(dc)* and $H_t(t)$. $H_t(t)$ is induced by current pulse, CP.

rectangular particles). It takes the form:

$$w = w_d + w_h = 2\pi M_z^2 - \mathbf{MH}(t)$$

where $\mathbf{H}(t) = \left(H_t, 0, H_i(t)\right)$. The calculated value of $M_z(t)$ may be converted into Kerr rotation angle $\phi(t)$ using the proportion $\phi/\phi_0 = M_z/M_s$, where $\phi_0 = 2.5$ mrad is the specific polar Kerr effect rotation attributed to light reflection from a perpendicularly magnetized surface (recall that $M_z(t)$ itself has uncertainty already of ~ 20 % from the assignment of a vertical axis to the interpolating function).

Figures 8.11 and 8.14 show the result of this modeling. 8.11, as discussed earlier, gives the interpolating function which serves as the envelope for the numerical solution. Fig 8.14 is the time domain response at 500 Oe and at the center of the particle (for which we have already seen several spatial snapshots (figs 8.9)) overlaid with the numerical solution. Parameters used in the fitting included the saturation magnetization ($4\pi M_s = 10.8$ kG from previous fitting of the FMR frequency data - fig 8.7), the gyromagnetic ratio ($\gamma = 1.76 \times 10^7 \left(\text{s Oe}\right)^{-1}$), and the damping parameter α. Of the above, only α was allowed to range and in this case was assigned a value of $\alpha = 0.008$. As can be seen the fit is not fully successful, probably indicating that the non-uniformities (not accounted for in the model) do, indeed, play an important role. The first four peaks agree fairly well. This is before the shock waves meet in the middle of (fig 8.9) panel 4 and also before the second pulse has arrived. Peaks 5, 6, 7, and 8 don't agree as well and, in fact, have a phase lag. This makes sense if attributed to the non-uniformity of response as these are the places that show the richest spatial structure (fig 8.9). Peaks 9, 10, and 11 agree

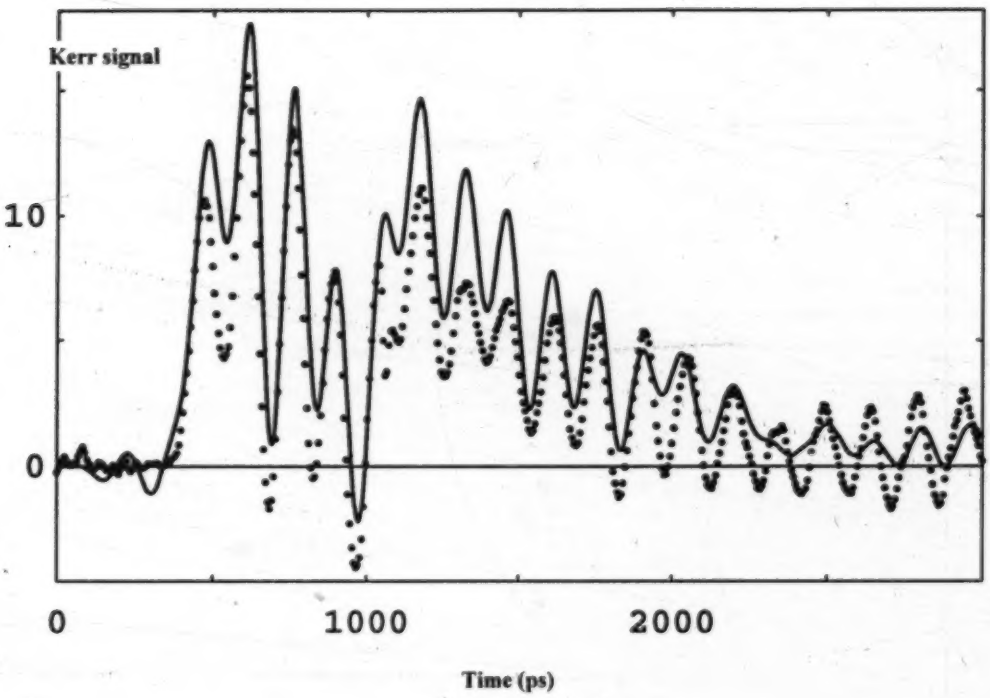

Fig 8.14 Numerical modeling of the magnetization response (solid curve) overlaying the experimental data. Agreement is lost at the 5th through 8th peaks where non-uniform effects may be invalidating the modeling assumptions.

somewhat more with the data, again, coinciding with settling down of the spatial response.

The modeling is not completely satisfactory in this case with the double pulse exciting field. Features are reproduced generally, though the value for the damping parameter may just as easily have been chosen to try and make peaks 5 through 8 agree with the data, so must be taken only as an order of magnitude at this juncture.

8.7 More Investigations of the Spatially Varying Magnetization Response

Spatial non-uniformity has been shown at 500 Oe and initial modeling done. A limiting of this non-uniformity has been shown at 2200 Oe and a partial limiting at 1100 Oe. It is of interest to check the spatial response at other external fields to confirm similar response. In fact, the power of temporal and spatial resolutions has some aesthetic advantages not yet fully explored. It would be intriguing to take enough spatial images to "fill in" the oscillatory behaviour so that viewing them in succession gives a feel for the dynamical oscillation. An external field of 250 Oe is used to illustrate this because of its slower oscillation and higher amplitude for better signal. The time domain image is shown in figure 8.15. This time, spatial scans are taken at the noted points: on the initial slope, at each peak, at each valley, and in between. Results were limited to times before the second pulse. Many of the images show non-uniformity of the tipping pulse (with crescent moon excitation on the north sides) and all show in-plane field symmetry substantiating our ideas about the causes of symmetry. Excitation maxima occur at both the center and demagnetized edges as usual, but also at four corners for panels 9 and 10.

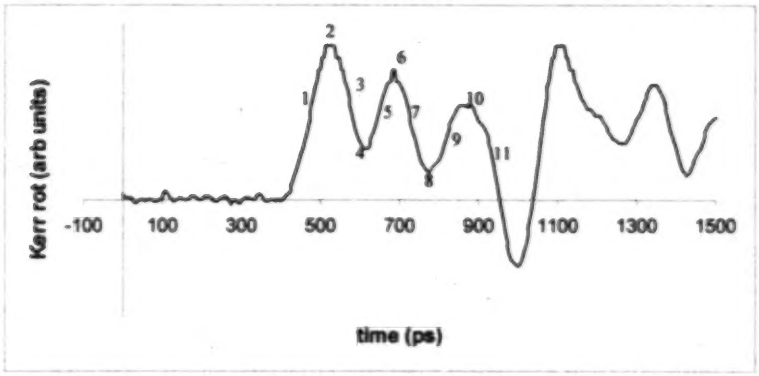

Fig 8.15(a) Excitation oscillation at 250 Oe. Numbers given correspond to the panels containing their spatial snapshot in time.

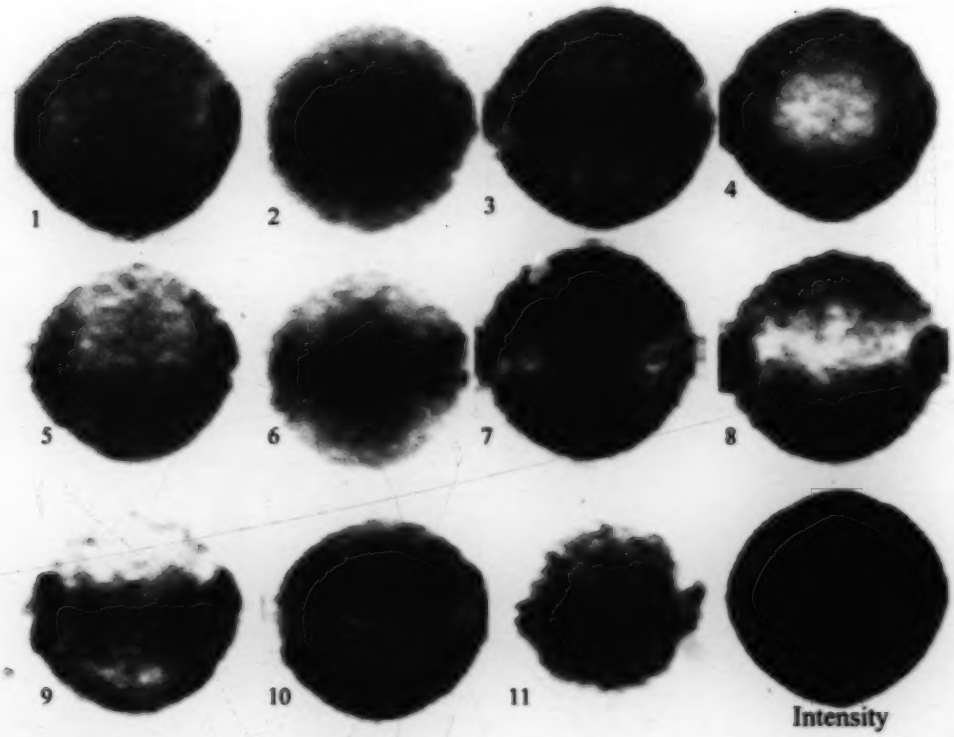

Fig 8.15(b) Temporal evolution of spatial response. The possibility exists to animate this evolution. Panels 9 and 10 show four corner symmetry.

The argument that the magnetization is most spatially rich, and therefore most non-uniform, after a double kick has been invoked several times. Presumably, the modeling done in figure 8.14 is in disagreement because of this spatial richness. Spatial scans at 250 Oe, taken after the onset of the reflection pulse, support these suppositions (fig 8.16). Panels 1 and 2 show the sharpest polarity change we've seen on vertical lines left and right as the center excitation is splitting into two on peak 2. Peaks 3 through 6 show two and sometimes three excitation points (all excitations reflect the in-plane induced symmetry) and peaks 7 through 11 show continuance of some excitation though they begin to be lost in the noise and perhaps begin to settle down.

8.8 Rotation by 90°: Spatial Variance Confirmation, New Tipping Pulse, and Precise Modeling Results

In order to confirm the reasoning for symmetry breaking, the sample was rotated 90° and the experiment repeated. If the induced anisotropy was to play a role, it would be seen here. Because the reflection was bothersome for modeling purposes, care was taken in remounting to try and minimize it as discussed in section 7.3. Figures 8.17 summarizes the spatial findings at 90° where the dc external field is again in the horizontal plane at 250 Oe, but the coil break is off to the right instead of above. Peak 1 occurs on the upward rise of the current pulse and doesn't show much information. Peaks 2 through 5 show spatial structure that is again consistent with our idea of the dc field symmetry (the preferred depolarizing edges begin the response that propagates towards the center). Peaks 1 and 2 again reveal the uncenteredness of the tipping pulse as the response is higher on the left side (away from the coil gap and closer to the coil - on the north side).

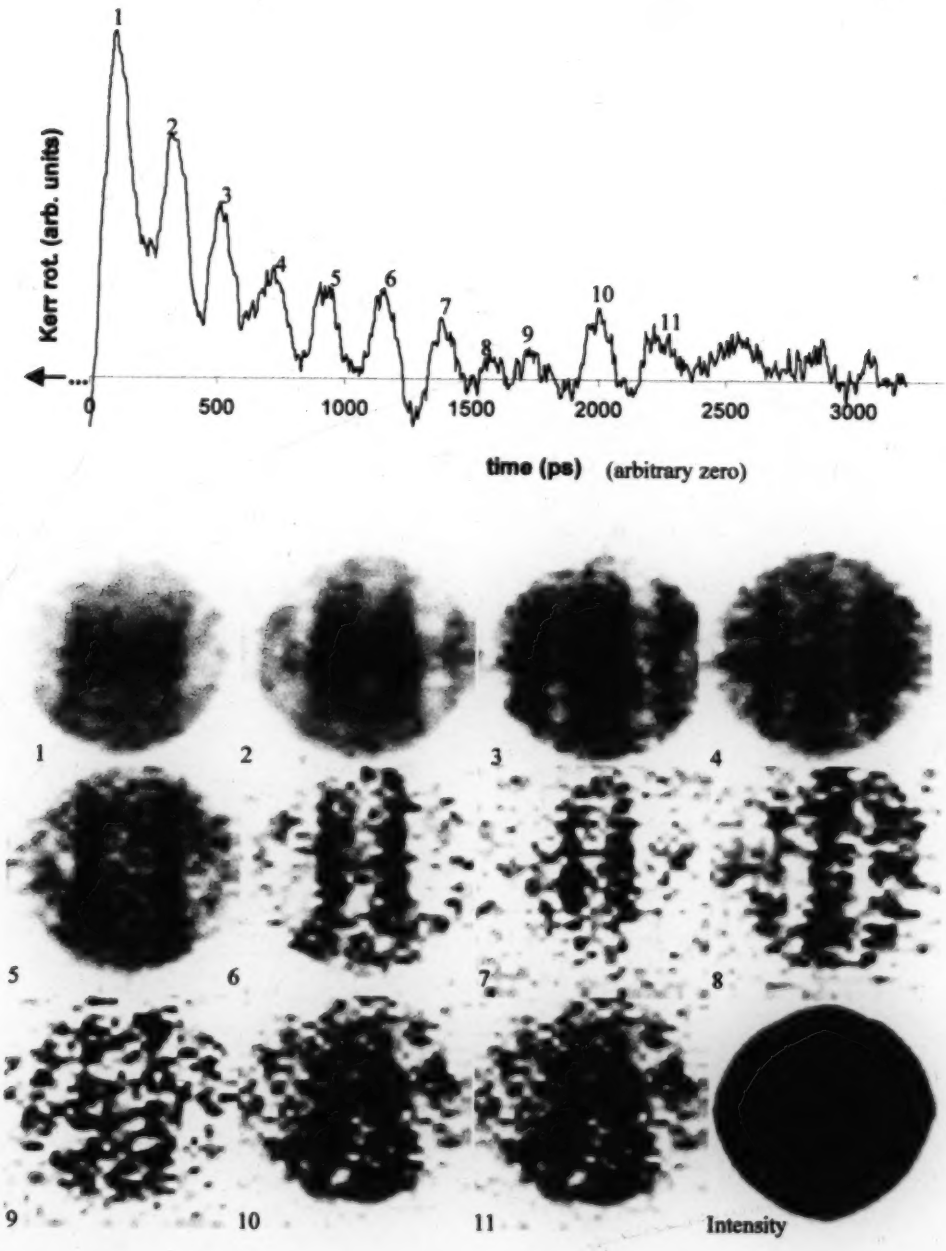

Fig 8.16 Spatial magnetization evolution after the second pulse of a "double kick". Extremely rich magnetization structure is seen.

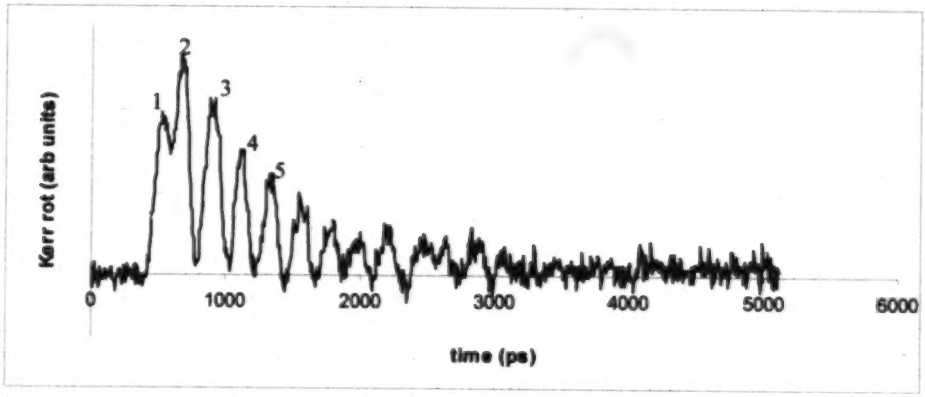

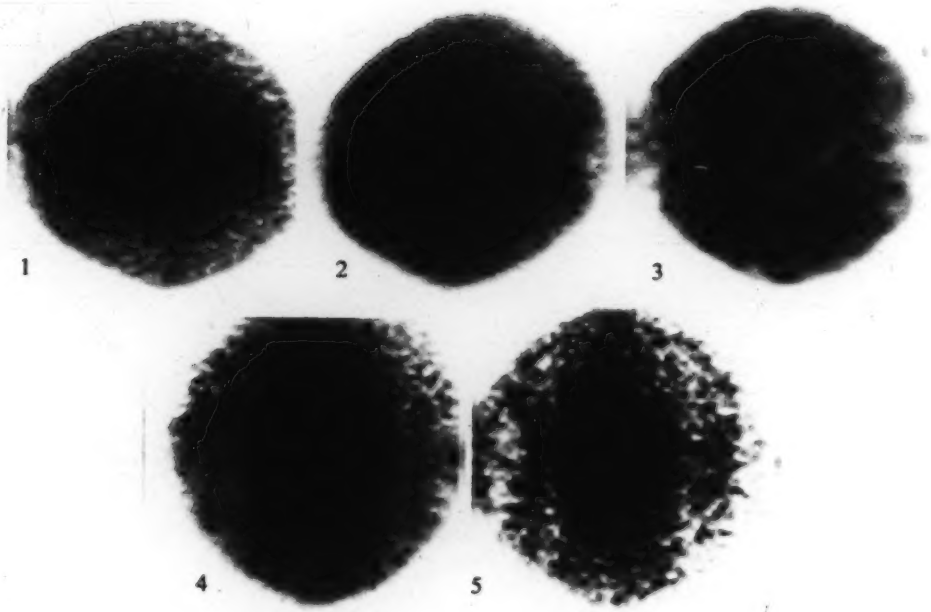

Fig 8.17 Time domain response and spatial magnetization evolution at 90° rotation of the sample. Anisotropy seems to have negligible role.

Also, peaks 1, 2, and 3 compare well with the corresponding peaks 2, 6, and 10 in figure 8.15 (the same external field and time locations, but a different tipping pulse). As expected, the symmetries are retained and the anisotropy field seems to have little effect.

More meaningful modeling may now be done using the 90° data, as the particle is less likely to be put into vastly non-linear modes without the double-kick. Figure 8.18(a) shows the time-domain response at high field (1.9 kOe) overlaid with its interpolating function $H_i(t)$ (as discussed above in section 8.5). Temporal responses for 250, 500, and 1000 Oe are also shown in figures 8.18(b)-(d). Using the same modeling techniques as cited above, the data for the three field value oscillations were fit, simultaneously as mentioned in section 8.5. The results are also shown in figures 8.18(b)-(d) (overlaid on the data) with fitting parameters, $\gamma = 1.76 \times 10^{+7}$ (s Oe)$^{-1}$, $4\pi M_s = 10.8$ kOe, ϕ_0, and α. Here, ϕ_0 is determined from the overall normalization of the signal amplitude, and γ is a well known constant, leaving α as the single parameter describing decay of the oscillations. As can be seen the numerical solutions agree quite well with the experimental data. The only obvious deviation of the fitting from the data occurs during the same time range in all three fits: from about 600 to 1200 ps after the onset of the pulse. If we look back to figure 8.9 from the double pulse data, we notice that the most exciting spatial information corresponds with this time window. In each of panels 4 through 7 of 8.9, excitation "shock waves" combine in the center of the particle and in panels 9 and 10 of fig 8.15(b), four corners of excitation are visible. It makes sense that these locations should represent a higher amplitude oscillation then would be expected for uniform modes. If we assume that there is somewhat similar propagation of non-uniformity

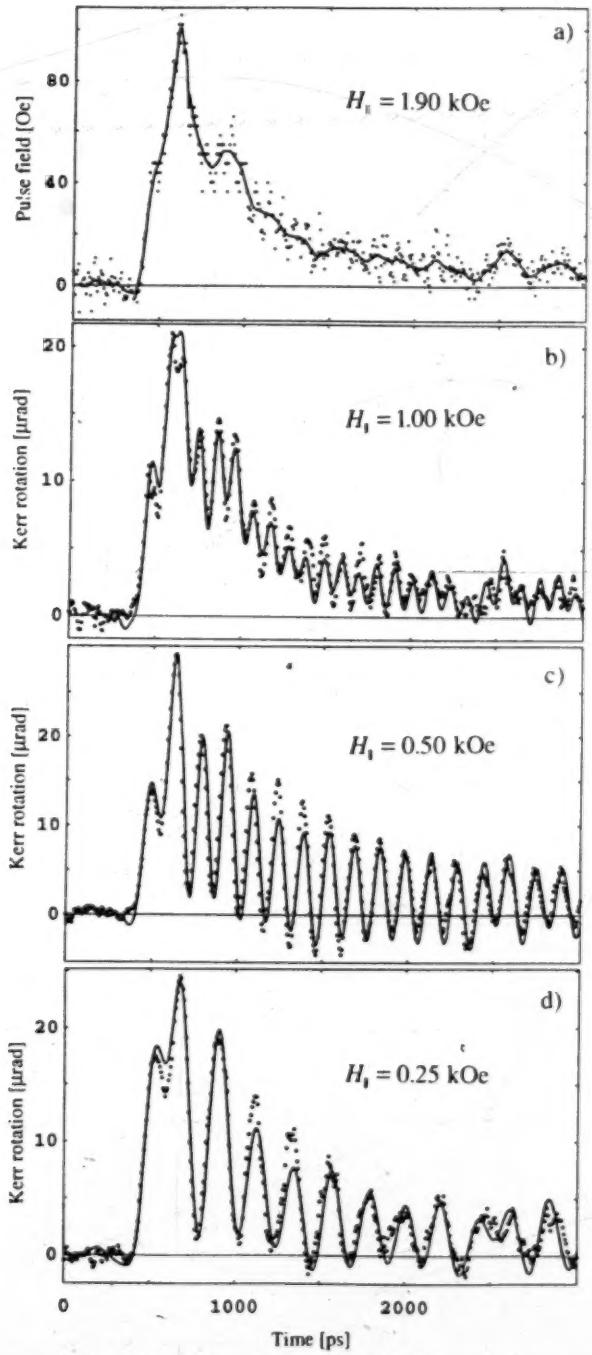

Fig 8.18 Time dependencies for Kerr rotation for several different fields with modeling. Solid line in **(a)** is the interpolating pulse shape $H_1(t)$. Solid lines in **(b)-(d)** are the modeling fit simltaneously to all three sets of data.

information (even with the different tipping function) at 90° then the disagreement seen in the center sections of figure 8.18 is well explained. Admittedly, 500 Oe external field value data for this 90° position would have made our argument more convincing. Unfortunately, the sample was burned after 250 Oe data, not allowing a chance for measurements in 500 Oe.

The value of $\phi_0 = 2.5$ mrad agrees well with ~3 mrad from interpolating a graph[8.4]. It should be remembered that ϕ_0 propagates the estimation of the vertical axis of the tipping function which may assign about 20% too high a value to the z-magnetization. In this case, the specific Kerr rotation would appear low. The value obtained for α is 0.008 which is reasonably consistent with the most reliable value of 0.005 found by Patton[8.5] (using several frequencies as discussed in section 2.6.3). Hearn[8.6] finds a value consistent with 0.014 and Dietrich et al[8.7]. imply 0.06 both using less reliable methods. A change of α by ~10% was found to still fit the data reasonably and can be considered the margin of error. Because of the huge array of particulars that can affect the properties of permalloy the comparison with Patton should be seen as a good agreement. The direct method of measuring α described here is superior in principle, simply because of the ability to localize the measurement.

A note should be made about eddy currents which are usually considered very important in any dynamic analysis of a conducting ferromagnet. In our case, because our structure is small enough, calculations show the eddy current relaxation to be of the order of 1 ps (cf. section 2.4.5: $\tau=\mu_0\sigma r d/2$, where r=4μm, d=0.1μm, σ=1/(~20μΩ-cm), and $\mu_0=4\pi\text{x}10^{-7}$ farads/meter) which is much faster than the rise time of the current pulse so could be omitted in our case.

8.9 Discussion: Uniform Modeling vs. Non-Uniform Response

We have not satisfactorily answered the question as to why the modeling seems to work so well, even though it assumes all excitations are uniform, and at the same time our microstructure clearly exhibits non-uniform response every step of the way. Some assurance is gained by looking at the scale of the non-uniformities that were observed. Many of them were in the micrometer and several micrometer size range. It is possible that our resolution is limiting how small we see these non-uniformities but, because several were larger than our focal spot, it is more likely that we are observing their true scale. Because the range of exchange interaction is much smaller than the non-uniformities, we can suppose that the magnetization is considerably more uniform on this interaction scale, so the mesoscopic non-uniformities would act merely as perturbations (as is evidenced by fig 8.18). This still isn't the whole story, though, considering figure 8.14 again where the strong non-uniformities seem to act as more than a mild perturbation. In fact, the size of the non-uniformities seems to reflect the size of the particle and it is possible that the two scale down together to some degree. In this case, we could conjecture these are the results of an intermediate size regime; the particle is large enough to have non-exchanging perturbations (i.e. large enough to emulate bulk film) so uniform approximations work well in modeling, and at the same time small enough for the edges to play a real role in the bulk oscillations of the particle (it is less likely that the non-uniformities scale up in size, i.e. I've assumed we are seeing their natural scale and energy limitations of a smaller structure could only shrink that scale).

We also stress that creation of the non-uniformities is probably a non-linear process. Hence, the registered response in non-uniform regions may increase non-linearly with the amplitude of pumping current. Furthermore, our detection is only of the surface of the permalloy so we couldn't determine what is occurring below the surface (this problem as well as the problem of thickness being much larger than exchange interaction can be solved merely by going to a thinner film). In order to describe the excitation process accurately, it is necessary to solve the Landau-Lifshitz equation in three dimensions with realistic energy density and proper boundary conditions.

Again, I would like to mention that none of this analysis could even be considered using any other experimental technique. Damping has been measured before, usually indirectly through microwave cavity measurements, as discussed in chapter 2, which necessitates a bulk film. Recall that there was a problem of resonance line broadening from the excitation of non-uniform modes. In our case, we not only avoid this problem but are able to expose the non-uniformities causing it with spatial and temporal resolution. Non-interacting arrays of small structures have also been studied[8.8] to try and identify the small structure properties, but these also must halt their (experimental) analysis at the assumption of uniformity; spatial variance of the magnetization response could never be identified this way.

8.10 Summary

In this chapter we have witnessed the power of time resolved scanning Kerr effect microscopy (TR-SKEM) in which data is taken with simultaneous spatial and temporal resolutions. We have seen ferromagnetic resonance in a permalloy microstructure and

viewed oscillatory behaviour in the time domain. Resonance frequencies were compared with the easy-plane ferromagnet with good agreement ranging from 3 to 11 GHz for external fields of 100 to 1900 Oe, respectively. Non-uniform spatial response was observed and qualified. The magnetization tipping pulse was quantified and an investigation of the effect of boundary conditions and tipping pulse effects on the spatial response was undertaken. Oscillatory response symmetry was shown to be most probably imposed by external field via demagnetizing effects while "extra" asymmetry was seen from the un-centered tipping pulse. Numerical solutions of the Landau-Lifshitz-Gilbert equation, using uniform excitation assumptions, were shown and modeling of the resonance oscillations was done giving good agreement in mildly non-uniform time windows, but substantial disagreement in significantly non-uniform time sections. Model fitting to experimental data was used to confidently elicit a value for the Gilbert dimensionless damping parameter of $\alpha = 0.008$. Discussion regarding the uniformity vs. non-uniformity was given and a conclusion made that the permalloy particle is in an intermediate size regime. It was also concluded that a more complicated modeling of the Landau-Lifshitz equation is needed to more fully understand the behaviour of the permalloy microstructure.

9 CONCLUSION

Ferromagnetic resonance has been studied in a permalloy microstructure using time resolved scanning Kerr effect microscopy (TR-SKEM). Discussions of the design, fabrication, and characterization of the sample were given, several subtleties of the experimental technique were discussed, and results and analysis presented.

The power of the technique has been demonstrated. Picosecond temporal and sub-micrometer spatial resolutions have allowed time-domain and spatial snapshot observation of polar magnetization response giving FMR agreement with theory, numerical modeling partial agreement and elicitation of the damping rate, and non-uniform spatial profile observation.

Discussion for adaptation to longitudinal Kerr detection has been presented for improved versatility of the technique. The spatial and temporal resolutions can be improved and other configurations of the excitation pulse may permit observations of other phenomena including magnetization reversal.

BIBLIOGRAPHY

1.1 Physics Today: Special Issue on Magnetoelectronics, **48** (No.4) April 1995.

1.2 W.Wernsdorfer et. al., Phys. Rev. B **53**, 3341 (1996).

1.3 J.Levy et. al., Phys. Rev. Lett. **76**, 1948 (1996).

1.4 S.T.Chui, Phys. Rev. B **55**, 3688 (1997).

1.5 J.Ding and J.-G.Zhu, J. Appl. Phys. **79**, 5982 (1996).

1.6 M.Lederman, S.Schultz, M.Ozaki, Phys. Rev. Lett. **73**, 1986 (1994).

1.7 M.R.Freeman and J.F.Smyth, J. Appl. Phys. **79**, 5898 (1996).

2.1 T.H.O'Dell, *Ferromagnetodynamics* (The Macmillan Press Ltd., 1981).

2.2 J.E.Thompson, *The Magnetic Properties of Materials* (CRC Press, 1968).

2.3 S.V. Vonsovskii, *Ferromagnetic Resonance* (Pergamon Press Ltd., 1966).

2.4 S.Chikazumi, *Physics of Magnetism* (John Wiley and Sons, Inc., 1964).

2.5 D.J.Craik, R.S.Tebble, *Ferromagnetism and Ferromagnetic Domains* (North-Holland Publishing Company, 1965).

2.6 J.C.Anderson, *Magnetism and Magnetic Materials* (Chapman and Hall Ltd., 1968).

2.7 P.Weiss, J. Phys. **6**, 661 (1907).

2.8 F.Bloch, Z.Phys. **74**, 295 (1932).

2.9 L.Landau, E.Lifshitz, Phys. Z. SowjUn. **8**, 153 (1935).

2.10 J.K.Galt, Phys. Rev. **85**, 664 (1952).

2.11 T.L.Gilbert, J.M.Kelly, *Proc. Conf. Magnetism and Magnetic Materials, A.I.E.E. Publ.*, p. 253 (1955).

2.12 E.W.Lee, D.R.Callaby, Nature **182**, 254 (1958).

2.13 N.C.Ford, J. Appl. Phys. **315**, 300 (1960).

2.14 D.A.Thomson, H.Chang, Phys. Stat. Sol. **17**, 83 (1966).

2.15 A.Green, M.Prutton, J. Scient. Instrum. **39**, 244 (1962).

2.16 J.A.Copeland, F.B.Humphrey, J. Appl. Phys. **34**, 1211 (1963).

2.17 R.L.Conger, G.H.Moore, J. Appl. Phys. **34**, 1213 (1963).

2.18 M.H.Kryder, F.B.Humphrey, J. Appl. Phys. **40**, 2469 (1969).

2.19 M.H.Kryder, F.B.Humphrey, Rev. Scient. Instrum. **40**, 829 (1969).

2.20 M.H.Kryder, F.B.Humphrey, J. Appl. Phys. **41**, 1130 (1970).

2.21 J.A.Watt, G.S.Radley, paper 2.3, Soft Magnetic Materials 7. Conference, European Physical Society, Blackpool (1985).

2.22 S.Ledingham, K.Broadbent, G.S.Radley, Physica Scripta **40**, 526 (1989).

2.23 H.Hauser, F.Hochrieter, M.Gaugitsch, Appl. Phys. Lett. **64** (18), 2448 (1994).

2.24 N.L.Schryer, L.R.Walker, J. Appl. Phys. **45** (12), 5406 (1974).

2.25 N.Smith, IEEE Trans. Magn. **27** (2), 729 (1991).

2.26 J.S.Helman, Phys. Rev. B **43** (7), 5908 (1991).

2.27 W.F.Brown, *Magneto-static Principles in Ferromagnetism* (North-Holland Publ. Co., Amsterdam, 1962).

2.28 E.H.Frei, S.Strikman, D.Treves, Phys. Rev. **106**, 446 (1957).

2.29 R.L.Conger, F.C.Essig, Phys. Rev. **104**, 915 (1956).

2.30 W.Dietrich, W.E.Proebster, P.Wolf, IBM Jl. Res. Dev. **4**, 189 (1960).

2.31 M.Lederman, S.Schultz, M.Ozaki, Phys. Rev. Lett. **73** (14), 1986 (1994).

2.32 L.Neel, Ann. Geophys. **5**, 99 (1949).

2.33 D.R.Fredkin, T.R.Koehler, J.F.Smyth, S.Schultz, J. Appl. Phys. **69** (8), 5276 (1991).

2.34 D.R.Fredkin, T.R.Koehler, IEEE Trans. Magn. **26** (5), 1518 (1990).

2.35 J-G.Zhu, H.N.Bertram, J. Appl. Phys. **63** (8), 3248 (1988).

2.36 M.Kersten, Z. Phys. **124**, 714 (1948).

2.37 C.E.Patton, Z.Frait. C.H.Wilts, J. Appl. Phys. **46**, 5002 (1975).

2.38 P.H.Bryant, J.F.Smyth, S.Schultz, D.R.Fredkin, Phys. Rev. B **47** (17), 11255 (1993).

2.39 M.J.Freisen, IEEE Trans. Magn. **4** (2), 152 (1968).

2.40 C.C.Robinson, J. Opt. Soc. Amer., **54** (10), 1220 (1964).

2.41 C.C.Robinson, J. Opt. Soc. Amer., **53** (6), 681 (1963).

2.42 P.N. Argyres, Phys. Rev. **97** (2), 334 (1955).

2.43 W.Voigt, *Magneto- und Elector-Optik* (Teubner, Leipzig, 1908).

2.44 Landolt-Bornstein, New Series III/19a, Figures 250 and 251, 269, (1966).

2.45 P.Kasiraj, R.M.Shelby, J.S.Best, D.E.Horne, IEEE Trans. Magn. **22** (5), 837 (1986).

2.46 M.Prutton, Phil. Mag. **4**, 1063 (1959).

2.47 A.Green, M.Prutton, W.S.Carter, J. Scient. Instrum. **40**, 480 (1963).

2.48 A.Fowler, E.M.Fryer, Phys. Rev. **94**, 52 (1954).

2.49 B.E.Argyle, B.Petek, D.A.Herman Jr., J. Appl. Phys. **61** (8), 4303 (1987) .

2.50 K.Shirae, K.Sugiyama, J. Appl. Phys. **53** (11), 8380 (1982).

2.51 F.Schmidt, W.Rave, A.Hubert, IEEE Trans. Magn. **21** (5), 1596 (1985).

2.52 S.N.Jasperson, S.E.Schnatterly, Rev. Scient. Instrum. **40** (6), 761 (1969).

2.53 E.W.Lee, D.R.Callaby, A.C.Lynch, Proc. Phys. Soc. **72**, 233 (1958).

2.54 M.E.Re, M.H.Kryder, J. Appl. Phys. **55** (6), 2245 (1984).

2.55 M.R.Freeman, R.R.Ruf, R.J.Gambino, IEEE Trans. Magn. **27** (6), 4840 (1991).

3.1 H.D.Arnold, G.W.Elmer, J. Franklin Inst. **195**, 621 (1923).

3.2 G.W.Elmer, J. Franklin Inst. **207**, 583 (1929).

3.3 J.F.Dillinger, R.M.Bozorth, Physics, **6**, 279 (1935).

3.4 F.Pfeifer, C.Radeloff, J. Magn. and Magn. Mater. **19**, 190 (1980).

3.5 G.Y.Chin, IEEE Trans. Magn. **7**, 102 (1971).

3.6 J.F.Freedman, IEEE Trans. Magn. **5**, 752 (1969).

3.7 R.C.Hall, J. Appl. Phys. **30** (6), 816 (1959).

3.8 E.T.Ferguson, J. Appl. Phys. **29** (3), 252 (1958).

3.9 R.M.Bozorth, J.G.Walker, Phys. Rev. **89** (3), 624 (1953).

3.10 S.Chikazumi, *Physics of Magnetism* (John Wiley and Sons, Inc., 1964).

3.11 J.E.Thompson, *The Magnetic Properties of Materials* (CRC Press, 1968).

3.12 M.Prutton, *Ferromagnetic Films* (London: Butterworth, 1964).

3.13 L. Neel, Compt. rend. **237**, 1468, 1613 (1953); J. Phys. radium **15**, 225 (1954).

3.14 T.Fujii, Suchiyama, M.Masuda, Y.Sakaki, IEEE Trans. Magn. **4** (3), 515 (1968).

3.15 S.Tsunashima, M.Suzuki, T.Fujii, S.Uchiyama, Jpn. J. Appl. Phys. **15** (3), 439 (1976).

3.16 A.S.Koo, P.Kasiraj, IEEE Trans. Magn. **27** (6), 4452 (1991).

3.17 K.Krusch, IEEE Trans. Magn. **22** (6), 626 (1986).

3.18 M.Takahashi, A.Fujita, T.Shimatsu, T.Wakiyama, J.Yamada, Tshiba, IEEE

Translation Journal on Magnetics in Japan **6** (2), 127 (1991).

3.19 R.Nakatani, K.Hoshino, S.Noguchi, Y.Sugita, Jpn. J. Appl. Phys. **33**, 133 (1994).

3.20 M.F.Gillie, J.N.Chapman. J.C.S.Kools, J. Magn. and Magn. Mater. **140-144**, 721 (1995).

3.21 H.T.Kim, S.J.Kim, S.H.Han, H.J.Kim, I.K.Kang, IEEE Trans. Magn. **31** (6), 4100 (1995).

3.22 C.A.Grimes, H.J.Lee, IEEE Trans. Magn. **32** (5), 4520 (1996).

3.23 Y.K.Kim, T.J.Silva, Appl. Phys. Lett. **68** (20), 2885 (1996).

4.1 M.R.Freeman, R.R.Ruf, R.J.Gambino, IEEE Trans. Magn. **27** (6), 4840 (1991).

4.2 Private Communication.

4.3 A.G.Foyt, F.J.Loenberger, R.C.Williamson, SPIE.

4.4 D.H.Auston, Appl. Phys. Lett. **26** (3), 101 (1975).

5.1 J.J.Kelly, G.J.Koel, J. Electrochem. Soc. **125** (6), 860 (1978).

5.2 M.F.Gillies, J.N.Chapman, J.C.S.Kools, J. Magn. and Magn. Mater. **140-144**, 721 (1995).

5.3 R.Nakatani, K.Hoshino, S.Noguchi, Y.Sugita, Jpn. J. Appl. Phys. **33**, 133 (1994).

5.4 K.Ouchi, H.Ishiguro, S.Ohkijima, Y.Nakamura, IEEE Trans. Magn. **27** (6), 4912 (1991).

5.5 J.L.Vossen, W.Kern (eds.), *Thin Film Processes II* (Academic Press, Inc., 1991).

5.6 M.J.Brett, Thin Films course notebook, Dept. of Electrical Engineering, University of Alberta (unpublished).

5.7 J.A.Thornton, Annu. Rev. Materials Science **7**, 239 (1977).

5.8 B.Movchan, A.Demchishin, Phys. Metals and Metallography **28**, 83 (1969).

5.9 A.Y.Elezzabi, M.R.Freeman, M.Johnson, Phys. Rev. Lett. **77**, 3220 (1996).

5.10 Y.L.Li, MSc. Thesis, Dept. of Electrical Engineering, University of Alberta (1995, unpublished).

6.1 Control System Manual, Nanoscope III Version 3.0, p. 37 (1993).

6.2 P.Grutter, Y.Liu, P.LeBlanc, U.Durig, Appl. Phys. Lett. **71**, 279 (1997).

6.3 J.Ding, J-G.Zhu, J. Appl. Phys. **79** (8), 5892 (1996).

7.1 A.Y.Elezzabi, M.R.Freeman, M.Johnson, Phys. Rev. Lett **77**, 3220 (1996).

7.2 M.R.Freeman, J.F.Smyth, J. Appl. Phys. **79**, 5898 (1996).

7.3 S.M.Mansfield, G.S.Kino, Appl. Phys. Lett. **57**, 2615 (1990).

7.4 T.J.Silva, A.B.Kos, to be published.

7.5 W.W.Clegg N.A.E.Heyes, E.W.Hill, C.D.Wright, J. Magn. and Magn. Mater. **83**, 535 (1990).

8.1 W.K.Hiebert, A.Stankiewicz, M.R.Freeman, Phys. Rev. Lett. **79** (6), 1134 (1997).

8.2 A.Y.Elezzabi, M.R.Freeman, Appl. Phys. Lett. **68**, 3546 (1996).

8.3 S.Zhang, S.A.Oliver, N.E.Israeloff, C.Vittoria, Appl. Phys. Lett. **70** (20), 2756 (1997).

8.4 from interpolation of graph, Landolt-Bornstein, New Series III/19a, Fig. 250.

8.5 C.E.Patton, Z.Frait, C.H.Wilts, J. Appl. Phys. **46**, 5002 (1975).

8.6 B.R.Hearn, Int. J. Electron **16**, 33 (1964).

8.7 W.Dietrich, W.E.Proebster, P.Wolf, IBM Jl. Res. Dev. **4**, 189 (1960).

8.8 J.F.Smyth, S.Schultz, D.R.Fredkin, D.P.Kern, S.A.Rishton, H.Schmid, M.Cali, T.R.Koehler, J. Appl. Phys. **69** (8), 5262 (1991).

APPENDIX 1: LITHOGRAPHIC COILS AND DOTS

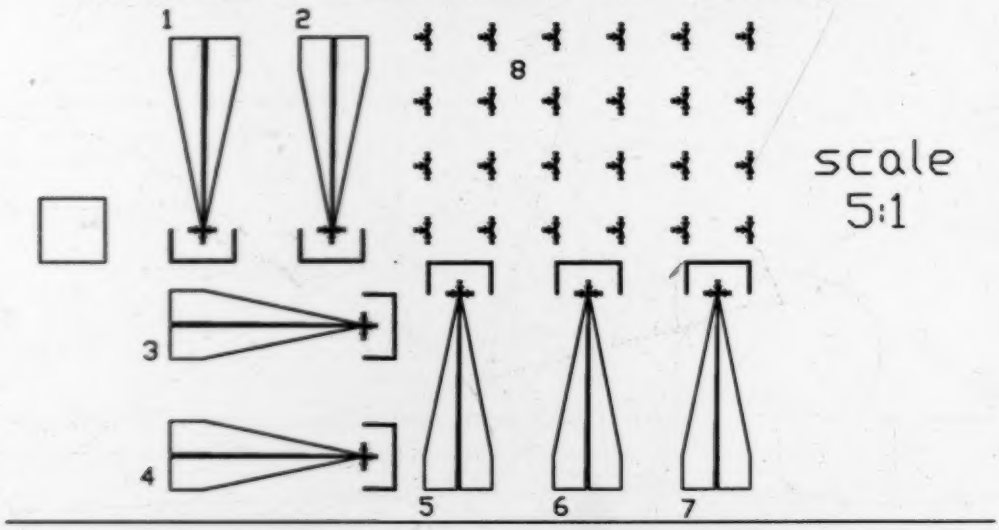

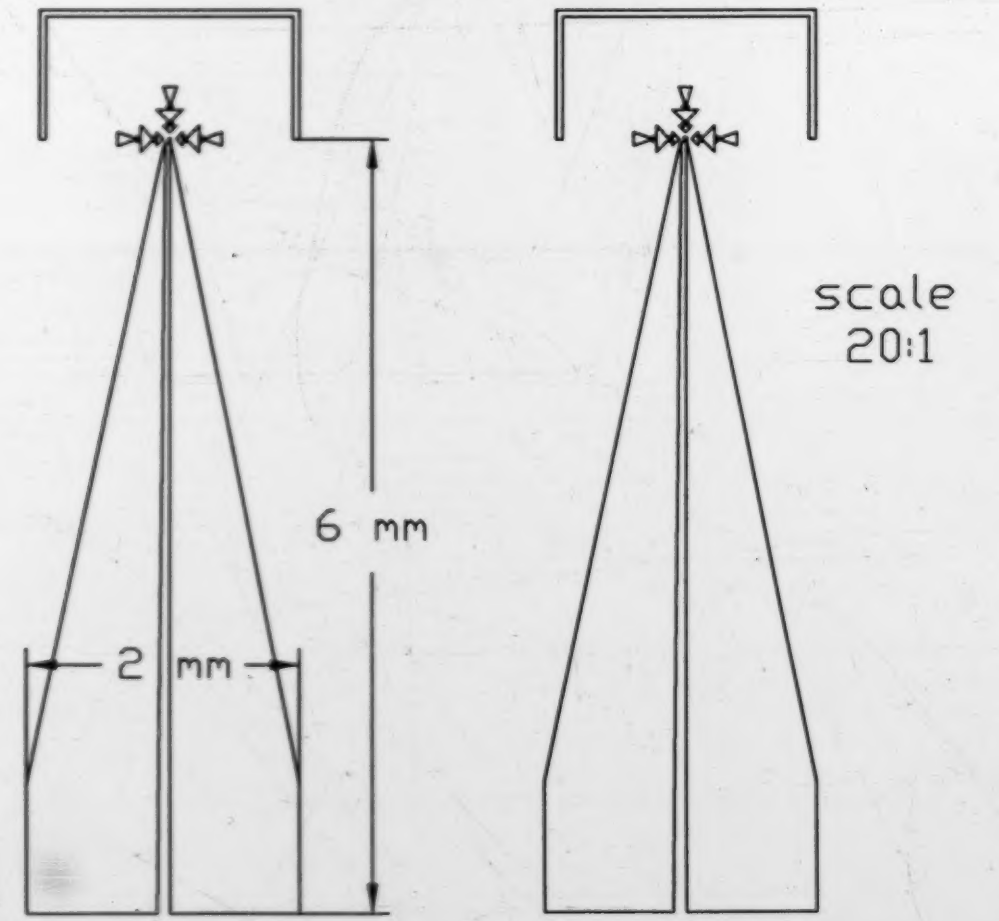

Coil #6
scale:
125:1

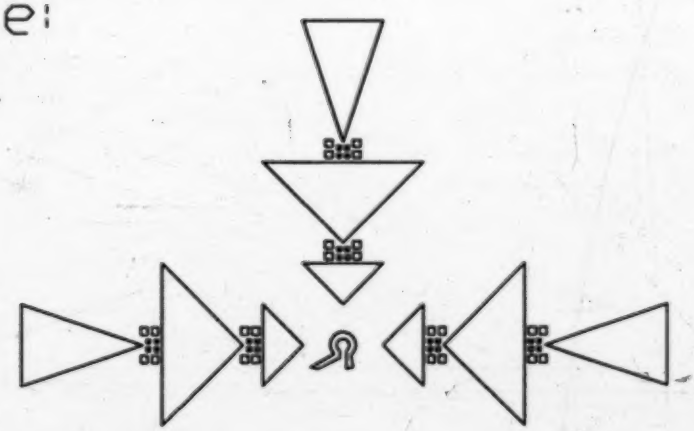

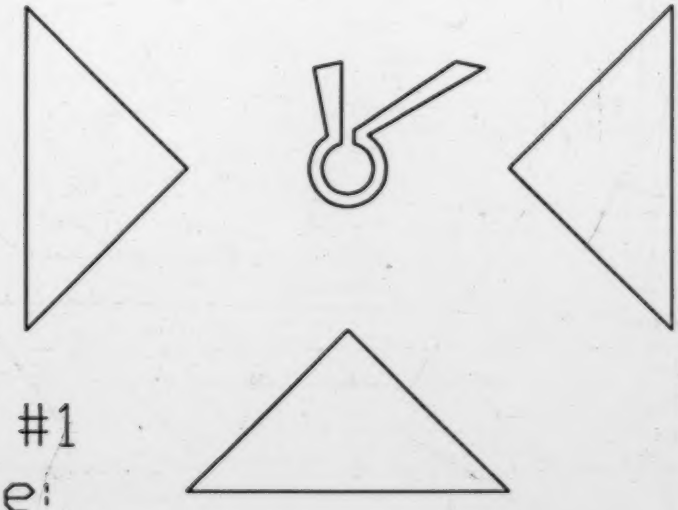

Coil #1
scale:
500:1

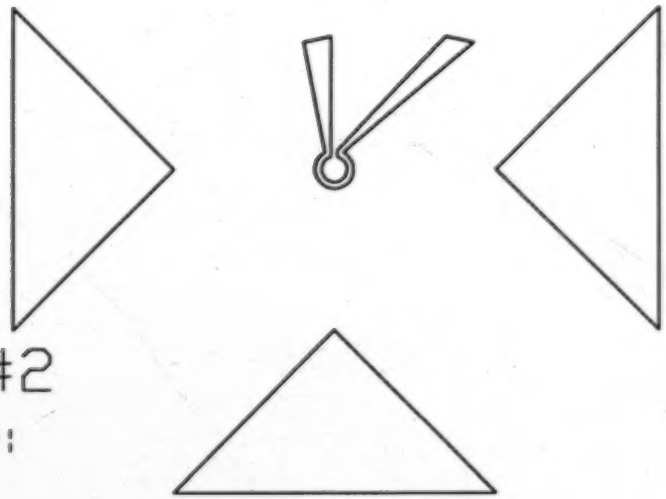

Coil #2
scale:
500:1

Coil #3
scale
500:1

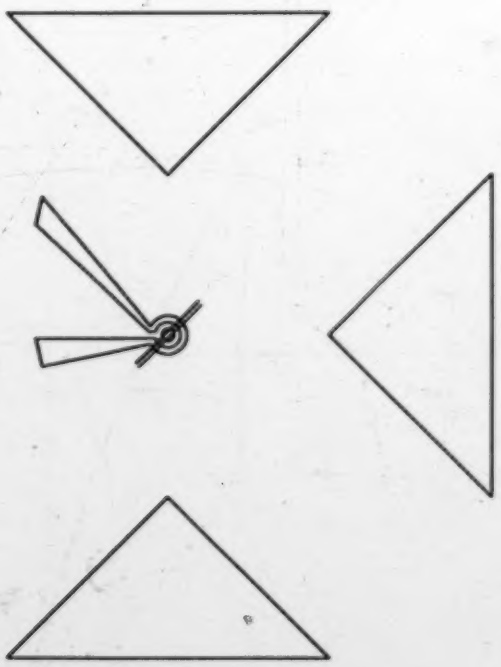

Coil #4
scale:
500:1

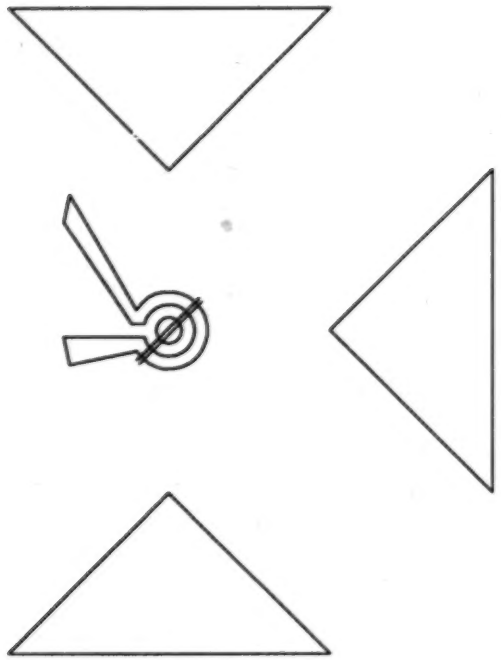

Coil #5
scale:
500:1

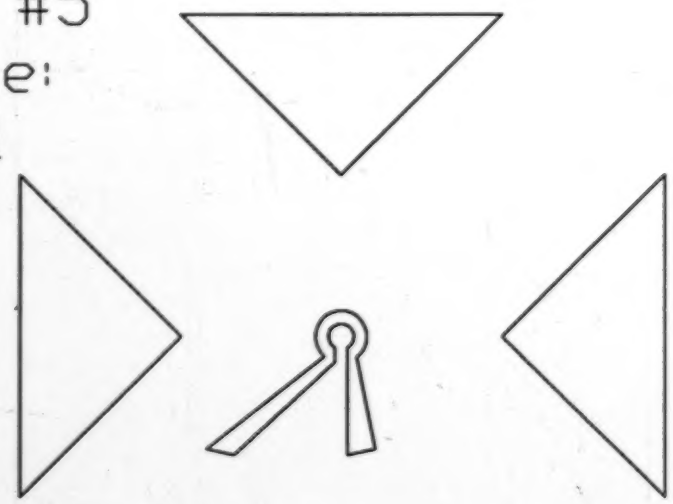

Coil #6
scale:
500:1

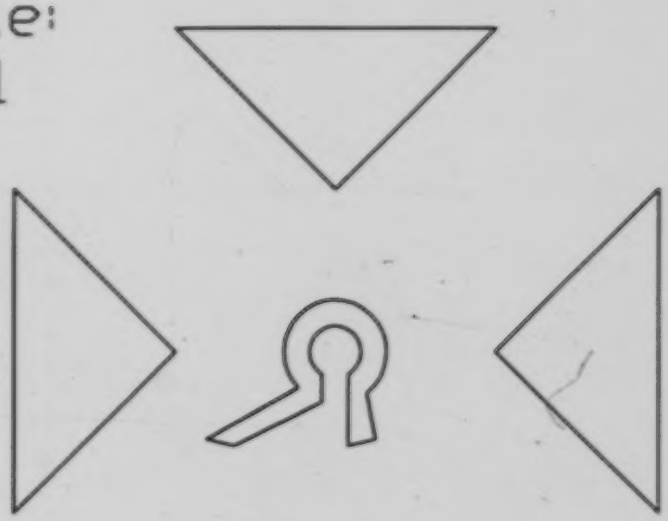

Coil #7
scale:
500:1

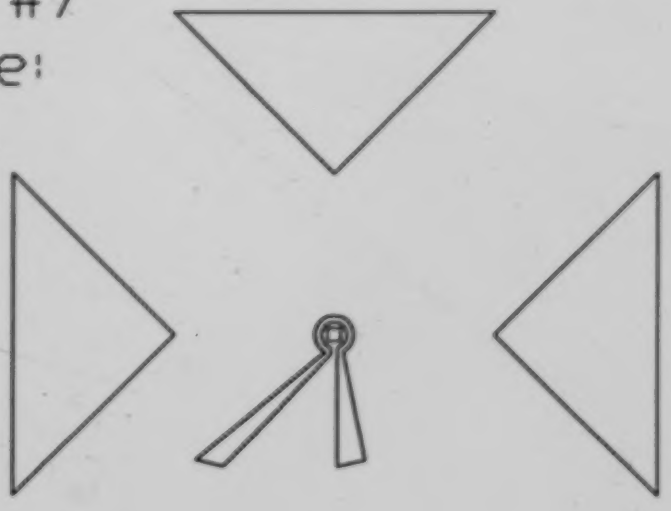

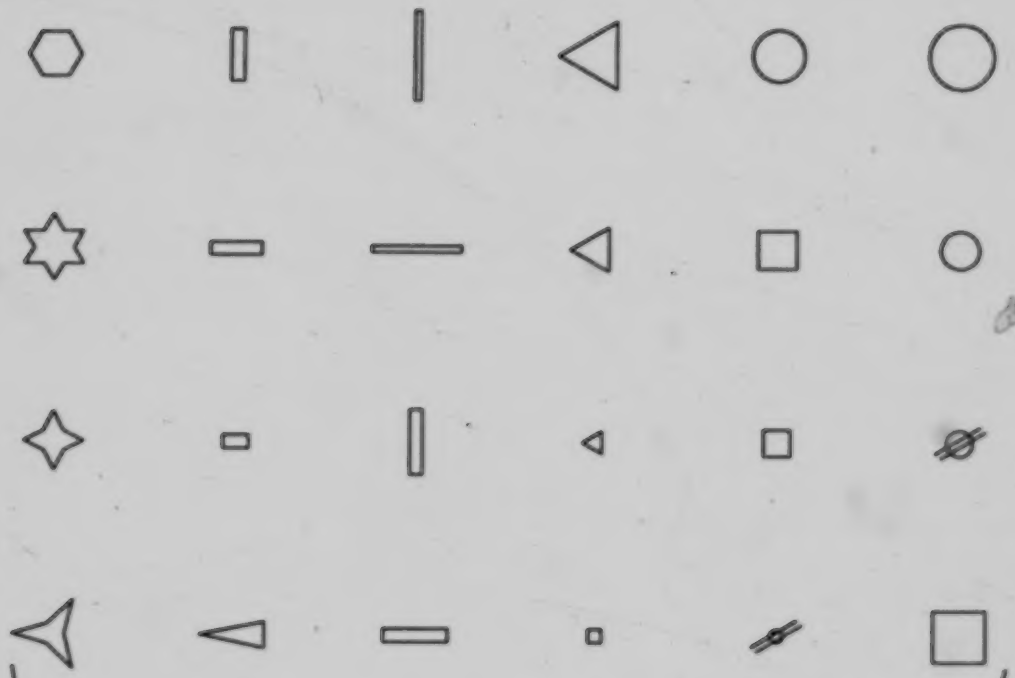

#8 scale: 1000:1

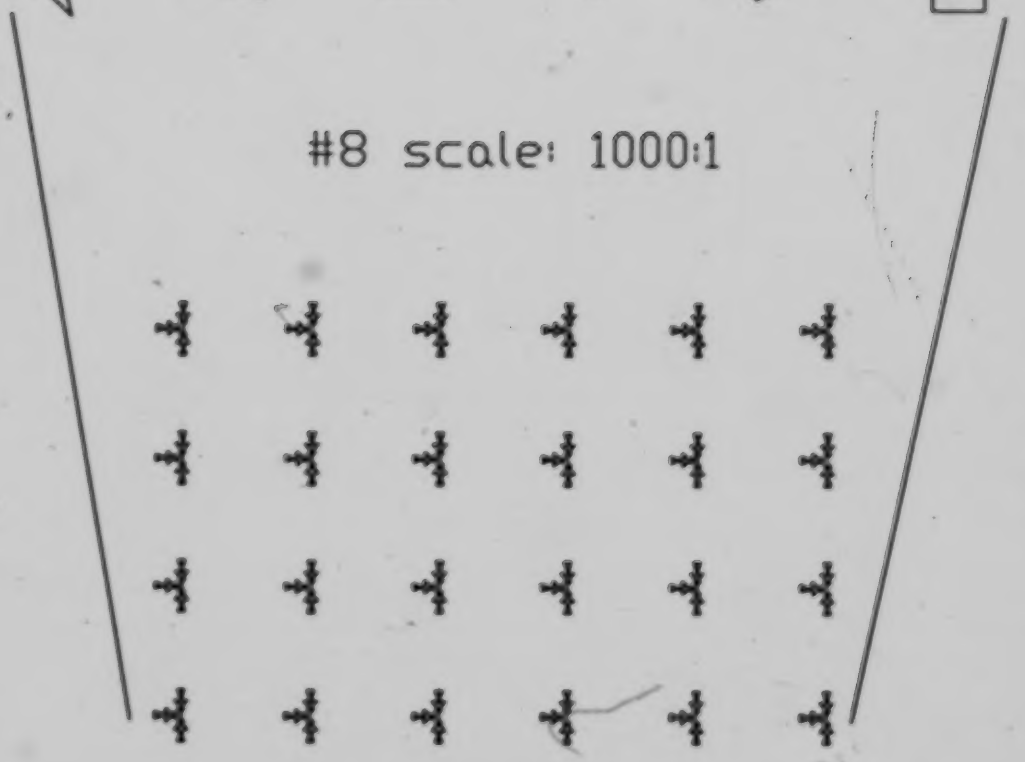

APPENDIX 2: PHOTOCONDUCTIVE SWITCHES

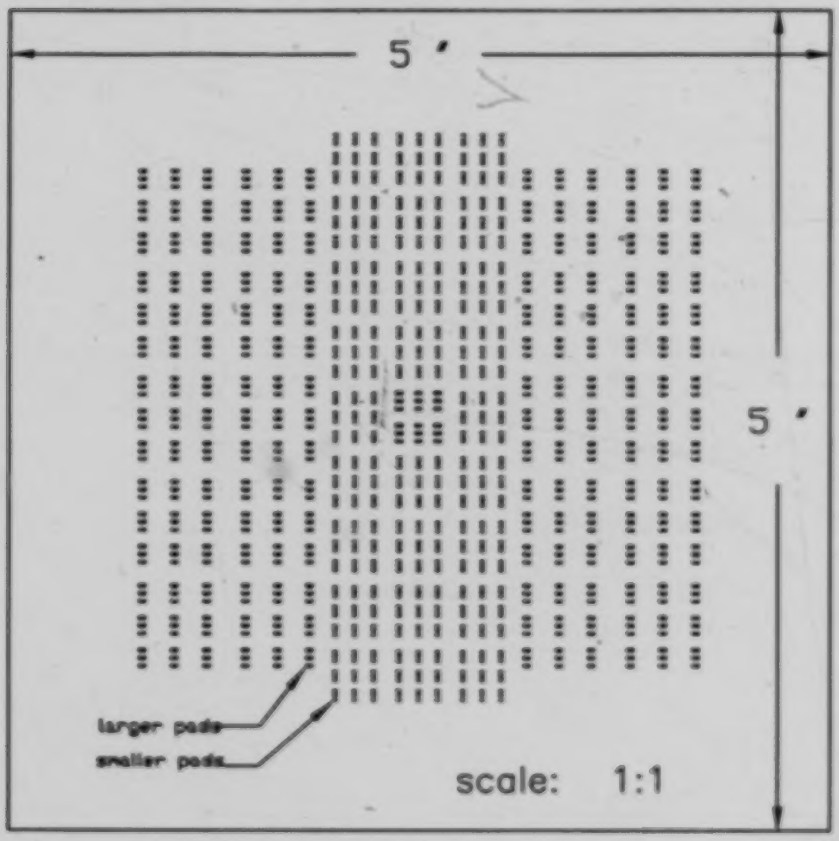

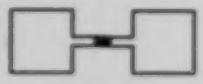

"3-set" with larger pads

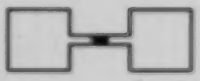

"3-set" with smaller pads

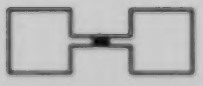

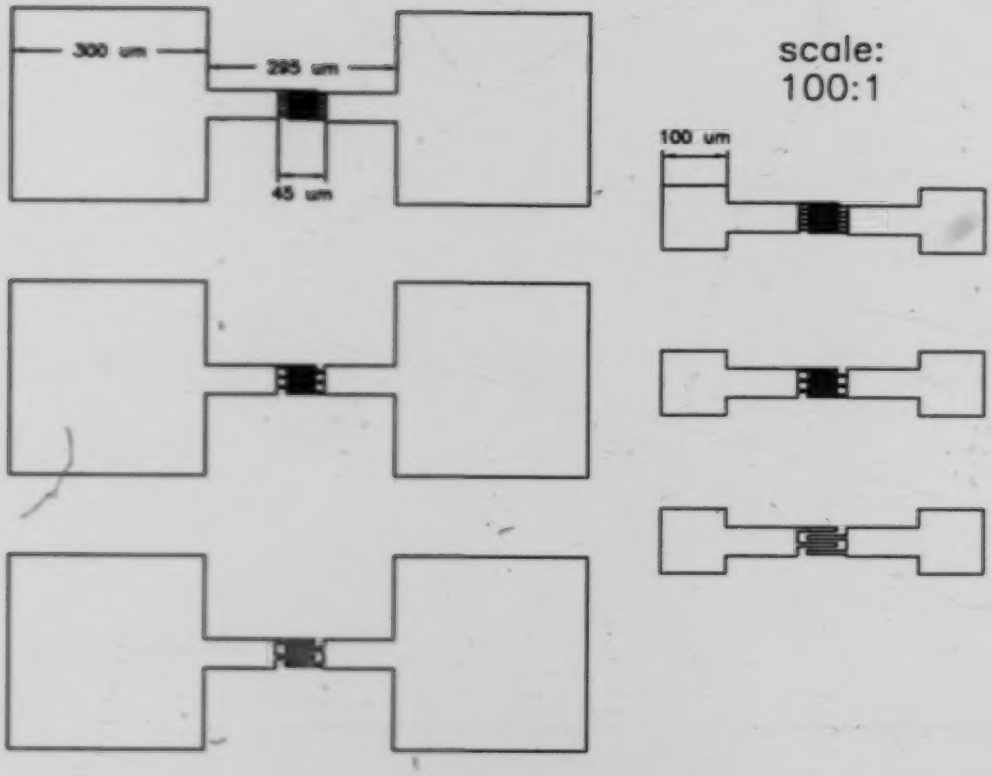
300 um
295 um
45 um
scale:
100:1
100 um

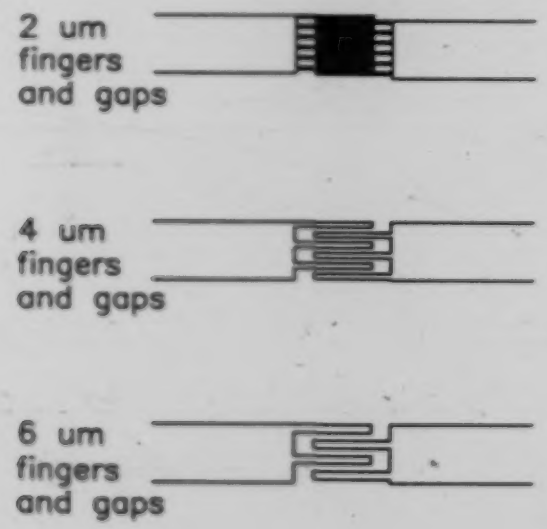
2 um
fingers
and gaps
scale:
200:1
4 um
fingers
and gaps
6 um
fingers
and gaps

APPENDIX 3: UHV SUBSTRATE HOLDER

magnet holder

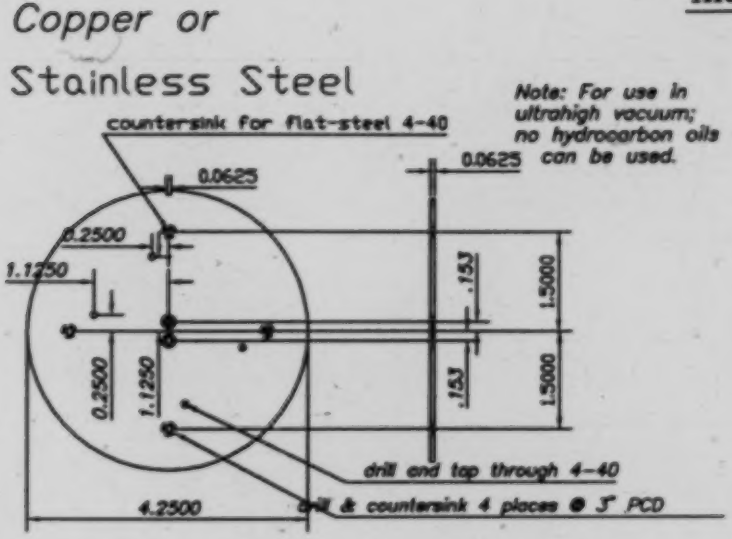

backing plate

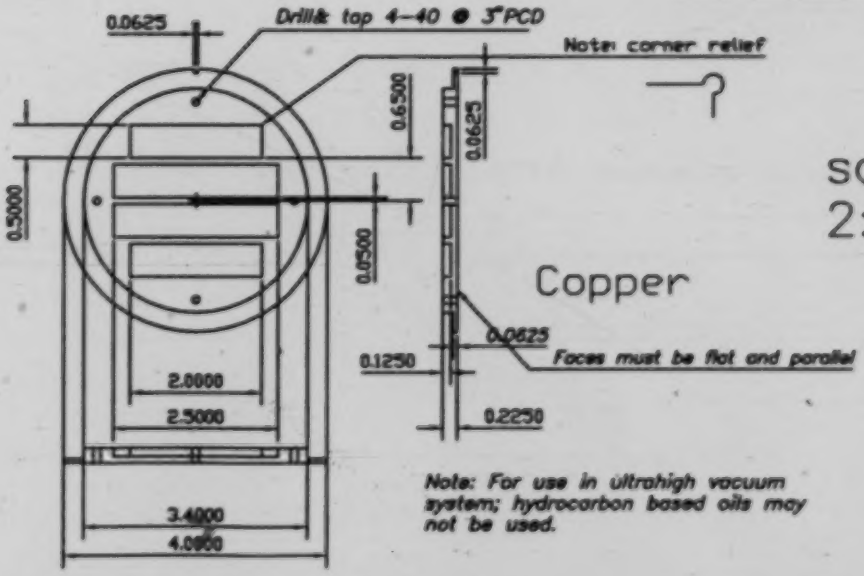

Note: This piece was built as designed and modified as on the top ot the following page.

modified backing plate

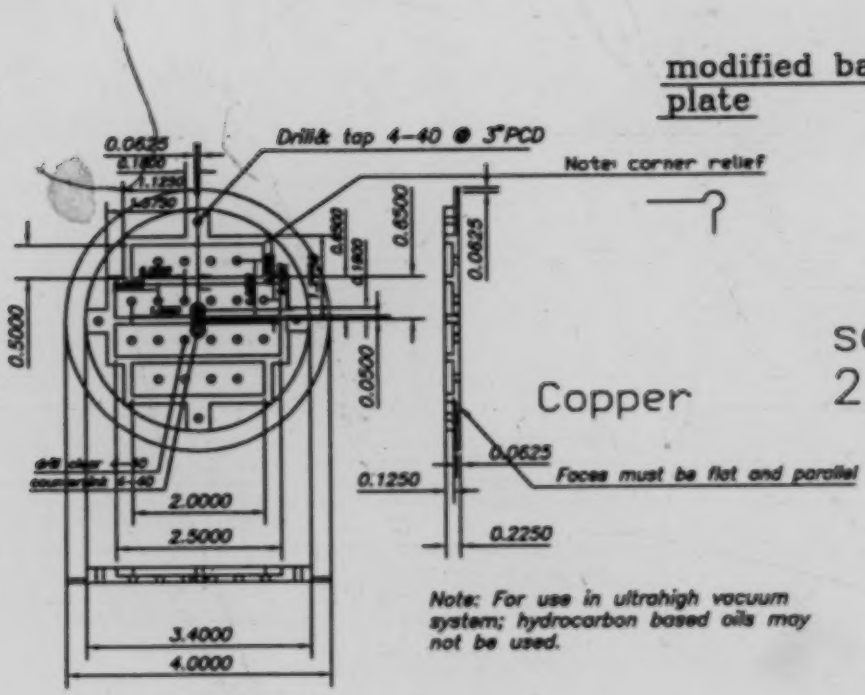

Copper

scale: 2:5

---

substrate fasteners

Stainless Steel X 2

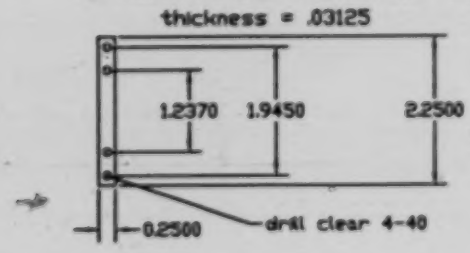

scale 2:5